APPROVAL SHEET

Title of Dissertation: Modeling nonlinearity and noise in high-current photodetectors

Name of Candidate: Yue Hu
Doctor of Philosophy, 2017

Dissertation and Abstract Approved: _____
Curtis R. Menyuk

Department of Computer Science and Electrical Engineering

Date Approved: _April 5, 2017_

Yue Hu's Curriculum Vitae

Education

Ph.D. in Electrical Engineering, GPA: 4.0   May/2017

University of Maryland, Baltimore County (UMBC) , Baltimore, MD

Graduate study in Optical Engineering, GPA: 3.6/4   2009

University of Electronic Science and Technology of China, Chengdu, Sichuan China

B.A. in Electrical Engineering, GPA: 3.7/4   2006

University of Electronic Science and Technology of China, Chengdu, Sichuan China

Skills

Platforms: Unix, Linux, Windows 7/10

Programming Language: Proficient in C/C++, Python, VBA, MATLAB, Tex

Also basic ability with: MPI, CUDA, Hadoop, Mapreduce, Spark, Graph

Software: MATLAB, COMSOL

Research Experience

University of Maryland, Baltimore County   Baltimore, MD

Research Assistant – Electric Engineering   June 2011 - July 20

- Developed 1D/2D modified drift-diffusion models using Matlab to study non-linearity in high current and high speed photodetectors used in the RF pho-

tonics. Finite difference method and finite element method were used to solve the equations.

- Designed a equivalent circuit model of a p-i-n photodetector to study nonlinearity and frequency response of a high speed photodetector.

- Used high performance computing/parallel computing (MPI and CUDA in the cluster Maya) to solve partial differential equation, such as drift-diffusion equations.

- Studied frequency response of high speed photodetectors using modified drift-diffusion model to determine the bandwidth and response time of photodetector; Provided suggestions to modify the structure of the photodetector to improve the bandwidth.

- Studied power-to-phase noise conversion and analyzed shot noise in the high current photodetector using drift-diffusion model.

- Modeled heat transfer in device to determine heat sink performance and effect of the structure of photodetector.

Teaching Assistant – Electric Engineering   August 2010 - May 2011

- Instructed/mentored undergraduate students in circuit design concepts; Advised students during office hours, graded homework, supervised weekly lab exercises (circuit design class)

Relevant Projects

Futurewei Technologies Inc.   Santa Clara, CA

Internship, Machine Learning   August 2016 - Jan. 2017

- Design an innovation Java Spark machine learning system, and apply it to the network product R&D. I focus on data mining in the current network product database. Used Java to extract features from log file which save in a Hadoop DHFS system.

- Applied K-means and Gaussian Mixture Model to achieve classification and anomaly detection on spark. Used supervised learning algorithm (SVM, Decision Tree) to detect anomaly.

Parallel Computing using CUDA and MPI   Fall 2014

- Wrote conjugate gradient method in MPI C to solve 2D Poisson and heat transport equations. BLAS (Basic Linear Algebra Subprograms) were used. Speedup were analysis based on number of cores and nodes that used.

- Fourier transform and image processing was performed through CUDA C.

Primary Publications

Y. Hu, C. Menyuk, M. Hutchinson, V. Urick, K. Williams, *"Frequency dependent harmonic powers in a modified uni-traveling carrier photodetector,"* Opt. Lett. Vol. 42, pp. 919–929, 2017

Y. Hu, C. Menyuk, M. Hutchinson, V. Urick, K. Williams, "*Impact of the Coulomb interaction on the FranzKeldysh effect in high-current photodetectors* ," Opt. Lett. Vol. 41, pp. 456–459, 2016

Y. Hu, T. Carruthers, C. Menyuk, M. Hutchinson, V. Urick, and K. Williams, "*Simulation of a partially depleted absorber (PDA) photodetector*," Opt. Express Vol. 23, pp. 20402–20417, 2015

Y. Hu, B. Marks, C. Menyuk, V. Urick, and K. Williams, "*Modeling sources of nonlinearity in a simple p-i-n photodetector.*" J Lightw. Tech. Vol. 32, pp. 3710–3720, 2014

Conference Presentations

Y. Hu, T. Carruthers, C. Menyuk, M. Hutchinson, V. Urick, and K. Williams, *Modeling nonlinearity in a modified uni-traveling-carrier (MUTC) photodetector*, in 2015 IEEE Photonics Conference (IPC), pp.122–123, Oct 2015.

Y. Hu, C. Menyuk, M. Hutchinson, V. Urick, and K. Williams, *Impact of the Coulomb Interaction on the Franz-Keldysh Effect in a High-Current Photodetector*, in 2015 OSA CLEO, STh3F.6., 2015

Y. Hu, C. Menyuk, M. Hutchinson, V. Urick, and K. Williams, *Modeling nonlinearity in a partially depleted absorber photodetector and a modified uni-traveling carrier photodetector*, 2014 IEEE Photonics Conference (IPC), pp.206–207, Oct 2014.

Y. Hu, C. Menyuk, V. Urick, and K. Williams, *Sources of nonlinearity in a pin photodetector at high applied reverse bias*, in 2013 International Topical Meeting on

Microwave Photonics (MWP), pp. 282–285, Oct 2013.

Y. Hu and C. Menyuk, *Computational modeling of nonlinearity in a pin photode-tector*, in 2013 International Semiconductor Device Research Symposium (ISDRS), Dec 2013.

ABSTRACT

Title of dissertation: MODELING NONLINEARITY AND NOISE
IN HIGH-CURRENT PHOTODETECTORS

Yue Hu, Doctor of Philosophy, 2017

Dissertation directed by: Professor Curtis R. Menyuk
Department of Computer Science
and Electrical Engineering

High-current, high-power photodetectors are important in RF-photonic systems, optical communications systems, photonic microwave generation, and high-frequency measurement systems. Device nonlinearity limits the performance of these photodetectors. In order to obtain a linear response with a high output current, we must understand the sources of nonlinearity and find ways to mitigate them. Besides nonlinearity, another important characteristic of photodetectors is the phase noise and amplitude-to-phase (AM-to-PM) conversion. This effect limits the performance of photonic microwave generation systems. We must find the source of AM-to-PM conversion in the photodetectors and find ways to mitigate it.

In this dissertation, we first describe one-dimensional (1D) and two-dimensional (2D) drift-diffusion models that we used to study p-i-n, partially depleted absorber (PDA), and modified uni-traveling carrier (MUTC) photodetectors. We obtained excellent agreement with experiments for the harmonic power and responsivity. Impact ionization, external loading, and the Franz-Keldysh effect are all included in the model.

In a *p-i-n* photodetector, we found that impact ionization is an important source of nonlinearity. In a PDA photodetector, we showed that the Franz-Keldysh effect is an important source of nonlinearity. Decreasing the effective load resistor decreases the higher harmonic powers.

In an MUTC photodetector, our theoretical calculation agree well with the experimental results. We demonstrated that the dominant physical source of non-linearity is the Franz-Keldysh effect. We also showed that a shift in the bias null that occurs when the difference frequency is compared to the sum frequency is due to displacement current in the intrinsic region of the device.

AM-to-PM conversion in the photodetector occurs due to nonlinearities in the photodetector. We used the impulse response to calculate the phase delay in the photodetector and to analyze the source of AM-to-PM conversion. AM-to-PM noise conversion is due to the change in the transit time that occurs when the pulse energy changes. Our calculations show that the AM-to-PM noise conversion coefficient can be reduced 90% by completely removing the heterojunction between InGaAs and InP. While that is not possible to do in practice, this result demonstrates that it should be reduced as far as possible.

In the course of our studies, we have created a computational model for high-current photodetectors. Using this model, we have carried out a detailed study of the field and current evolution in these devices. In addition to its use to analyze the characteristics of existing photodetectors, this model can be used to design new device structures.

MODELING NONLINEARITY AND NOISE IN HIGH-CURRENT PHOTODETECTORS

by

Yue Hu

Dissertation submitted to the Faculty of the Graduate School of the
University of Maryland, Baltimore County in partial fulfillment
of the requirements for the degree of
Doctor of Philosophy
2017

Advisory Committee:
Professor Curtis R. Menyuk, Chair/Advisor
Dr. Meredith Hutchinson
Professor Fow-Sen Choa
Professor Anthony Johnson
Professor Terrance Worchesky

Acknowledgments

I owe my gratitude to all the people who have made this dissertation possible and because of whom my graduate experience has been one that I will cherish forever.

First and foremost I'd like to thank my advisor, Professor Curtis Menyuk for giving me an invaluable opportunity to work on challenging and extremely interesting projects over the past six years. I would also like to thank my committee members, Dr. Meredith Hutchinson, Professor Fow-Sen Choa, Professor Anthony Johnson, and Professor Terrance Worchesky for serving as my committee members. Thank you for your comments and suggestions for my dissertation.

I would to thank all my colleagues at the Computational Photonics Laboratory that have enriched my graduate life in many ways and deserve a special mention.

I owe my deepest thanks to my family - my mother, my father, and my wife who have always stood by me and guided me through my career, and have pulled me through against impossible odds at times. Words cannot express the gratitude I owe them.

It is impossible to remember all, and I apologize to those I've inadvertently left out.

Lastly, thank you all.

Table of Contents

List of Figures

Chapter 1

Introduction

High-current, high-power photodetectors are important in RF-photonic or analog photonic systems [1, 5–10], fiber-radio wireless communications systems [11, 12], photonic microwave generation systems [13, 14], and high-frequency measurement systems [4, 15]. The main goal when designing an RF-photonic system is to minimize the noise and distortion that occurs when translating signals between the radio frequency (RF) and optical domains. Our goal is to find the sources of noise and distortion in the photodetectors and to mitigate them by proper design.

1.1 Analog photonics links

1.1.1 Overview of analog photonic links

Figure 1.1 shows a typical fiber optic link. An optical link has three basic components. These are: (1) a modulation device, which transfers the electrical signal onto an optical carrier, (2) an optical fiber, and (3) a photodetector, which recovers the electrical signal from the optical carrier. The fiber has a relatively low loss compared to microwave cables. An optical fiber operating at 1.5 μm has a loss of 0.2 dB/km, while a typical 3/8-inch cable has a loss of 18 dB/km at 10 GHz [1].

Analog photonic or RF-photonic systems have significant advantages over purely electronic systems in many RF applications [1, 5, 7–10, 16, 17]. These ad-

vantages include reduced size, lower cost, immunity to electromagnetic interference, large bandwidth, and low loss. However, analog links also have some limitations, which include less efficiency, a higher noise figure, a lower spur-free dynamic range (SFDR), and lower RF power [7].
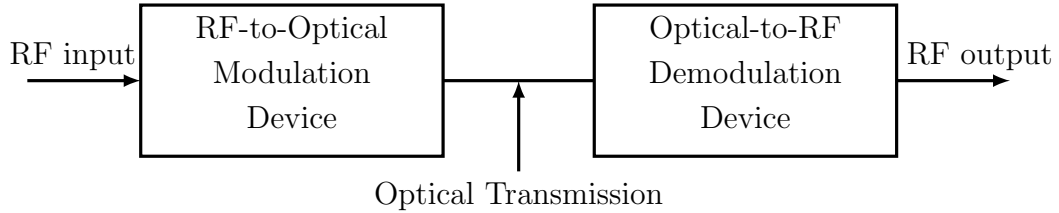
Figure 1.1: Basic structure of a fiber optic link: modulation device, optical fiber and photodetector. Similar to Fig. 1.2 in [1].

1.1.2 Frequency response and distortion in analog links

The RF gain of an analog photonic link is the ratio of the RF power at the photodetector output to the RF power at the input of the modulator. The RF gain is frequency dependent, which is an important system limitation since it leads to distortion [1]. Hence, it is important to understand the sources of this frequency dependence. First, the laser has a frequency-dependent response to the modulator frequency. For a semiconductor laser, the laser's frequency response depends on the carrier lifetime and the photon lifetime [1]. The modulator also has a frequency-dependent response to the RF current. For the Mach-Zehnder modulator (MZM), which is the most commonly used modulator, the frequency response is determined by the optical transit time past the electrodes relative to the modulation period of the maximum modulation frequency [1]. Additionally, the photodetector has a

2

frequency-dependent response. Its response is the most complex and difficult to analyze. We will discuss its response in more detail later.

Distortion of a sinusoidal current input produces harmonics of the fundamental signal, which limits the performance of an RF-photonic link. The most important distortion is the third-order intermodulation power because this distortion produces frequencies that are close to the fundamental frequency. The distortion at inter-modulation and harmonic frequencies increases faster than the fundamental power as the power increases. As the power increases, the distortion will eventually be greater than the noise limit. Below this power, the link is considered to be linear; above this power, the link is considered to be nonlinear.

1.2 Microwave generation
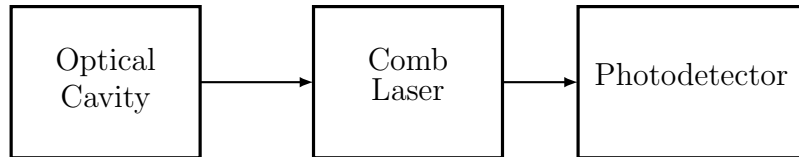
Figure 1.2: Microwave generation from frequency combs.

Recently, there has been great interest generating microwaves through optical frequency division (OFD) with a modelocked laser comb [13, 14, 18, 19]. Ultrastable microwave generation has been demonstrated [18, 19]. The stability of the optical reference is transferred to the repetition rate of the pulse train of a modelocked laser. Figure 1.2 shows a schematic diagram of microwave generation using a photodetector. One approach for achieving optical-to-electrical conversion is the balanced optical-microwave photodetector (BOM-PD) [20, 21]. Direct pulse detection

3

is also promising. The pulsed output of the frequency-stabilized laser illuminates a high-speed photodiode that produces a microwave signal. The phase noise that is produced by the photodetector is a critical limit to system performance.

Carrier-envelope-phase locking (CEPL) of passively modelocked lasers has great potential for low-noise microwave generation [22]. The key figures-of-merit for photodetectors in optoelectronic oscillators and CEPL lasers are the power spectrum of the phase noise, including the white noise and flicker noise contributions, as well as the power-to-phase conversion ratio. The noise contributions are more important in optoelectronic oscillators [23], while the power-to-phase conversion is more important in CEPL lasers [19, 24]. The impact of these physical effects on device performance is qualitatively understood and has impacted the design of the detection systems [24], but quantitative design tools have been lacking.

1.3   Photodetector

1.3.1   Overview of photodetector

A photodetector is an optoelectronic device that absorbs light and converts it to electric current. Modern photodetectors operate on the basis of the internal photo-effect, in which the generated electron-hole pairs remain in the sample [25]. The absorption of a photon by a semiconductor results in the generation of an electron in the conduction band and a hole that is generated in the valence band. In the presence of an electric field, the two carriers drift in opposite directions. The transport of the carriers induces an electric current in the external circuit.

The most common photodetector in use for analog optical links is the *p-i-n* photodetector. Figure 1.3 shows a diagram of a reversed-biased *p-i-n* photodetector. Most of the voltage through the device occurs in the intrinsic region. After an electron-hole pair is generated in the intrinsic region, the electron and the hole drift in opposite directions due to the electric field. The photo-generated electrons drift to the *n*-region, and the holes drift to the *p*-region. The photodiode is a diode. So, under reverse bias and with a dark condition in which there is no incoming light, there is only the dark current I, which is given by [26]

$$I = I_0 \left[\exp\left(\frac{qV}{k_B T} \right) - 1 \right], \tag{1.1}$$

where I_0 is a parameter depending on the doping level and material of the photodetector, V is bias voltage, q is the magnitude of the electron charge, k_B is Boltzmann's constant, and T is temperature. If the device is reverse biased, the dark current is negligible. The photocurrent is dependent on the light intensity and is defined as

$$I_p = \frac{\eta q}{h\nu} P_{\text{opt}}, \tag{1.2}$$

where η is the quantum efficiency, h is the Planck's constant, ν is the frequency of incident light, and P_{opt} is the input optical power.

The quantum efficiency η of a photodetector equals N_e/N_{phot}, where N_e is the number of electrons per second in the output current and N_{phot} is the number of photons per second in the incoming light. For a surface normal photodetector, the
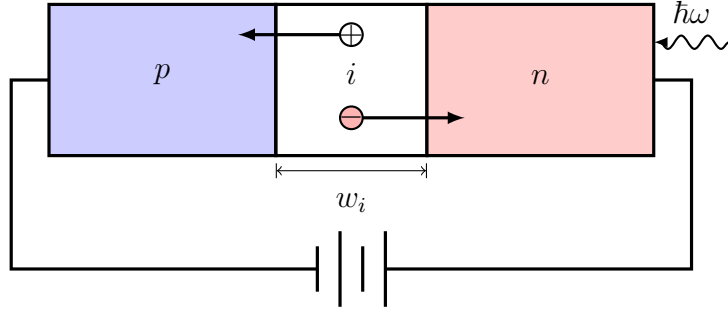
Figure 1.3: Basic structure of p-i-n photodetector.

quantum efficiency can be written as

$$\eta = \zeta(1 - R)\left[1 - \exp(-\alpha w_i)\right],\tag{1.3}$$

where ζ is the fraction of electron-hole pairs that contribute to the photocurrent, R is the reflection index, α is the absorption coefficient, and w_i is the length of the absorption layer in the photodetector, which is the length of the intrinsic region in the p-i-n photodetector. The responsivity $\mathfrak{R}$ can be defined as the ratio of the output current to the input optical power. From Eq. 1.2, we obtain

$$\mathfrak{R} = \frac{\eta q}{h\nu}.\tag{1.4}$$

Another important feature of a photodetector is its response time or bandwidth, which is constrained by the transit time and the RC time constant, where R is due to the series load resistance and C is the junction capacitance. Since the electron velocity is faster than the hole velocity in InGaAs by factor of 2, the transit time is mainly determined by the hole velocity in the intrinsic region. For a p-i-

n photodetector, the bandwidth is limited by this transit time and approximately equals [27]

$$f_T = \frac{v_{p,\text{sat}}}{\pi w_i},$$

(1.5)

where $v_{p,\text{sat}}$ is the saturation hole velocity. The RC-limited bandwidth is given by [27]

$$f_{RC} = \frac{1}{2\pi C (R_s + R_{\text{load}})},$$

(1.6)

where R_s is the series resistance and R_{load} is the load resistor. The capacitance in the p-i-n photodetector is given by [26]

$$C = \frac{\epsilon A}{w_i},$$

(1.7)

where ϵ is the dielectric constant and A is the area of the device.

A thicker (w_i) intrinsic region leads to a higher efficiency. However, the transit time becomes longer, which reduces the frequency range. Additionally, space charge in the intrinsic region leads to nonlinearity in the p-i-n photodetector. Hence, there is a trade-off between efficiency, transit time, and nonlinearity.

1.3.2 Introduction of modeling photodetector

In the mid-1990s, Williams, et al. [28, 29] developed a 1D model of high-current photodetectors, based on the drift-diffusion equations, which greatly elucidated space-charge effects in these devices. Since that time, this model has been improved in several ways. Improvements include taking into account the barrier

heights at the material interfaces [30], taking into account the external circuit [30], and taking into account the change in the refractive index [31]. Jiang, et al. [32] developed a circuit-equivalent model to study the distortion of the *p-i-n* photodetector. In this early work, these authors [30–32] determined the *p-i-n* photodetecter's harmonic power at different frequencies for different illumination powers and determined the influence of the circuit paramters on the behavior of the photodetector. Walker and colleagues [33,34] developed 1D and 2D models of metal-semiconductor-metal photodetectors to study the transient behavior of the photodetectors. They showed that it is possible for a 1D model to give a good approximate solution. They also discussed diffraction and transient behavior in an metal-semiconductor-metal (MSM) photodetector. Wilson et al. [35] studied impact ionization effect in GaAs *p-i-n* photodetector under high illumination. Recently, Fu et al. [36] used a 1D drift-diffusion model to study the nonlinear intermodulation distortion in a modified uni-traveling-carrier (MUTC) photodetector. In the model, they included the Franz-Keldysh effect and impact ionization. They calculated the electric field in the device and then calculated the absorption coefficient and impact ionization in the device.

In our earliest work, we revisited the question of determining the sources of nonlinearity in a simple *p-i-n* photodetectors at room temperature [37]. Subsequent to the early simulation work [2, 3, 33, 34], it had been discovered that several effects that were not included in the original studies can play an important role. These include external loading [38], thermionic emission at the heterojunction boundaries [39–41], incomplete ionization [41], impact ionization [36, 41–43], and the Franz-

Keldysh effect [44].

We showed that impact ionization, in particular, is the dominant nonlinear effect at large reverse biases (>10 V) in a simple p-i-n device, leading in most cases to an increase in the harmonic power beyond some voltage [37]. Additionally, modern-day computers allowed us to carry out cylindrically-symmetric two-dimensional (2D) simulations and thus take into account transverse diffusion without making *ad hoc* assumptions about the beam radius. We showed that it is necessary to take into account 2D effects to obtain good agreement with experiments at low reverse biases where the transverse diffusion becomes important. Finally, we carried out fully implicit simulations, in contrast to the explicit simulations in the original work by Williams et al. [2,3]. Explicit simulations of the drift-diffusion equations are intrinsically unstable [45]. (See also ref. [3], Fig. 4.14, p. 56.) Williams et al. [2,3] used a grid-dependent diffusion cap that avoids this instability, but lowers the diffusion by up to a factor of 100 in some regions of the photodetector — in particular, the p-i interface. We did not use a diffusion cap, which in some cases led to different physics for the dominant source of nonlinearity. In particular, we found that the role of p-region absorption is less than what Williams et al. [2] predicted because of diffusive backflow of electrons from the n-region through the intrinsic region to the p-region.

We then extended the model to study the sources of nonlinearity in a partially depleted absorber (PDA) photodetector [46,47], which has several absorption layers on each side of intrinsic region in PDA photodetector [46]. These photodetectors can support higher currents than can standard p-i-n photodetectors, but have a structure

that is significantly more complex. In InGaAs, the electron velocity is much greater than the hole velocity, and the carrier velocity difference induces device nonlinearity. In a PDA photodetector, it is possible to have a better carrier balance in the intrinsic region, reducing the built-in fields, by adjusting the length of the absorption layers.

Subsequent to the original experimental study [46], it was discovered that several voltage-dependent effects, such as the Franz-Keldysh effect and impact ionization, play a role in the generation of higher harmonic power [44,48]. In this work, we used a 2D drift-diffusion model that uses one longitudinal and one radial dimension and assumes cylindrical symmetry, in keeping with our prior work that showed that a 2D model produces more reliable results than a 1D purely longitudinal model, particularly at low reverse bias where transverse current flow is important [37]. It also allowed us to avoid *ad hoc* assumptions for the radial intensity profile of the incident light. We included incomplete ionization, the Franz-Keldysh effect, external loading, and history-dependent impact ionization in our model [37, 43, 47, 49–51], and we studied the influence of all these effects on the harmonic power.

We showed that the Franz-Keldysh effect can be an important source of nonlinearity in PDA photodetectors. It leads to changes in the absorption coefficient that depend on the incident light wavelength and the strength of the electric field. We showed that increasing the length of the *p*-region absorption layers can eliminate the impact of the Franz-Keldysh effect. We also found that history-dependent impact ionization can be important in PDA photodetectors. The "dead length" [51], which is the distance required for a carrier to gain sufficient kinetic energy from the electric field so that it can initiate impact ionization, cannot be ignored in a device

10

with a thin intrinsic region. Finally, we showed that decreasing the load resistor decreases the harmonic powers.

We next applied our model to the MUTC photodetector, where the only traveling carriers are electrons. A key difficulty is that modeling the interface becomes complicated because the structure is complicated. Hence, in each heterojunction, we use a thermionic emission model as the boundary condition. To apply this model, we need to find the correct band structure in order to obtain the barrier height. In the intrinsic region, the electron velocity has an overshoot as a function of the electric field strength. However, the intrinsic layer is sufficiently thin, such that the transient behavior of the electron can become important. Our model must correctly describe the velocity in the intrinsic region. In the PDA or *p-i-n* photodetector, the active material only consists of InGaAs. However, in an MUTC photodetector, InP is also an important material in the collection layer [36]. It is important to choose the right parameters for the electron velocity model in InP.

We also studied AM-to-PM conversion using our model. In order to calculate the AM-to-PM conversion coefficient, we calculate the impulse response of the photodetector in time. We then use the Fourier transform to calculate the phase at each pulse intensity. Since the pulse duration is short (about 100 femtoseconds), we have to use a small time step to calculate the impulse response.

Chapter 2

Modeling the *p-i-n* photodetector

2.1 Structure of the *p-i-n* photodetector

The basic structure that we investigated is a single heterojunction device made from InP and InGaAs [2], as shown in Fig. 2.1. The device is composed of a highly-doped transparent *n*-InP substrate of length $w_n = 0.1$ μm ($N_D = 2 \times 10^{17}$ cm^{-3}), an intrinsic layer of *n*-InGaAs of length $w_i = 0.95$ μm ($N_B = 5 \times 10^{15}$ cm^{-3}), and a degenerately doped *p*-InGaAs *p*-region of length $w_p = 1$ μm ($N_A = 7 \times 10^{18}$ cm^{-3}), where N_A and N_D denote the acceptor and donor densities, and N_B denotes the unintentional donor density in the intrinsic region. The total length of the photodetector is $L = 2.05$ μm. The incident light was assumed to pass through an aperture on the *n*-side ohmic contact of the device. The device radius is 15 μm. In the simulation, we set $N_D = 2 \times 10^{17}$ cm^{-3}, $N_A = 7 \times 10^{18}$ cm^{-3}, and $N_B = 5 \times 10^{15}$ cm^{-3}. We used z to parameterize the distance along the device from the *p*-contact, and we used r to parameterize the radial distance.

2.2 Drift-diffusion model

To model the carrier transport in the photodetector, we used both 1D and 2D drift-diffusion models [33,34,43,52–58]. The 1D model ignores the radial dependence

12
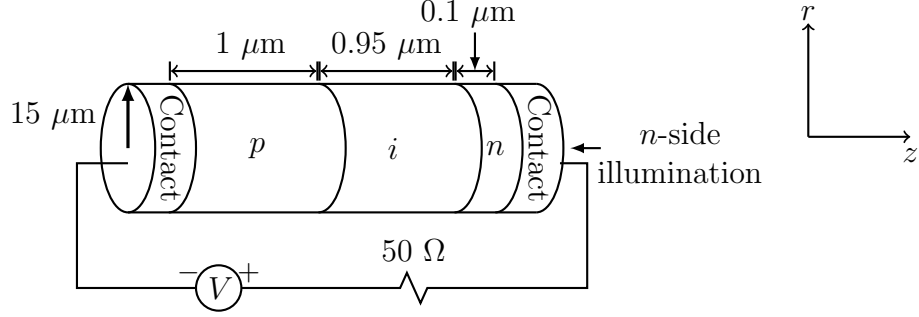
Figure 2.1: Structure of the *p-i-n* photodetector. Lengths are not to scale.

of all qualities, while the 2D model assumes cylindrical symmetry. Both of these

models consist of three equations that govern the dynamics of the electron density

n, the hole density p, and the electric field $\mathbf{E}$ (gradient of the electrostatic potential,

φ),

$$\frac{\partial(n - N_D^+)}{\partial t} = G_l + G_i - R(n, p) + \frac{\nabla \cdot \mathbf{J}_n}{q}, \tag{2.1a}$$

$$\frac{\partial(p - N_A^-)}{\partial t} = G_l + G_i - R(n, p) - \frac{\nabla \cdot \mathbf{J}_p}{q}, \tag{2.1b}$$

$$\nabla \cdot \mathbf{E} = \frac{q}{\epsilon} \left(N_D^+ + p - n - N_A^- \right), \tag{2.1c}$$

where q is the unit of charge (here positive), G_l and G_i are the generation rate from

light and impact ionization, R is the recombination rate, ϵ is the permittivity of

the semiconductor material, and N_D^+ and N_A^- are the ionized donor and acceptor

impurity concentrations. The variables $\mathbf{J}_n$ and $\mathbf{J}_p$ are the current densities for

electrons and holes, respectively, and are given by

$$\mathbf{J}_n = qn\mathbf{v}_n(\mathbf{E}) + qD_n\nabla n, \tag{2.2a}$$

$$\mathbf{J}_p = qp\mathbf{v}_p(\mathbf{E}) - qD_p\nabla p, \tag{2.2b}$$

13

where D_n and D_p are the electron and hole diffusion coefficients, respectively, while $\mathbf{v}_n(\mathbf{E})$ and $\mathbf{v}_p(\mathbf{E})$ are the electric-field-dependent electron and hole drift velocities, respectively.

The electron velocity as a function of electric field has been measured for InGaAs samples at electric field strengths from 10–100 kV/cm. An empirical expression that has been used to fit $\mathbf{v}_n(\mathbf{E})$ for electrons in InGaAs is given by [3,52]

$$\mathbf{v}_n = \frac{\mathbf{E}\left(\mu_n + v_{n,\text{sat}}\beta|\mathbf{E}|\right)}{1 + \beta|\mathbf{E}|^2}, \tag{2.3}$$

where μ_n is the electron low-field mobility, $v_{n,\text{sat}}$ is the saturated electron velocity, and β is a fitting parameter. The parameters μ_n, $v_{n,\text{sat}}$, and β are given in Table 2.1. The hole velocity has also been measured in the range of 50–100 kV/cm. An empirical expression that has been used to fit $\mathbf{v}_p(\mathbf{E})$ for the holes in the InGaAs is given by [59]

$$\mathbf{v}_p = \frac{\mu_p v_{p,\text{sat}}\mathbf{E}}{\left(v_{p,\text{sat}}^{\gamma} + \mu_p^{\gamma}|\mathbf{E}|^{\gamma}\right)^{1/\gamma}}, \tag{2.4}$$

where μ_p is the hole low-field mobility, γ is an empirical fitting parameter that depends on temperature, and $v_{p,\text{sat}}$ is the saturated hole velocity. The parameters μ_p, γ, and $v_{p,\text{sat}}$ are given in Table 2.1. In Fig. 2.2, we show the electron and hole velocities as a function of the electric field magnitude given by Eqs. 2.3 and 2.4.

The doping-dependence of the low-field mobilities, μ_n and μ_p, are fitted to available experimental data, using Hilsum's empirical formula [41,60],

Parameter	InP	In$_{0.53}$Ga$_{0.47}$As
W$_g$ (eV)	1.35	0.74
χ (eV)	4.38	4.6
ϵ_r (eV)	12.4	13.7
ΔW_D (eV)	0.007	0.005
ΔW_A (eV)	0.025	0.025
$\tau_{n,p}$ in i-region (ps)	200	200
$\tau_{n,p}$ in doped region (ps)	2	2
A_n (cm^{-1})	1.12 $\times 10^7$	6.64$\times 10^7$
B_n (V/cm)	3.11 $\times 10^6$	2$\times 10^6$
A_p (cm^{-1})	4.79 $\times 10^6$	9.34$\times 10^7$
B_p (V/cm)	2.55 $\times 10^6$	2.26$\times 10^6$
$\mu_{n,0}$ (cm^2/V sec)	6000	8000
$\mu_{p,0}$ (cm^2/V sec)	180	300
$N_{n,\text{ref}}$ (cm^{-3})	10^{17}	10^{17}
$N_{p,\text{ref}}$ (cm^{-3})	6×10^{17}	10^{18}
η_n	0.34	0.5
η_p	0.64	0.45
β (cm^2/V^2)	8×10^{-8}	8×10^{-8}
γ	1	1
α (μm^{-1})	$-$	1.15
$v_{n,\text{sat}}$ (cm/sec)	5×10^6	6×10^6
$v_{p,\text{sat}}$ (cm/sec)	6×10^6	6×10^6
m_n^*/m_0	$-$	0.041
m_p^*/m_0	$-$	0.59

Table 2.1: Material parameters at 300 K that we used in the simulations.

$$\mu = \frac{\mu_0}{1 + \left(\dfrac{N_D + N_A}{N_{\text{ref}}}\right)^{\eta}}, \tag{2.5}$$

where μ_0 is the mobility in low doping concentration, while N_{ref} and η are empirical parameters.

We use the same expression for the electron and hole diffusion coefficient that Williams [3] used,

$$D_n = \frac{kT\mu_n/q}{\left[1 - 2\left(|\mathbf{E}|/E_p\right)^2 + 4/3\left(|\mathbf{E}|/E_p\right)^3\right]^{1/4}},$$
$$D_p = \frac{kT}{q}\frac{\mathbf{v}_p(\mathbf{E})}{\mathbf{E}}, \tag{2.6}$$

where E_p is the electric field at which the diffusion constant peaks. We used $E_p = 4$ kV/cm in the simulation, with $\mathbf{v}_p(\mathbf{E})$ given by Eq. 2.4 [3].

The largest contribution to recombination is the Shockley-Read-Hall (SRH) effect. The expression for SRH recombination is

$$R = \frac{np - n_i^2}{\tau_p(n + n_i) + \tau_n(p + n_i)}, \tag{2.7}$$

where n_i is the intrinsic density, while τ_p and τ_n are the hole and electron lifetimes, respectively.

In our 2D simulations, we assume that the light intensity that is incident on the detector is a Gaussian function of the radius and enters through an opening in the n-side, anti-reflection-coated contact. Assuming that there are no reflections,
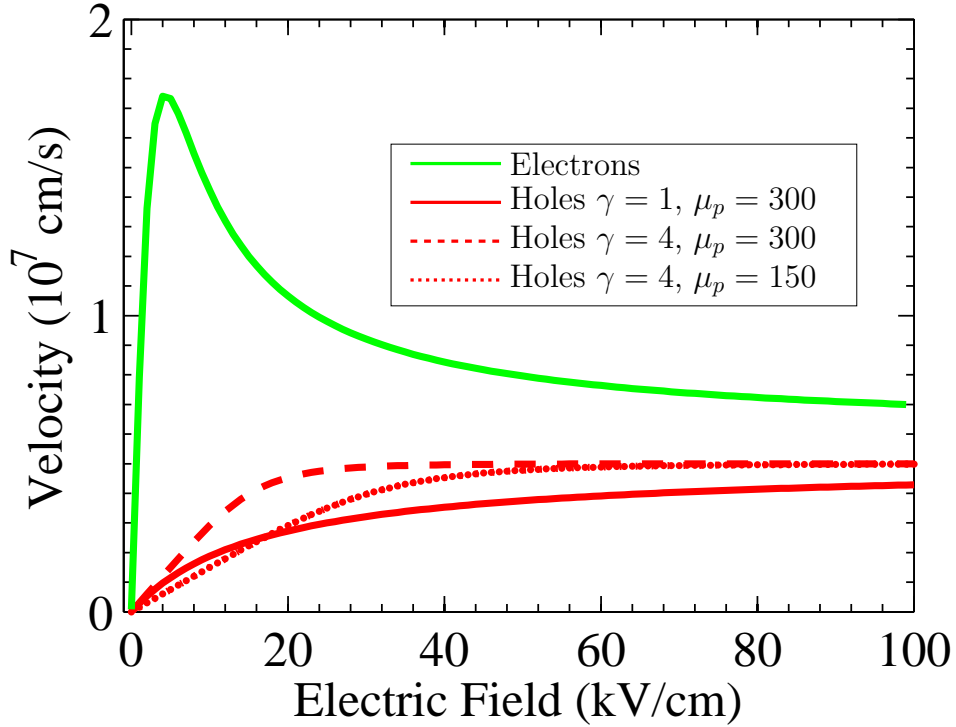
Figure 2.2: Empirical expressions for electron and hole velocities versus the electric field from Eqs. 2.3 and 2.4. We use different fitting parameters $\gamma = 1$, 4 and hole mobility $\mu_p = 150\,\mathrm{cm^2/V\text{-}s}$, $300\,\mathrm{cm^2/V\text{-}s}$. This figure is similar to Fig. 3 in Williams, et al. [2].

the generation rate from the light as a function of position in the device is expressed

as

$$G_l(r, z, t) = Q(r, t)\alpha\exp[-\alpha(w_p + w_i - z)], \tag{2.8}$$

where α is the absorption coefficient in the InGaAs and Q is the incident photon

flux, which is given by

$$Q = \frac{P}{AW_{\mathrm{ph}}}, \tag{2.9}$$

where A is the area of the light spot, and W_{ph} is the photon energy.

We will assume that the beam is Gaussian-shaped with a profile given by

$$Q(r,t) = Q_0(t)\exp\left[-2\left(r/r_0\right)^2\right], \tag{2.10}$$

where $Q_0(t)$ is the time-dependent incident photon flux and r_0 is the spot size of the light.

In the 2D model, we use the Gaussian profile in Eq. 2.10. However, in the 1D drift-diffusion model, the physical Gaussian beam profile must be approximated by a constant intensity over an effective beam area. The optical intensity is defined as the optical power per unit area. We define an effective beam diameter D_0 and an average beam intensity I_{av} such that the total power of this constant approximation is the same as the Gaussian beam, so that

$$\int_0^\infty I(r)2\pi r dr = I_{av}\pi\left(\frac{D_0}{2}\right)^2, \tag{2.11}$$

where $I(r) = I_0\exp\left(-2r^2/r_0^2\right)$ is the intensity of the Gaussian beam and r_0 is the $1/e$ beam radius of the Gaussian beam. In the 1D simulation, D_0 is a fitting parameter, and we obtain reasonable results when D_0 approximately equals $2r_0$. The principal advantages of the 2D model are that it is possible to use a realistic beam profile, and it is not necessary to define the fitting parameter D_0.

The total current output is the sum of the hole and electron currents with the addition of the displacement current averaged over the photodetector length and is

given by

$$I_{\text{total}} = \frac{1}{L} \int_0^L \int_0^R 2\pi r \left(J_n + J_p + \epsilon \frac{\partial E}{\partial t} \right) dr dz, \qquad (2.12)$$

where L is the length of the device and R is the radius of the device. While it is not necessary in principle to average over the device length since the total current is constant, we find that the average is necessary in practice to reduce computational fluctuations to an acceptable level.

To simulate nonlinearities, the photodetector is excited with a constant generation rate until the output current reaches a steady state, at which time a superimposed sinusoidal signal stimulates the device for a number of cycles, typically 10. We then take the Fourier transform of the output current to obtain the harmonic power. In several cases, we carried the simulations out to 20 cycles and observed no significant difference in the results.

The simulated light is modulated at frequency f_1 with modulation depth m and enters into the simulated photodetector. We assume that the power of the light is

$$P = P_0 \left[1 + m \sin(2\pi f_1 t) \right], \qquad (2.13)$$

where P_0 is the average light power. In the simulation, only single-pass illumination is considered.

When we solve the drift-diffusion equation in time, we obtain the output current I as a function of time. We use the Fourier transform to calculate the power at each frequency. We assume that current sequence I has N values. Then, the output

current I_f at frequency f is

$$I_f = \frac{2}{N} \left| \sum_{k=0}^{N-1} I[k] e^{i2\pi f k \Delta t} \right|, \tag{2.14}$$

where Δt is time step of the current sequence. The harmonic power P_f at frequency f is given by

$$P_f = \frac{1}{2} I_f^2 R_{\text{load}}, \tag{2.15}$$

where R_{load} is the load resistance. Usually, we measure the harmonic power H_f in units of dBm,

$$H_f = 10 \log_{10} \left(1000 P_f \right). \tag{2.16}$$

2.3 Boundary conditions and thermionic emission

To determine a set of boundary conditions, the p- and n-contacts in Fig. 2.1 are assumed to be ohmic contacts and, as such, offer no barrier to carrier flow. Hence, the carrier densities near the contacts may be approximated by their densities in the bulk region. Assuming thermal equilibrium and vanishing space charge at the ohmic contacts, the boundary conditions at the contacts are

$$p(r, 0) = N_A^-, \qquad n(r, 0) = \frac{n_i^2}{p(r, 0)}, \tag{2.17}$$

$$n(r, L) = N_D^+, \qquad p(r, L) = \frac{n_i^2}{n(r, L)}, \tag{2.18}$$

where $p(r,0)$ and $n(r,0)$ are the hole and electron densities at the contact at $z = 0$, while $p(r,L)$ and $n(r,L)$ are the hole and electron densities at the contact at $z = L$.

We set the electrostatic potential at $z = 0$ to zero, i.e., $\varphi(r,0) = 0$. We must then set the boundary conditions for φ at the other device interfaces. To determine the appropriate condition for $\varphi(r,L)$, we must take into account the load resistor. Then, the potential boundary conditions relate the given reverse bias V_a, the built-in potential V_bi,

$$V_\text{bi} = \frac{kT}{q} \ln\left(\frac{N_A^- N_D^+}{n_i^2} \right),\tag{2.19}$$

and the current in the photodetector to the electric field in the semiconductor region, so that the boundary condition for the potential is

$$\varphi(r,L) - \varphi(r,0) = \varphi(r,L) = V_\text{a} - IR_\text{Load} + V_\text{bi},\tag{2.20}$$

where I is the output current. Since the current I is unknown at the start of the simulation, we must find it iteratively. Starting with an initial guess I_0, we determine a new current I_1 using Eq. 2.20. We then use I_1 as the next guess. We can assume that the output current I is an unknown function of the bias on the device $V_D = \varphi(r,L) - \varphi(r,0)$,

$$I = f(V_D).\tag{2.21}$$

We substitute Eq. 2.21 into Eq. 2.20, and obtain

$$F(V_D) = \frac{V_D - V_a - V_{\text{bi}}}{R_{\text{Load}}} + f(V_D) = 0. \tag{2.22}$$

We then obtain the numerical derivative of $df(V_D)/dV_D$ from two initial guesses of output current I_1 and I_0,

$$\frac{df(V_D)}{dV_D} = \frac{I_1 - I_0}{V_{D1} - V_{D0}}, \tag{2.23}$$

where V_{D1} is the bias applied on the device when the output current is I_1, and V_{D0} is the bias applied on the device when the output current is I_0. We next obtain the numerical derivative of $dF(V_D)/dV_D$,

$$\frac{dF(V_D)}{dV_D} = \frac{1}{R_{\text{Load}}} + \frac{I_1 - I_0}{V_{D1} - V_{D0}}. \tag{2.24}$$

We finally use Newton's method to solve Eq. 2.22. The next guess for V_D, V_{D2}, is

$$V_{D2} = V_{D1} - \frac{I_1 R_{\text{Load}} + V_{D1} - V_a - V_{\text{bi}}}{V_{D1} - V_{D0} + R_{\text{Load}}(I_1 - I_0)}(V_{D1} - V_{D0}). \tag{2.25}$$

We iterate until the relative difference for the output current is smaller than 10^{-6}. If we further decrease the relative difference, there is no change in the simulation results.

At the boundary $r = R$, a floating boundary condition is applied. The bound-

ary conditions are

$$\left.\frac{\partial p}{\partial r}\right|_{r=0} = 0, \qquad \left.\frac{\partial p}{\partial r}\right|_{r=R} = 0,$$

$$\left.\frac{\partial n}{\partial r}\right|_{r=0} = 0, \qquad \left.\frac{\partial n}{\partial r}\right|_{r=R} = 0, \qquad (2.26)$$

$$\left.\frac{\partial \varphi}{\partial r}\right|_{r=0} = 0, \qquad \left.\frac{\partial \varphi}{\partial r}\right|_{r=R} = 0.$$

Figure 2.3: A depiction of the photodetector band diagram. This figure is similar to Fig. 3.2 in Williams [3].

Figure 2.3 shows the band diagram of the photodetector, where a reverse bias voltage of a few volts is applied to the device. The InGaAs/InP heterojunction depicted in Fig. 2.3 has a valence band discontinuity of 0.38 eV and a conduction band discontinuity of 0.23 eV [3, 41, 42]. The reduction in the conduction band discontinuity and the increase in the valence band discontinuity of approximately 0.1 eV is the result of the difference in the doping of the intrinsic and n-InGaAs layer.

23

The electrons will be allowed to flow without restriction across the heterojunction because the barrier is only 0.1 eV. However, holes are affected by the 0.5 eV barrier. We use a thermionic emission model [39, 40] to calculate the hole current at the heterojunction. We may write

$$J_p = q v_1 p_- \exp[(W_{v1} - W_{v2})/k_B T] - q v_2 p_+, \qquad (2.27)$$

where v_1 and v_2 are respectively the hole emission velocities on the left side and right side of the heterojunction, p_- and p_+ are the hole densities on the left side and right side of the heterojunction, and W_{v1} and W_{v2} are the valance band energies on the left side and right side of the heterojunction.

2.4   Additional effects

2.4.1   Incomplete ionization

The doping impurities introduced into InGaAs and InP are not fully ionized at room temperature [41]. The incomplete ionization of impurities in InGaAs and InP must be considered in a similar manner to those in silicon because the impurity energy levels are relatively deep compared to the thermal energy, so that only some of the impurities are ionized. The model accounts for the incomplete ionization of

doping impurities such as boron, aluminium, and nitrogen, using the expressions

$$N_D^+ = \frac{N_D}{1 + g_D \exp\left(\dfrac{W_C - W_D}{k_B T}\right) \exp\left(\dfrac{W_{Fn} - W_C}{k_B T}\right)},$$

$$N_A^- = \frac{N_A}{1 + g_A \exp\left(\dfrac{W_A - W_V}{k_B T}\right) \exp\left(-\dfrac{W_{Fp} - W_V}{k_B T}\right)},$$

(2.28)

where N_D^+ and N_A^- are the ionized donor and acceptor impurity concentrations, N_D and N_A are the donor and acceptor impurity concentrations, $g_D = 2$ and $g_A = 4$ are the respective ground-state degeneracy of donor and accept impurity levels, W_A and W_D are the acceptor and donor energy levels, W_C and W_V are the low conduction band and the high valence band energy levels, W_{Fn} and W_{Fp} are the quasi-Fermi energy levels for the electrons and holes, k_B is the Boltzmann constant, and T is the temperature. The energy differences in the simulation are $\Delta W_D = W_C - W_D = 5$ meV and $\Delta W_A = W_A - W_V = 25$ meV [41]. The basic variables in the drift-diffusion equations, Eq. 2.1, are the potential (or electric field), the electron concentration, and the hole concentration. Therefore, it is more convenient to rewrite Eq. 2.28 in terms of the carrier concentration instead of the quasi-Fermi levels. We use the expressions

$$N_D^+ = \frac{N_D}{1 + g_D n/n_1}, \quad N_A^- = \frac{N_A}{1 + g_A p/p_1},$$

(2.29)

where

$$n_1 = N_C \exp\left(-\frac{\Delta W_D}{k_B T}\right),$$

$$p_1 = N_V \exp\left(-\frac{\Delta W_A}{k_B T}\right),$$

(2.30)

and we make use of the expressions

$$n = N_C \exp\left(\frac{W_{Fn} - W_C}{k_B T}\right),$$

$$p = N_V \exp\left(-\frac{W_{Fp} - W_V}{k_B T}\right).$$

(2.31)

2.4.2 Impact ionization

In a strong electric field, accelerating electrons and holes can have kinetic energies that are larger than the band gap (around 1 eV for $In_{0.53}Ga_{0.47}As$ [61]), at which point a lattice collision will produce an electron-hole pair. The electron and hole move in opposite directions and can themselves produce new electron-hole pairs. With a strong electric field and an acceleration region with a sufficiently long length, this mechanism can lead to avalanche breakdown [62]. In the *p-i-n* photodetectors that we are considering, the acceleration lengths are too small to lead to avalanche breakdown since electrons leave the acceleration region too quickly. Nonetheless, this impact ionization can lead to an important increase in the electron and hole densities. We may write the electron and hole generation rate G_i as

$$G_i = \alpha_n \frac{|\mathbf{J}_n|}{q} + \alpha_p \frac{|\mathbf{J}_p|}{q},$$

(2.32)

where α_n and α_p are the impact ionization coefficients of the electrons and holes, respectively. We calculate their values using the formulae [41]:

$$\begin{aligned}
\alpha_n &= A_n \cdot \exp\left[-\left(\frac{B_n}{|\mathbf{E}|}\right)^m\right], \\
\alpha_p &= A_p \cdot \exp\left[-\left(\frac{B_p}{|\mathbf{E}|}\right)^m\right],
\end{aligned} \tag{2.33}$$

where A_n, B_n, A_p, and B_p are experimentally determined parameters [41, 42]. The exponent m is taken to be 1.05. The values that we use, shown in Table 2.1 for InGaAs, are modified slightly from the values in [41, 42] in order to obtain harmonic powers that are consistent with experiments. However, all values fall within the range of experimental error.

2.4.2.1   History-dependent impact ionization

When the intrinsic region is very thin, we have to consider the "dead length" [50] in the device. Equation 2.33 assumes that the ionization coefficient of electrons is only a function of the local electric field; this assumption will become inaccurate in thin layers. A carrier has to gain enough energy from the electric field to have an ionizing collision [50, 51]. With a decrease of the material thickness, the impact ionization coefficient should decrease [63]. In order to cause ionization, an electron must travel a finite distance, which is frequently referred to as the dead length, before it can gain sufficient energy from the electric field to lead to a non-negligible ionization probability [64, 65]. In a thin device, this dead length cannot be ignored.

We use

$$\alpha_n(x'|x) = 6.64 \times 10^7 \exp\left[-2 \times 10^6 / E_{\text{eff},e}(x'|x)\right], \tag{2.34}$$

as a history-dependent ionization coefficient [51, 64] in the simulation, where $E_{\text{eff},e}$ is defined as the average of the electric field in a neighborhood $[x, x']$,

$$E_{\text{eff},e}(x'|x) = \int_x^{x'} dx'' E(x'') R_e(x''|x). \tag{2.35}$$

The correlation function R_e is given by

$$R_e(x''|x) = \frac{2}{\sqrt{\pi}\lambda_e} \exp\left[-\frac{(x''-x)^2}{\lambda_e^2}\right], \tag{2.36}$$

where λ_e is the correlation length, expressed in terms of the voltage drop across the dead length V_{de}. In our simulations, we used $\lambda_e = V_{\text{de}}/E$, and we set V_{de} equal to 4 V as in the experiments in [64].

2.4.3 Franz-Keldysh effect

When the photon energy of the incident optical light is close to the band edge of the InGaAs absorber, the Franz-Keldysh effect must be taken into account [66]. The Franz-Keldysh effect leads to oscillations in the carrier transition probability for energies that are greater than the band gap, and it leads to tunneling of the electron state into the forbidden band due to band-bending below the band gap in the presence of an applied electric field.

The expression for the absorption coefficient α [67] is

$$\alpha = \frac{2\pi e^2}{m_e^2 c \eta' \omega} |U(0)|^2 |\langle c\mathbf{k_0}|\mathbf{e} \cdot \mathbf{p}|v\mathbf{k_0}\rangle|^2 S(\hbar\omega), \qquad (2.37)$$

where e is the magnitude of the electron charge (here positive), m_e is the electron mass, η' is the real part of the refractive index at the frequency ω, c is the speed of light, $U(\mathbf{r})$ is the solution of the effective mass equation as a function of the relative coordinate $\mathbf{r}$, $\mathbf{k}_0$ is the point in $\mathbf{k}$-space where the minimum energy gap between the conduction band c and the valence band v occurs, $\mathbf{e} \cdot \mathbf{p}$ denotes the matrix elements of the transition, $S(\hbar\omega)$ is the density of excited states at the photon energy $\hbar\omega$ above the ground state. The effective mass equation that governs the relative motion of an electron and hole pair is

$$\left(-\frac{\hbar^2}{2m^*}\nabla^2 - \frac{e^2}{\epsilon r} + eEz\right)U(r) = WU(r), \qquad (2.38)$$

where m^* is the reduced effective mass $m_e m_h / (m_e + m_h)$, ϵ is the static dielectric constant of the material, E is the electric field strength and is taken to be in the z-direction, and $W = 0$ corresponds to the gap energy W_g. The second term on the left is due to the Coulomb interaction between an electron and an hole. If we neglect this term, the solution of Eq. 2.38 can be expressed in terms of Airy functions [68].

If units are chosen so that both the exciton Rydberg energy

$$R = \frac{m^* e^4}{2\hbar^2 \epsilon^2} \qquad (2.39)$$

and the exciton Bohr radius

$$a = \frac{\hbar^2 \epsilon}{m^* e^2} \tag{2.40}$$

are unity, then the effective mass equation becomes

$$\left(-\nabla^2 - \frac{2}{r} + fz \right) U = WU, \tag{2.41}$$

where the field strength f is measured in units of (Rydbergs)/[(Bohr radius)–(electron charge)].

Equation 2.41 is not separable in spherical polar coordinates, but it is separable in parabolic coordinates defined by

$$\xi = r + z, \ \zeta = r - z, \ \phi = \phi. \tag{2.42}$$

The Laplace operator in parabolic coordinates is

$$\nabla^2 = \frac{4}{\xi + \zeta} \left[\frac{\partial}{\partial \xi} \left(\xi \frac{\partial}{\partial \xi} \right) + \frac{\partial}{\partial \zeta} \left(\zeta \frac{\partial}{\partial \zeta} \right) \right] + \frac{1}{\xi \zeta} \frac{\partial^2}{\partial \phi^2}. \tag{2.43}$$

The solution of Eq. 2.41 may be written in the form [69, 70]

$$U(r) = \frac{\chi_1(\xi)\chi_2(\zeta) \exp(im\phi)}{(\xi\zeta)^{1/2}}, \tag{2.44}$$

where m is the angular quantum number. Substituting Eq. 2.44 into Eq. 2.41 and

separating the variables ξ and ζ, we obtain

$$\chi_1''(\xi) + \left(\frac{1-m^2}{4\xi^2} + \frac{\eta}{\xi} + \frac{W}{4} - \frac{f\xi}{8}\right)\chi_1(\xi) = 0, \tag{2.45a}$$

$$\chi_2''(\zeta) + \left(\frac{1-m^2}{4\zeta^2} + \frac{1-\eta}{\zeta} + \frac{W}{4} + \frac{f\zeta}{8}\right)\chi_2(\zeta) = 0, \tag{2.45b}$$

where $\chi_1''(\xi)$ denotes $d^2\chi_1(\xi)/d\xi^2$, $\chi_2''(\zeta)$ denotes $d^2\chi_2(\zeta)/d\zeta^2$, and η is a separation

parameter. We note that the $\chi_1(\xi)$ decays exponentially when $\xi \to \infty$. Hence, the

eigenvalue η will have an infinite number of discrete values η_n, where $n = 0, 1, 2...$

is the number of nodes in $\chi_1(\xi)$. By contrast, we find that $\chi_2(\zeta)$ is oscillatory for

large ζ. We note that in Eq. 2.45b the term $(1-\eta)/\zeta$ becomes equal to $-\eta/\zeta$ when

the Coulomb interaction is not included.

The solution of Eqs. 2.44 and 2.45 begins with the specification of W, f, and

m. For the allowed transitions considered here, only the case $m = 0$ contributes

to the absorption. An approximate value of η is specified, and the asymptotic

form of $\chi_1(\xi)$ is determined by the WKBJ approximation [71, 72]. The Numerov

integrator [73] is then used to integrate inward until $\chi_1(\xi)$ has a relative maximum.

A similar outward integration is started at $\xi = 0$ with a knowledge of the behavior

of the $\chi_1(\xi)$ near the origin [71, 72],

$$\chi_1 = \xi^{(|m|+1)/2}\left\{1 - \frac{\eta\xi}{|m|+1} + O(\xi^2)\right\}. \tag{2.46}$$

The two solutions are joined at the outer maximum, and the solution from the inward

integration is scaled so that χ_1 is continuous at the joining point. We then compare

the slope of the two solutions and adjust η according to the Cooley formula [74]. We repeat the integration process until the difference of the slopes of the two solutions at the joining point converges to zero.

The asymptotic form of χ_2 as $y \to \infty$ is [71, 72]

$$\chi_2(\zeta) \to \frac{A}{(W/f + \zeta/2)^{1/4}} \sin\left[\frac{2}{3}f^{1/2}(W/f + \zeta/2)^{3/2} + \eta\right], \qquad (2.47)$$

where A is a normalization constant that we will determine shortly and η varies only logarithmically with ζ. The density of states with Dirichlet (zero) boundary conditions over a length L equals [69, 71]

$$S(W) = \frac{1}{\pi}\left(\frac{L}{2f}\right)^{1/2} \qquad (2.48)$$

for large L. The normalization constant I is evaluated from the integral expression [69, 71]

$$I^2 = \int |U|^2 J d\xi d\zeta d\phi, \qquad (2.49)$$

where the Jacobian for parabolic cylinder coordinates is

$$J = \frac{1}{4}(\xi + \zeta). \qquad (2.50)$$

We thus obtain

$$I^2 = \frac{1}{4}\int_0^{2\pi} d\phi \int_0^\infty d\xi \int_0^L d\zeta \frac{\chi_1^2(\xi)\chi_2^2(\zeta)}{\xi\zeta}(\xi + \zeta). \qquad (2.51)$$

32

In Eq. 2.51, we may set the integration limit for ξ equal to infinity because of the exponential decay of χ_1. We must choose the integration limit for ζ so that it is the same as the length that we chose to find the density of states in Eq. 2.48. This box normalization will allow us to obtain a result for the absorption coefficient that is independent of L as $L \to \infty$. In the limit as $L \to \infty$, the entire contribution to the ζ-integration will come from the asymptotic limit, which allows us to simplify Eq. 2.51. We use the asymptotic expression for the Jacobian, $J = \zeta/4$, and Eq. 2.51 becomes

$$I^2 = \frac{1}{2}\pi \int_0^\infty \frac{\chi_1^2(\xi)}{\xi}d\xi \int_0^L \chi_2^2(\zeta)d\zeta = \frac{1}{2}\pi \int_0^\infty \frac{\chi_1^2(\xi)}{\xi}d\xi (2L)^{1/2}A^2, \qquad (2.52)$$

into which we will substitute the asymptotic expression from Eq. 2.47.

The coefficient A in Eq. 2.47 is determined by solving the differential equation 2.45b for $\chi_2(\zeta)$, starting at $\zeta = 0$ with the expansion for χ_2 [69, 71],

$$\chi_2 = \zeta^{(|m|+1)/2}\left\{1 - \frac{(1-\eta)\zeta}{|m|+1} + O(\zeta^2)\right\}, \qquad (2.53)$$

and integrating outward using Numerov's method. For large ζ, we fit the calculated function to the asymptotic result in Eq. 2.47 to determine A. Substituting Eqs. 2.46 and 2.53 into Eq. 2.44, the wave function becomes

$$U(r) = \left(x^2 + y^2\right)^{|m|/2}\left\{1 + \frac{(1-2\eta)z - r}{|m|+1} + O(r^2)\right\}\exp(im\phi). \qquad (2.54)$$

The value of U is zero at the origin when $m \neq 0$ and equals one when $m = 0$. The

normalized wave function at the origin should equal

$$U_{\text{norm}}(0) = U(0)/I^2 = 1/I^2 = \left[\frac{1}{2}\pi(2L_2)^{1/2}A^2 \int_0^\infty \chi_1^2(\xi)/\xi d\xi\right]^{-1}. \tag{2.55}$$

We finally substitute Eqs. 2.48 and 2.55 into Eq. 2.37, and the absorption coefficient becomes

$$\alpha = \left(\frac{2\pi e^2}{m_e^2 c\eta'\omega}\right)\left(\frac{|\langle c\mathbf{k_0}|\mathbf{e}\cdot\mathbf{p}|v\mathbf{k_0}\rangle|^2}{A^2\pi^2 f^{1/2}\int_0^\infty \chi_1^2(\xi)/\xi d\xi}\right). \tag{2.56}$$

We define a normalized absorption coefficient

$$\bar{\alpha} = |U(0)|^2 S(\hbar\omega) = \frac{1}{A^2\pi^2 f^{1/2}\int_0^\infty [\chi_1^2(\xi)/\xi]\,d\xi}. \tag{2.57}$$

When we do not consider the Coulomb interaction in Eq. 2.37, the absorption coefficient is given by [75]

$$\alpha(\omega, W) = \left(C\theta_F^{1/2}/\omega\right)\left[\left|\frac{d\text{Ai}(\beta)}{d\beta}\right|^2 - \beta\,|\text{Ai}(\beta)|^2\right], \tag{2.58}$$

where ω is the light frequency, C is a fitting parameter, and $\text{Ai}(x)$ is the Airy function. We also have

$$\beta = \frac{\omega_1 - \omega}{\theta_F} \tag{2.59}$$

and

$$(\theta_F)^3 = \frac{e^2 W^2}{2m_{np}\hbar}, \tag{2.60}$$

where $\hbar\omega_1$ is the energy of the band gap, and m_{np} is the reduced mass of the electric-

34

hole pair.

Figure 2.4 shows the normalized absorption coefficient $\bar{\alpha}$, defined in Eq. 2.57, as a function of electric field with and without the Coulomb interaction in $In_{0.53}Ga_{0.47}As$. The field strength is measured in units of (Rydbergs)/[(Bohr radius)–(electron charge)] (Rbe). The dashed and solid curves are the simulation results with and without the Coulomb interaction, respectively. We find that the amplitude of the normalized absorption coefficient $\bar{\alpha}$ is larger by approximately a factor of two when we include the Coulomb interaction in the calculation. Since the responsivity factor $|\langle c\mathbf{k_0}|\mathbf{e} \cdot \mathbf{p}|v\mathbf{k_0}\rangle|^2$ is assumed to be unknown and is determined from a best fit to the measured responsivity, this factor of two difference is not important when comparing the theoretically calculated responsivity as a function of bias and optical wavelength to the measured values. What is important is the difference in the slope between these two calculations. For an electric field between 50 and 100 Rbe, the slope with the Coulomb interaction is larger than without. In both calculations, the oscillations become more rapid as the field diminishes, but the values at which the minima and maxima occur are different, as are the oscillation periods.

2.5 Temperature conduction model

When the photo-current increases, the temperature in the device increases, and it becomes the most important source of nonlinearity in a high current photodetector.
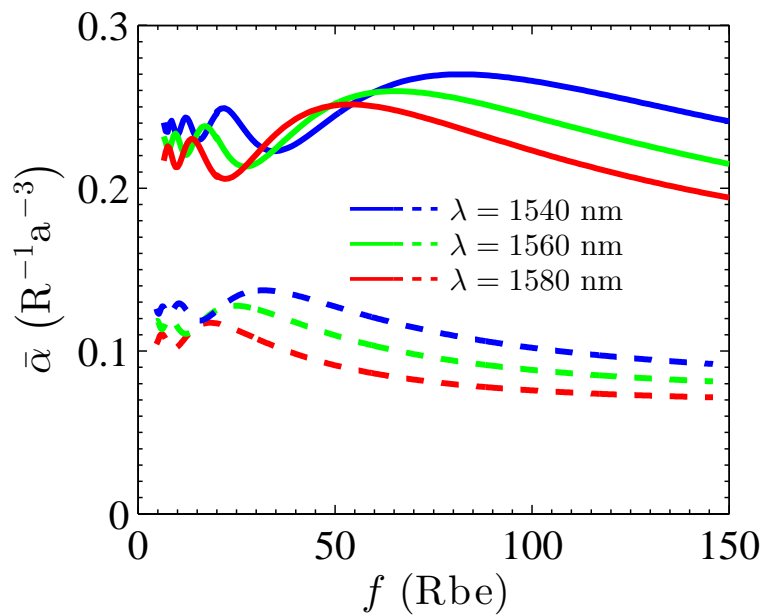
Figure 2.4: Calculated absorption coefficient as a function of electric field. The solid curves show the calculation results with the Coulomb interaction, and the dashed curves show the calculation results without the Coulomb interaction. The field strength is measured in units of (Rydbergs)/[(Bohr radius)–(electron charge)] (Rbe).

The heat flow equation [76–78] that governs the heat flow may be written as

$$\rho c_p \frac{\partial T}{\partial t} = (\mathbf{J}_n + \mathbf{J}_p) \cdot \mathbf{E} + RW_g + \nabla \cdot [k(T)\nabla T], \qquad (2.61)$$

where ρ and c_p are the specific mass density and specific heat of the material, T is the lattice temperature, W_g is the energy gap of the material, and k is the thermal conductivity. The thermal conductivity may be expressed as [77]

$$k(T) = k_{300} \left(\frac{T}{300} \right)^{\alpha_k}, \qquad (2.62)$$

where $k_{300} = 4.82$ W/K-m and α_k equals -1.17 in $In_{0.53}Ga_{0.47}As$. The electron and hole mobility and the energy gap of the material are functions of temperature; so, the heat flow equation must be included in the simulation. We solve the drift-diffusion equation and the heat flow equation iteratively to obtain the steady-state temperature distribution in the device. We calculate the band-gap W_g from the expression [76, 79, 80]

$$W_g(T) = 0.795 - \frac{4.91 \times 10^{-4} T^2}{301 + T}. \qquad (2.63)$$

The low-field mobility is given by

$$\mu_n^L = \mu_{n,300}^L \left(T/300 \right)^{r_n}, \quad \mu_p^L = \mu_{p,300}^L \left(T/300 \right)^{r_p}. \qquad (2.64)$$

Material	$\mu_{n,300}^L$, cm^2/(V-s)	r_n	$\mu_{p,300}^L$, cm^2/(V-s)	r_p
GaAs	8500	-2.2	491.5	-0.9
InAs	32500	-1.7	530	-2.3
InP	5300	-1.9	200	-1.2

Table 2.2: Material mobility parameters used in the simulation.

For material $A_x B_{1-x}$, the mobility is expressed as [80]

$$\frac{1}{\mu_{AB}} = \frac{x}{\mu_A} + \frac{1-x}{\mu_B} + \frac{x(1-x)}{C_\mu}, \tag{2.65}$$

where C_μ equals 1×10^6 cm^2/(V-s) for $In_x Ga_{1-x}As$. We show the low-field mobilities in Table 2.2 [79–81]. At room temperature, the electron mobility in $In_{0.53}Ga_{0.47}As$ equals 1.4×10^4 cm^2/(V-s), and the hole mobility equals 300 cm^2/(V-s).

The saturated velocities of the holes and electrons are also functions of temperature. These functions may be written [82]

$$v_{n,\text{sat}}(T) = \frac{v_{n,\text{sat},300}}{(1 - A_n) + A_n T/300}, \quad v_{p,\text{sat}}(T) = \frac{v_{p,\text{sat},300}}{(1 - A_n) + A_n T/300}, \tag{2.66}$$

where A_n equals 0.56 for $In_{0.53}Ga_{0.47}As$. The saturated, room-temperature electron and hole velocities that we use in our simulations are 1.2×10^7 cm/s and 0.5×10^7 cm/s, respectively.

2.6 Computational model

2.6.1 1D computational model
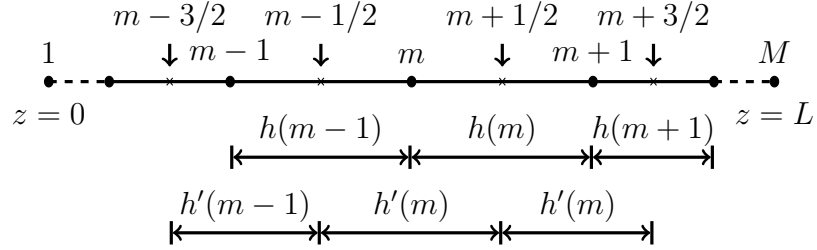
Figure 2.5: Numerical mesh used for the finite difference spatial discretization of the 1D drift-diffusion equation.

When discretizing the drift-diffusion equations for numerical computation, it is important to use a fully implicit method [45]. Explicit methods are intrinsically unstable and thus require an unreasonably small time step to yield physical results with the diffusion coefficients given in Eq. 2.6. In our simulations, the time step would be smaller than 10^{-15} s if we used an explicit method, compared with a time step of 10^{-12} s using an implicit method. We have used the implicit Euler method to discretize the equations in time t. We used second-order finite differences to discretize the spatial dimension z. We discretize the z-dimension using the mesh shown schematically in Fig. 2.5. We define p, n, and φ, at integral points in the mesh that are indexed by $m = 1, 2, ..., M$. The current and electric field are defined at intermediate points that are indexed by $m = 3/2, 5/2, ..., M - 1/2$. We use an uneven spacing between mesh points, and hence we specify the distance between the integral points m and $m+1$ as $h(m)$, and the distance between the intermediate

points $m - 1/2$ and $m + 1/2$ as $h'(m)$. We set

$$h'(m) = \frac{h(m-1) + h(m)}{2}. \tag{2.67}$$

Using this mesh, Eqs. 2.1 and 2.2 become

$$\frac{n_m^{i+1} - n_m^i}{\delta t} = \frac{1}{q} \frac{(J_n)_{m+1/2}^{i+1} - (J_n)_{m-1/2}^{i+1}}{h'(m)} + G_m^{i+1} + G_{im}^{i+1} - R_m^{i+1},$$

$$\frac{p_m^{i+1} - p_m^i}{\delta t} = -\frac{1}{q} \frac{(J_p)_{m+1/2}^{i+1} - (J_p)_{m-1/2}^{i+1}}{h'(m)}$$

$$+ G_m^{i+1} + G_{im}^{i+1} - R_m^{i+1}, \frac{1}{h'(m)} \left[\frac{\varphi_{m+1}^{i+1} - \varphi_m^{i+1}}{h(m)} - \frac{\varphi_m^{i+1} - \varphi_{m-1}^{i+1}}{h(m-1)} \right] \tag{2.68}$$

$$= -\frac{q}{\epsilon} \left(N_{Dm}^+ - N_{Am}^- + p_m^{i+1} - n_m^{i+1} \right),$$

and

$$(J_n)_{m+1/2}^{i+1} = q(D_n)_{m+1/2}^{i+1} \frac{n_{m+1}^{i+1} - n_m^{i+1}}{h(m)} + q(v_n)_{m+1/2}^{i+1} \frac{n_{m+1}^{i+1} + n_m^{i+1}}{2},$$

$$(J_p)_{m+1/2}^{i+1} = -q(D_p)_{m+1/2}^{i+1} \frac{p_{m+1}^{i+1} - p_m^{i+1}}{h(m)} + q(v_p)_{m+1/2}^{i+1} \frac{p_{m+1}^{i+1} + p_m^{i+1}}{2}, \tag{2.69}$$

where n_m^{i+1} and p_m^{i+1} are the electron and hole densities at the point m and time-step $i + 1$, respectively, while $(J_n)_{m+1/2}^{i+1}$ and $(J_p)_{m+1/2}^{i+1}$ are the electron and hole currents at the point $m + 1/2$ and time-step $i + 1$, respectively, G_m^{i+1} is the generation rate at the point m and time-step $i + 1$, R_m^{i+1} is the recombination rate at the point m and time-step $i + 1$, φ_m^{i+1} is the electrostatic potential at the point m and time-step $i+1$, N_{Dm}^+ and N_{Am}^- are the ionized donor and acceptor doping density at the point m, $(D_n)_{m+1/2}^{i+1}$ and $(D_p)_{m+1/2}^{i+1}$ are the electron and hole diffusion coefficient at the point $m + 1/2$ and time-step $i + 1$, $(v_n)_{m+1/2}^{i+1}$ and $(v_p)_{m+1/2}^{i+1}$ are the electron and

hole velocities at the point $m + 1/2$ and time-step $i + 1$. Here, we used the average carrier densities $\left(n_{m+1}^{i+1} + n_m^{i+1}\right)/2$ and $\left(p_{m+1}^{i+1} + p_m^{i+1}\right)/2$ to approximate the carrier densities $n_{m+1/2}^{i+1}$ and $p_{m+1/2}^{i+1}$ at the intermediate $m + 1/2$ point and time-step $i + 1$ in Eq. 2.69.
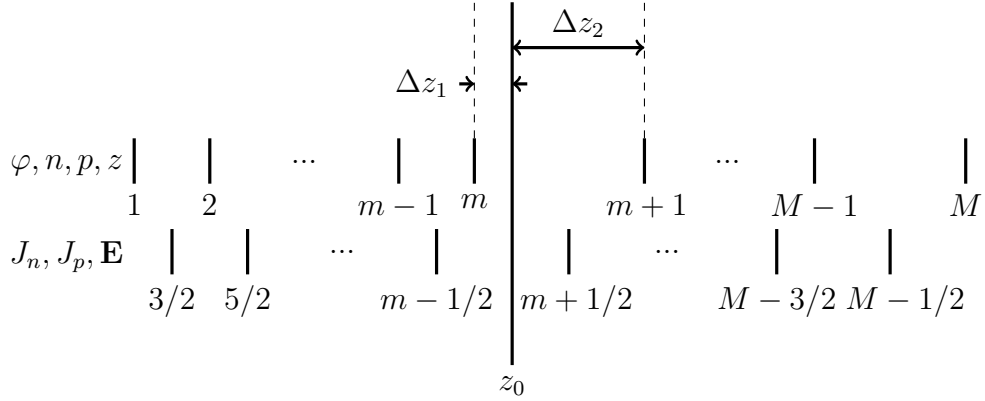
Figure 2.6: Gridding scheme used in the device model for multilayer devices.

At the heterojunction interface z_0 shown in Fig. 2.6, the discretization is different. We treat the drift-diffusion equation as a differential equation for the hole density, assuming that all other variables are constant along the grid elements introducing z_0, and we integrate over the grid elements to obtain the hole density at the interface z_0. For a grid element containing a heterojunction interface, there is a discontinuity in the hole density at this interface. So, the integration is done in two steps, first from $z(m)$ to z_0 and then from z_0 to $z(m + 1)$, as illustrated in Fig. 2.6. The drift-diffusion equation for the hole derivative, which is obtained by inserting Eq. 2.6 into Eq. 2.2b, can be written,

$$\frac{\partial p}{\partial z} = \frac{qE}{k_B T}p - \frac{EJ_p}{k_B T v_p}. \tag{2.70}$$

41

W_{c1} ——————— W_{c2}

Φ_b Φ_b

W_{v1} W_{v2}

hole motion   hole motion

Barrier to holes   No barrier to holes
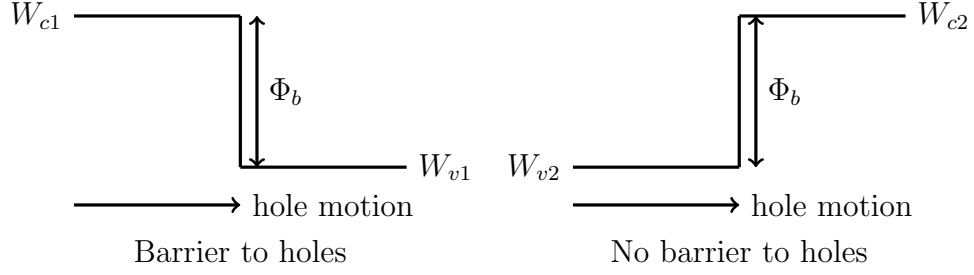
Figure 2.7: Schematic illustration of the boundary condition used at the hetero-junction. Valance band energies are denoted W_{v1} and W_{v2}, while conduction band energies are denoted W_{c1} and W_{c2}.

Integrating from $x(m)$ to x_0 yields

$$
\begin{aligned}
p(z_0^-) = p(m)\exp\left[\frac{qE(m+1/2)}{kT}\Delta z_1\right] &- \frac{J_p(m+1/2)}{qv_p(m+1/2)} \\
\times \left\{1 - \exp\left[\frac{qE(m+1/2)}{kT}\Delta z_1\right]\right\}&,
\end{aligned}
\tag{2.71}
$$

The integral from x_0 to $x(m+1)$ yields:

$$
\begin{aligned}
p(z_0^+) = p(m+1)\exp\left[-\frac{eE(m+1/2)}{kT}\Delta z_2\right] \\
- \frac{J_p(m+1/2)}{qv_p(m+1/2)}\left\{1 - \exp\left[-\frac{qE(m+1/2)}{kT}\Delta z_2\right]\right\}.
\end{aligned}
\tag{2.72}
$$

Thermionic emission [39, 40] is accounted for at the heterojunction interface. The possible barriers for holes are illustrated in Fig. 2.7. When holes move from a material with a higher valance band energy to a lower valance band energy, as shown on the left of Fig. 2.7, the heterojunction is a barrier to holes, which is the case in our structure. When holes move from a material with a lower valance band energy to a material with a higher valance band energy, as shown on the right of Fig. 2.7,

then holes move freely through the heterojunction. This kind of heterojunction is not a barrier to holes. Using Eq. 2.27, the current at the heterojunction can be written as

$$J_p(m + 1/2) = qv_1 p(z_0^-) \exp[(W_{v1} - W_{v2})/kT]$$
$$- qv_2 p(z_0^+).$$

(2.73)

Inserting Eqs. 2.71 and 2.72 into Eq. 2.73 and rearranging yields

$$J_p(m + 1/2) = qv_p(m + 1/2) \frac{A - B}{1 + C - D},$$

(2.74)

where A, B, C, and D are

$$A = p(m) \exp\left[\frac{qE(m + 1/2)\Delta z1 + W_{v1} - W_{v2}}{kT}\right],$$
$$B = p(m + 1) \exp\left[-\frac{qE(m + 1/2)\Delta z_2}{kT}\right],$$
$$C = \left\{1 - \exp\left[\frac{qE(m + 1/2)\Delta z_1}{kT}\right]\right\} \exp\left[\frac{W_{v1} - W_{v2}}{kT}\right],$$
$$D = 1 - \exp\left[-\frac{qE(m + 1/2)\Delta z_2}{kT}\right].$$

(2.75)

We have assumed that the electric field and the hole velocity are constant across the heterojunction interface.

2.6.2   2D computational model

We use the implicit Euler method to discretize the equations in time t. We use a second-order finite difference scheme to discretize the spatial dimensions r and
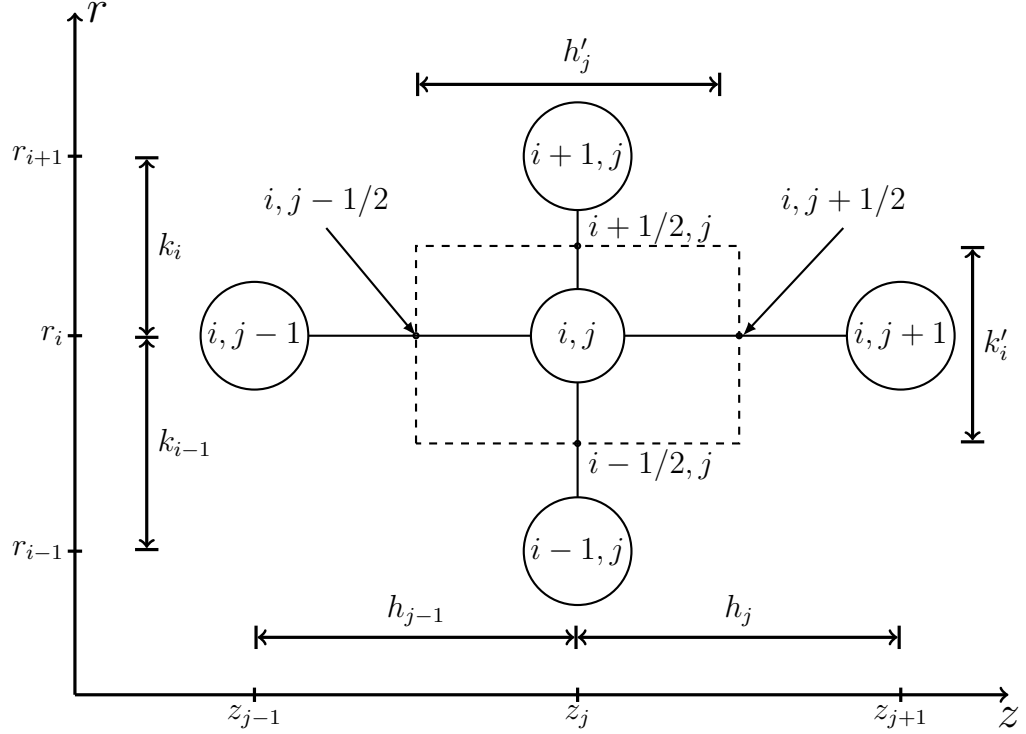
Figure 2.8: Computational mesh used for the finite difference spatial discretization of the 2D drift-diffusion equation.

z. The mesh is shown schematically in Fig. 2.8. The integral points in the mesh, labeled (i, j), are where the values of p, n, and φ are defined, while the intermediate points labeled $(i - 1/2, j)$ and $(i, j - 1/2)$ are where the current and electric field are defined. We use an uneven spacing between mesh points, and hence we specify the distance between the integral points (i, j) and $(i, j - 1)$ as h_{j-1} in the longitudinal (z) direction, and between (i, j) and $(i - 1, j)$ as k_{i-1} in the radial (r) direction. The distance between the intermediate point $(i, j + 1/2)$ and $(i, j - 1/2)$ is h'_j and between the intermediate point $(i + 1/2, j)$ and $(i - 1/2, j)$ is k'_i. We set

$$ h'_j = \frac{h_{j-1} + h_j}{2}, \qquad k'_i = \frac{k_{j-1} + k_j}{2}. \tag{2.76} $$

44

Our time step is given by δt. We thus obtain

$$\frac{n_{i,j}^{t+1} - n_{i,j}^{t}}{\delta t} = \frac{1}{q} \frac{(J_{nr})_{i+1/2,j}^{t+1} - (J_{nr})_{i-1/2,j}^{t+1}}{k_i'} + \frac{1}{q} \frac{(J_{nr})_{i,j}^{t+1}}{r_i}$$
$$+ \frac{1}{q} \frac{(J_{nz})_{i,j+1/2}^{t+1} - (J_{nz})_{i,j-1/2}^{t+1}}{h_j'} + G_{i,j}^{t+1} + G_{ii,j}^{t+1} - R_{i,j}^{t+1},$$

(2.77a)

$$\frac{p_{i,j}^{t+1} - p_{i,j}^{t}}{\delta t} = -\frac{1}{q} \frac{(J_{pr})_{i+1/2,j}^{t+1} - (J_{pr})_{i-1/2,j}^{t+1}}{k_i'} - \frac{1}{q} \frac{(J_{pr})_{i,j}^{t+1}}{r_i}$$
$$- \frac{1}{q} \frac{(J_{pz})_{i,j+1/2}^{t+1} - (J_{pz})_{i,j-1/2}^{t+1}}{h_j'} + G_{i,j}^{t+1} + G_{ii,j}^{t+1} - R_{i,j}^{t+1},$$

(2.77b)

$$-\frac{q}{\epsilon} \left(N_{D\,i,j}^{+} - N_{A\,i,j}^{-} + p_{i,j}^{t+1} - n_{i,j}^{t+1} \right) = \frac{1}{k_i'} \left[\frac{\varphi_{i+1,j} - \varphi_{i,j}}{k_i} - \frac{\varphi_{i,j} - \varphi_{i-1,j}}{k_{i-1}} \right]$$
$$+ \frac{1}{h_j'} \left[\frac{\varphi_{i,j+1} - \varphi_{i,j}}{h_j} - \frac{\varphi_{i,j} - \varphi_{i,j-1}}{h_{j-1}} \right] + \frac{1}{r_i} \frac{\varphi_{i+1,j} - \varphi_{i-1,j}}{k_i + k_{i-1}}.$$

(2.77c)

and

$$(J_{nr})_{i+1/2,j}^{t+1} = q(D_n)_{i+1/2,j}^{t+1} \frac{n_{i+1,j}^{t+1} - n_{i,j}^{t+1}}{k_i} + q(v_{nr})_{i+1/2,j}^{t+1} \frac{n_{i+1,j}^{t+1} + n_{i,j}^{t+1}}{2},$$
$$(J_{nr})_{i,j}^{t+1} = q(D_n)_{i,j}^{t+1} \frac{n_{i+1,j}^{t+1} - n_{i-1,j}^{t+1}}{k_i + k_{i-1}} + q(v_{nr})_{i,j}^{t+1} n_{i,j}^{t+1},$$
$$(J_{nz})_{i,j+1/2}^{t+1} = q(D_n)_{i,j+1/2}^{t+1} \frac{n_{i,j+1}^{t+1} - n_{i,j}^{t+1}}{h_j} + q(v_{nz})_{i,j+1/2}^{t+1} \frac{n_{i,j+1}^{t+1} + n_{i,j}^{t+1}}{2},$$

(2.78)

$$(J_{pr})_{i+1/2,j}^{t+1} = -q(D_p)_{i+1/2,j}^{t+1}\frac{p_{i+1,j}^{t+1} - p_{i,j}^{t+1}}{k_i} + q(v_p)_{i+1/2,j}^{t+1}\frac{p_{i+1,j}^{t+1} + p_{i,j}^{t+1}}{2},$$

$$(J_{pr})_{i,j}^{t+1} = -q(D_p)_{i,j}^{t+1}\frac{p_{i+1,j}^{t+1} - p_{i-1,j}^{t+1}}{k_i + k_{i-1}} + q(v_p)_{i,j}^{t+1}p_{i,j}^{t+1}, \qquad (2.79)$$

$$(J_{pz})_{i,j+1/2}^{t+1} = -q(D_p)_{i,j+1/2}^{t+1}\frac{p_{i,j+1}^{t+1} - p_{i,j}^{t+1}}{h_j} + q(v_p)_{i,j+1/2}^{t+1}\frac{p_{i,j+1}^{t+1} + p_{i,j}^{t+1}}{2},$$

where $n_{i,j}^{t+1}$ and $p_{i,j}^{t+1}$ are the electron and hole densities at the point (i,j) and time-step $t+1$, respectively, while $(J_{nr})_{i+1/2,j}^{t+1}$ and $(J_{pr})_{i+1/2,j}^{t+1}$ are the electron and hole currents at the point $(i+1/2,j)$ and time-step $t+1$ in the radial direction, respectively, $(J_{nz})_{i,j+1/2}^{t+1}$ and $(J_{pz})_{i,j+1/2}^{t+1}$ are the electron and hole currents at the point $(i,j+1/2)$ and time-step $t+1$ in the longitudinal direction, respectively, $G_{i,j}^{t+1}$ is the generation rate at the point (i,j) and time-step $t+1$, $R_{i,j}^{t+1}$ is the recombination rate at the point (i,j) and time-step $t+1$, $G_{ii,j}^{t+1}$ is the impact ionization generation rate at the point (i,j) and time-step $t+1$, $\varphi_{i,j}$ is the electrostatic potential at the point (i,j) and time-step $t+1$, $N_{D\,i,j}^{+}$ and $N_{A\,i,j}^{-}$ are the ionized donor and acceptor doping density at the point (i,j), $(D_n)_{i+1/2,j}^{t+1}$ and $(D_p)_{i+1/2,j}^{t+1}$ are the electron and hole diffusion coefficient at the point $(i+1/2,j)$ and time-step $t+1$, $(D_n)_{i,j+1/2}^{t+1}$ and $(D_p)_{i,j+1/2}^{t+1}$ are the electron and hole diffusion coefficient at the point $(i,j+1/2)$ and time-step $t+1$, $(v_{nr})_{i+1/2,j}^{t+1}$ and $(v_{pr})_{i+1/2,j}^{t+1}$ are the electron and hole velocities at the point $(i+1/2,j)$ and time-step $t+1$ in the radial direction, $(v_{nz})_{i,j+1/2}^{t+1}$ and $(v_{pz})_{i,j+1/2}^{t+1}$ are the electron and hole velocities at the point $(i+1/2,j)$ and time-step $t+1$ in the longitudinal direction.
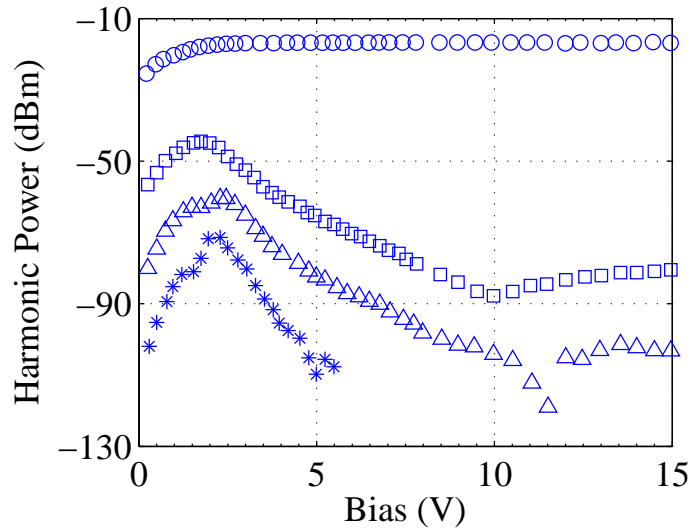
Figure 2.9: Measured harmonic power as a function of reversed bias. The output current is 1 mA, the modulation frequency is 5 GHz, and the modulation depth is 100%.

2.7 *p-i-n* photodetector simulation results

2.7.1 *p-i-n* photodetector experimental results

In Fig. 2.9, we show the harmonic power as a function of reverse bias when the output current is 1 mA. The harmonic power always decreases as the reverse bias increases from 2 to 10 V, beyond which the harmonic power saturates and can even increase slightly. From 0 to 2 V, all the harmonic powers increase because the velocity is low due to the low electric field. Around 2 V, the second, third, and fourth harmonic powers reach their peak values and then decrease. When the bias increases, the electric field in the device increases and the space charge effect diminishes, which leads to this decrease. However, at large reverse bias, we find that the harmonic powers saturate and even increase slightly. Hence, there must be

(a) Carrier densities (b) Electric field
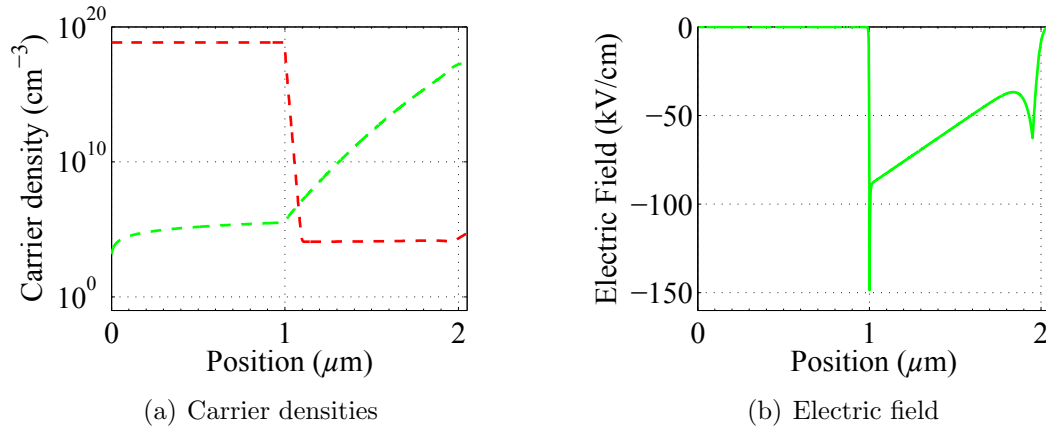
Figure 2.10: The carrier density (red denotes holes, green denotes electrons) and electric field in the steady state. The reverse bias is 5 V.

another source of nonlinearity in the device.

2.7.2 Simulation results at steady state

The parameters used in our simulations are shown in Table 2.1. We vary some parameters in order to see how they affect the results. In the following simulations, we used the parameters shown in Table 2.1 unless otherwise specified. We did not consider temperature changes for this *p-i-n* photodetector, since the output current is only 0.1 mA. The temperature increase in this device should be negligible. We also did not use a history-dependent impact ionization in the *p-i-n* photodetector because the intrinsic region is sufficiently long that the dead length is negligible.

The photodetector is reverse-biased with an applied voltage of 5 V and operates under dark (no generation) conditions. The total current is small throughout the device, governed only by the injected minority carrier density at the contacts, which is small due to the high doping densities and the reverse bias. The electric field and

carrier density are shown in Fig. 2.10.

2.7.3 Comparison between 1D and 2D simulations
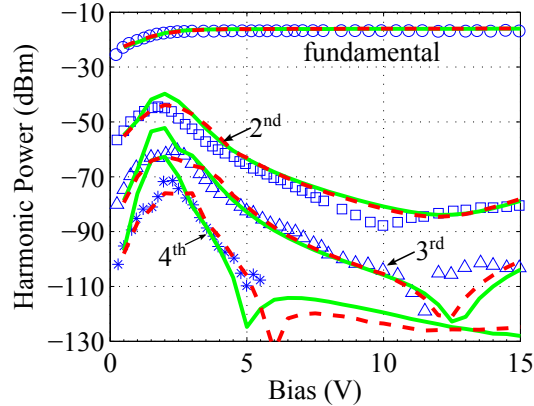
Figure 2.11: Measured (symbols) and calculated harmonic power. The green solid and red dashed curves show the results of the 1D and 2D models.

The harmonic powers that we calculated using the 1D model and 2D models are compared in Fig. 2.11. In order to match the experimental data, we set $D_0 = 8$ μm in the 1D simulations, and we set the spot size of the Gaussian beam width equal to 4 μm in the 2D simulations. Compared to the 1D results, the harmonic power in the 2D results is lower when the reverse bias is small. This difference is due to the assumption of a constant generation rate as a function of r, which is implicit in the 1D model. When r is small, the generation rate in the 2D model must be higher than the constant generation rate in the 1D model, which will induce large harmonic powers. However, when r is large, the generation rate in the 2D model becomes smaller than in the 1D model inducing carrier flow in the radial direction. This transverse flow is particularly important at low reverse bias, and we find the largest discrepancies between the 1D and 2D models when the reverse bias is less

49

(a) $\mu_p = 150$ cm^2/V-s

(b) $\mu_p = 300$ cm^2/V-s
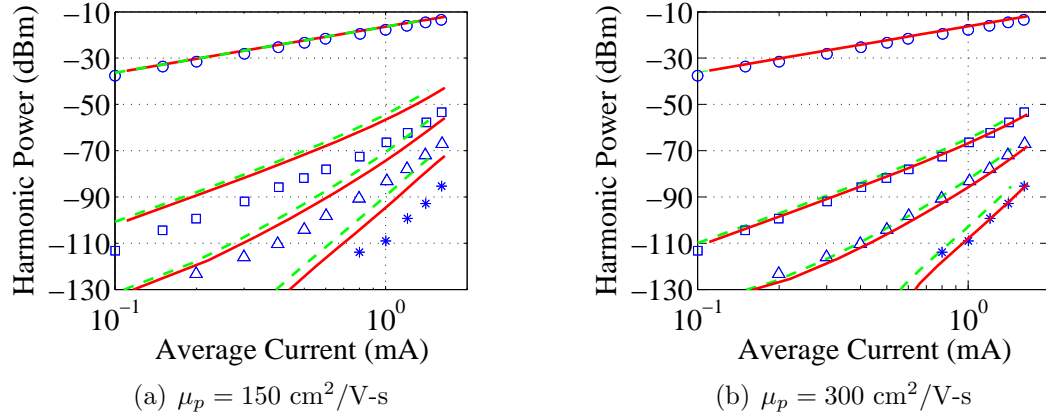
Figure 2.12: Measured and simulated powers of the fundamental, second, third, and fourth harmonics of the photodetector output current for different diameters of the light beam. The diameter of the light beam is 7 μm (green) and 7.5 μm (red). The fundamental frequency is 5 GHz, the applied reverse bias is 5 V, and $\gamma = 1$.

than 3 V.

Despite the discrepancies between the 1D and 2D models, as well as the necessity of empirically determining the parameter D_0 in the 1D model so that the results best match the experiments, the 1D model has the important advantage that it is far more rapid computationally than is the 2D model. To calculate the data in the 1D simulations in Fig. 2.11 took 30 minutes of run time on a Dell T3500 computer, while the data in the 2D simulation would have taken 60 hours of run time on the same computer that we used for the 1D simulations. Instead we used UMBC's High Performance Computing Facility (HPCF) [http://www.umbc.edu/hpcf/], which allowed us to carry out the simulations with 6 hours of run time.

2.7.4 Space-charge-induced nonlinearities dominant at low voltages

We show in Fig. 2.12 that the diameter of the beam can also influence the results. The harmonic power decreases as the diameter increases. When the diameter increases, the generation rate decreases, and a lower generation rate leads to less nonlinearity.

The two simulation results in Fig. 2.12 are from simulations that use different light beam spot sizes. The continuity equations are nonlinear because the carrier velocities are functions of the generated carrier densities. When the photodetector is dark, the electric field in the intrinsic region, plotted in Fig. 2.10, is not high enough over the entire intrinsic region to saturate the hole or electron velocities. Thus, a photo-generated space-charge electric field will induce carrier velocity variations and cause nonlinearities that in turn generate harmonics in the photodetector current. Figure 2.13 shows how the electric field changes due to the space charge in the intrinsic region with different applied reverse biases. We see that the electric field is between 30–100 kV/cm when the photodetector is dark and the reverse bias is 5 V. The space-charge-induced electric field is about 10–20 kV/cm. From Fig. 2.2, we note that velocities do not saturate until the electric field reaches about 80 kV/cm.

2.7.5 Harmonic power as a function of current

We show the harmonic power as a function of output current at 5 V in Fig. 2.14. We obtained excellent agreement with the experiments. Figure 2.15 shows the har-

(a) Reverse bias = 5 V

(b) Reverse bias = 10 V
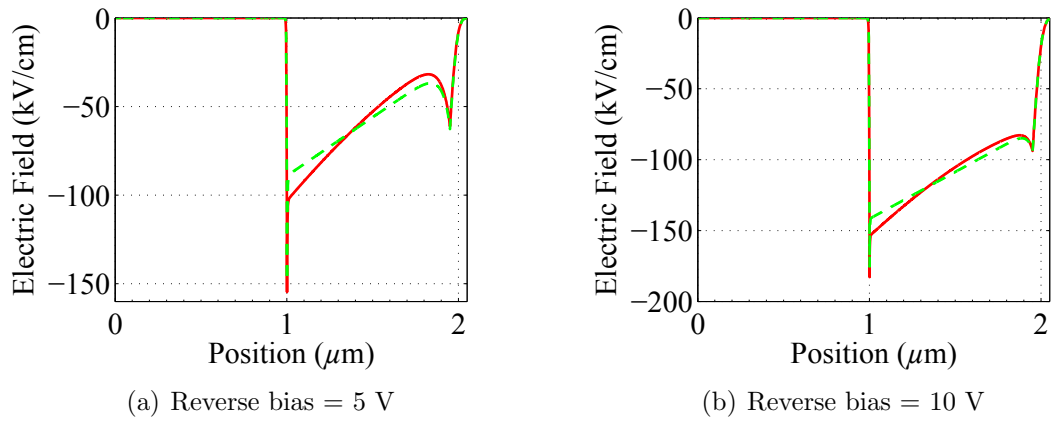
Figure 2.13: Electric field at a current of 1 mA (red-solid) and in a dark condition (green-dashed).
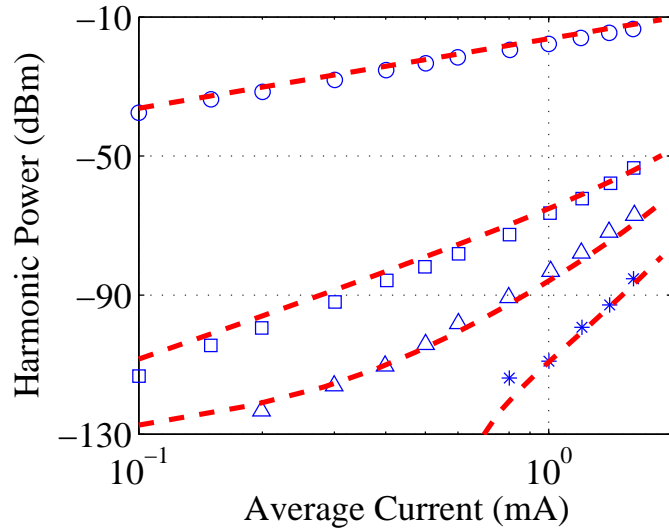
Figure 2.14: Calculated and measured harmonic power as a function of output current at 5 V. The modulation frequency is 5 GHz, and the modulation depth is 100%.
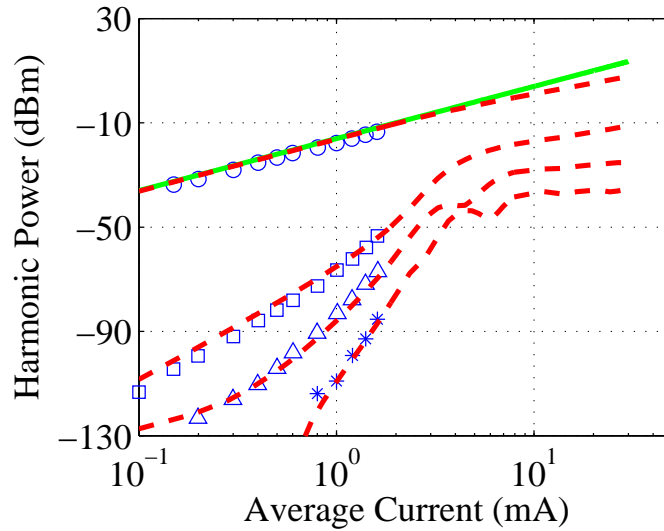
Figure 2.15: Calculated harmonic power as a function of output current at 5 V. The modulation frequency is 5 GHz, and the modulation depth is 100%. The green curve is the ideal output power.

monic power when the input power increases. The green curve is the ideal output power as a function of the output current. When the output current increases, the simulated fundamental power decreases. The output current begins to decrease due to the nonlinearity. When the photo-current increases, the space charge effect becomes more important because there is more space charge in the intrinsic region.

The harmonics should decrease as the reverse bias increases because the velocity saturates and becomes independent of the electric field strength. Figure 2.13(b) shows that the electric field stength is greater than 80 kV/cm in the intrinsic region, and therefore the carrier velocities saturate when the applied reverse bias is 10 V or more. In this limit, the drift-diffusion equations become linear. However, experiments show that the harmonic power is flat and even increases slightly in the range of 10–15 V. So, there must be one or more additional sources of nonlinearity.
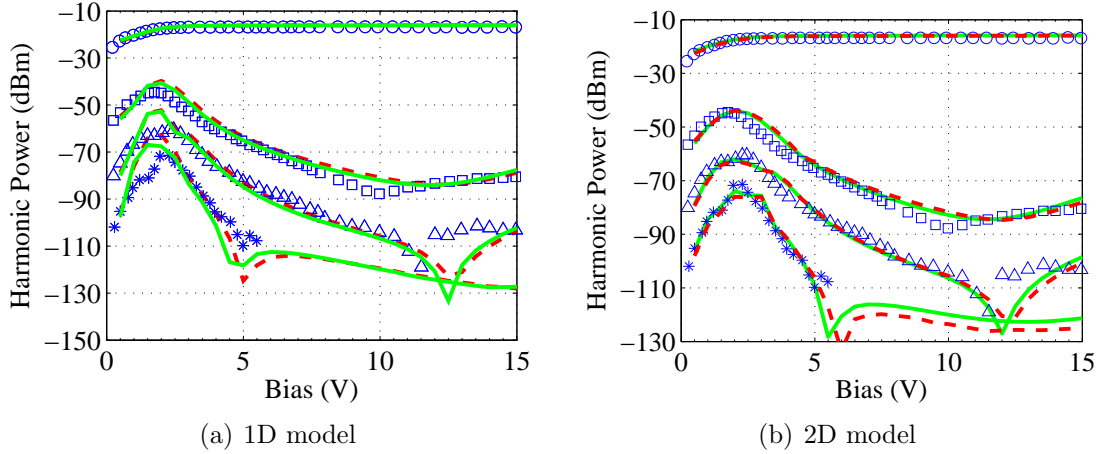
Figure 2.16: Measured and calculated harmonic powers. We compare the load resistor's influence to the harmonic power of the photodetector. The red dashed curves show the results without the load resistor, and the green solid curves show the results of keeping a 50 Ω resistor in the simulation.

2.7.6 External loading and thermionic emission

External loading is another source of nonlinearity in the photodetector. The simulation results are shown in Fig. 2.16. The results show that external loading only makes a small difference in the harmonic powers.

We expect that external loading has its greatest effect on the harmonic power when the reverse bias is low. However, it affects the harmonic power elsewhere. First, the load resistor reduces the bias that is applied to the device. For an average current of 1 mA, the potential across the resistor is 0.05 V for a 50 Ω resistor. So, the harmonic power as a function of reverse bias should shift to lower bias. Second, an external load is also a source of nonlinearity. When the generation increases in the device, there is more space charge in the depletion region, so that the electric field in the depletion region changes, leading to space-charge induced nonlinearity [2].
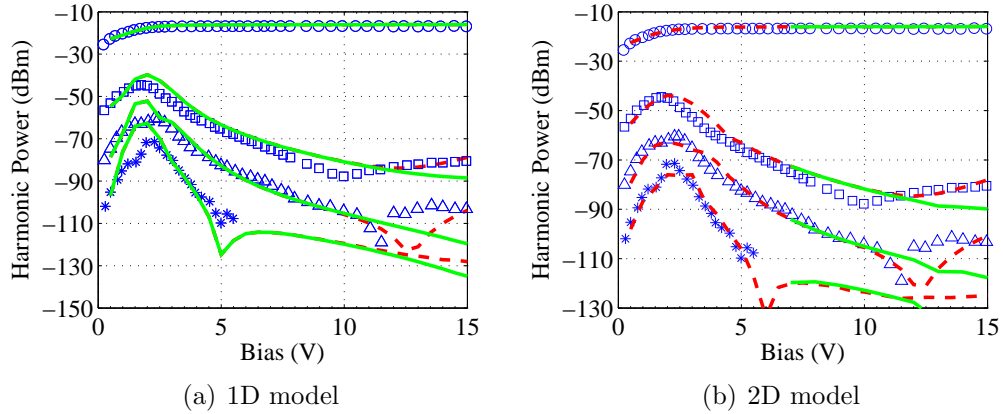
Figure 2.17: Measured and calculated harmonic powers of the photodetector output current as a function of the reverse bias. Impact ionization and a load resistor are kept in the simulations. The harmonic power is compared with (red dashed curve) and without (green solid curve) impact ionization. The red dashed curve is not visible until almost 10 V in Fig. 2.17(a) because the green solid curve lies on top of it. In Fig. 2.17(b), we only plot the green solid curve above 7 V.

When there is a large generation, the current and the bias across the resistor will also increase. So, there is less reverse bias on the photodetector, and the electric field decreases, changing the current.

In our simulations, the load resistor is not significant because the output current of 1 mA is too small to lead to a significant voltage drop across the resistor. The drop is only 0.05 V. However, we note that the load resistor becomes important when the current is large, as is the case in some modern-day devices [36, 44].

When thermionic boundary conditions are replaced by a complete barrier, as was done by Williams, et al. [3], no difference is observed in the results. So the comparison between these two models is not shown.
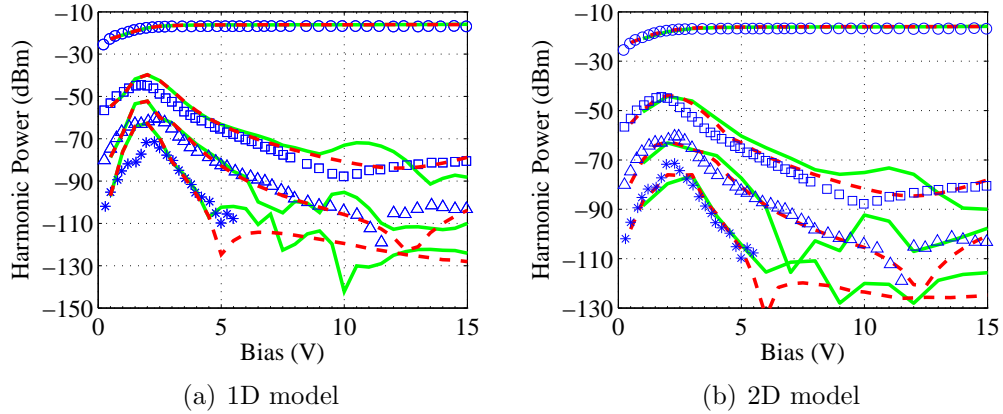
Figure 2.18: Measured and calculated harmonic powers of the photodetector output current as a function of the reverse biases with (green solid curve) and without (red dashed curve) the Franz-Keldysh effect. Impact ionization and a 50 Ω load resistor are kept in the simulations.

2.7.7 Impact ionization effect on the harmonic power

In Fig. 2.17, we show the effect of impact ionization. Below 10 V, it makes little to no difference in the results. However, above 10 V, the differences are significant, leading in most cases to an increase in the harmonic power as the reverse bias increases. It is not possible to obtain agreement with experiments without including this effect.

2.7.8 The Franz-Keldysh effect

In all the simulations that we have shown thus far, we have not included the Franz-Keldysh effect. We show the results when this effect is included in Fig. 2.18. In both the 1D and 2D models, it leads to a rapid and unphysical oscillation in the harmonic powers as the reverse bias increases. We conclude that the Franz-Keldysh effect does not play a visible role in this device. We note that the Franz-Keldysh

56

effect is a quantum coherent effect that requires maintaining phase coherence of the electron wave functions, and we also note that the light wavelength of 1319 nm corresponds to an energy of 0.94 eV, which differs significantly from the band edge of 0.74 eV. We speculate that electron-phonon, electron-carrier, and/or electron-impurity collisions are disrupting the quantum coherence that is needed for the Franz-Keldysh effect to appear in the experimental devices. The Franz-Keldysh effect is important in PDA and MUTC photodetectors [36, 44], as we will discuss in Chap. 3 and Chap. 4. of this dissertation.

2.8 Summary for the *p-i-n* photodetector

We studied 1D and 2D models of a single heterojunction *p-i-n* photodetector that are based on the drift-diffusion equations. The harmonic power in these devices decreases from 2 V to about 10 V, then saturates at around 10 V, and then in most cases increases again as the reverse bias increases. We have examined the impact of an external load, thermionic emission at the *p-i-n* interfaces, incomplete ionization, impact ionization, and the Franz-Keldysh effect at room temperature. We have found that the dominant physical cause of the observed saturation and the increase at large reverse bias is impact ionization in the simple *p-i-n* device that we studied in this chapter.

Chapter 3

Modeling a PDA photodetector

3.1   Structure of the PDA photodetector

In Fig. 3.1 and Fig. 3.2, we show the structure of the PDA photodetector that we studied. It has several absorption layers on each side of intrinsic region [46]. In InGaAs, the electron velocity is much greater than the hole velocity; this difference in carrier velocities induces device nonlinearity. In a PDA photodetector, it is possible to have a better carrier balance in the intrinsic region and reduce the built-in fields by adjusting the length of the absorption layers.
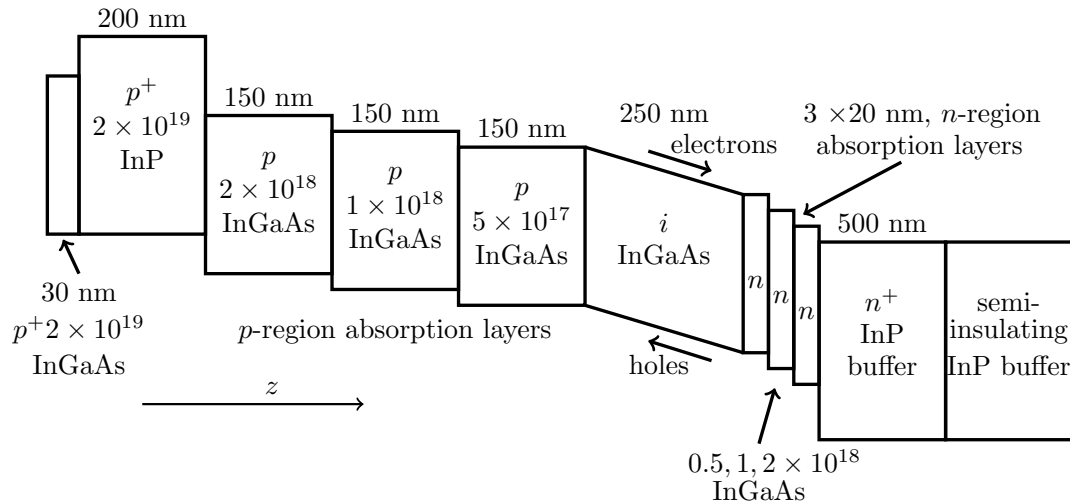
Figure 3.1: Structure of the PDA photodetector. Not drawn to scale.
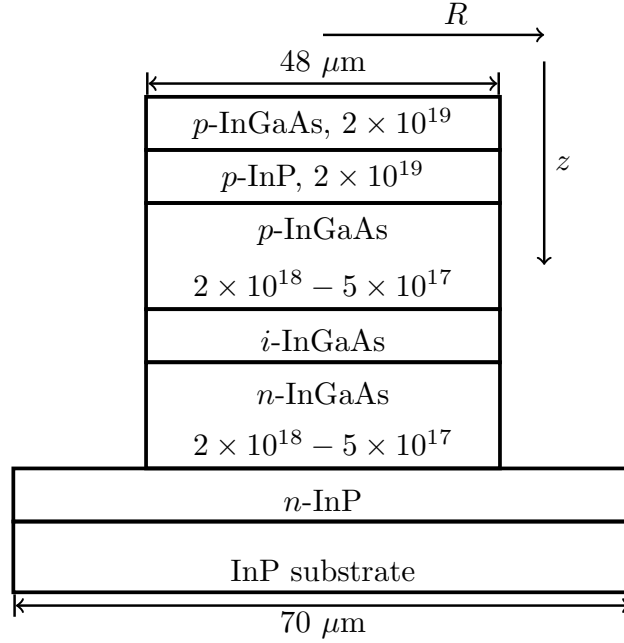
Figure 3.2: The epitaxial structure of the modeled PDA photodetector. The pillar has a diameter of 48 μm, and the base has a diameter of 70 μm. Light is incident from the InP substrate side. Lengths are not to scale.

3.2 Simulation results

We use the model that described in the Chapter 2 to calculate the device temperature, responsivity and harmonic power in the PDA photodetector.

3.2.1 Device temperature

Figure 3.3 shows the temperature in the device with a bias of 5 V. In the middle of the device, the temperature can reach as high as 370 K. The most important parameter in the device that affects the harmonic power is the InGaAs band gap. The most important region of light absorption in the device that affects the harmonic power is the intrinsic region. We calculated the average temperature in the region

of the device where the light is absorbed $\simeq$ ($z = 0.2 - 1.3$ μm). We then used

this average temperature to calculate the bandgap W_g and obtain the temperature

dependent parameters that are used in the transient calculations.
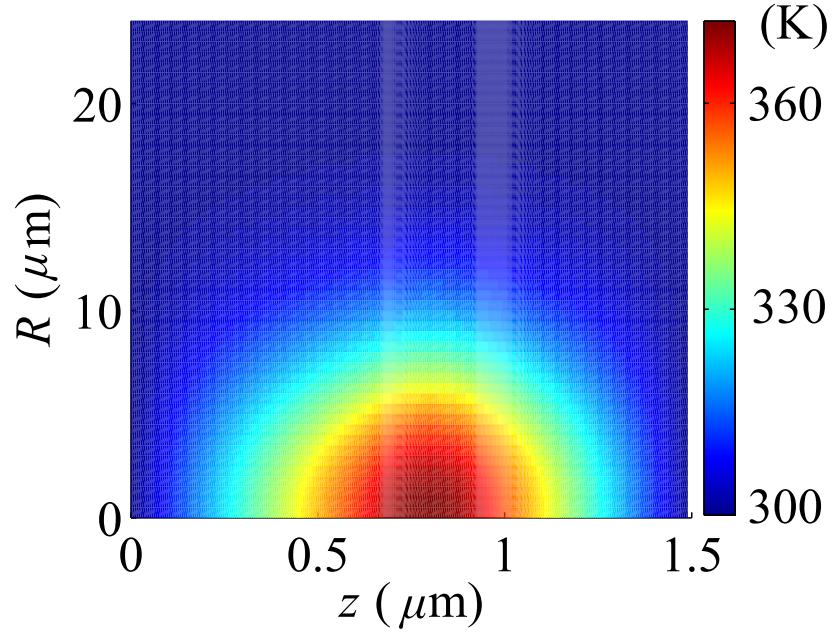
Figure 3.3: Calculated temperature in the device. The bias is 5 V and the photocurrent is 10 mA.

Figure 3.4 shows the average temperature in the light-absorption region as a

function of bias. When the bias increases, the temperature increases, leading to a

decrease in the bandgap. The velocities of the electrons and holes are also affected.

We observe that the temperature change is only 30 K when the bias increases from

2 to 5 V; however, the energy gap decreases by 0.012 eV. Without considering the

temperature increase, we cannot achieve agreement with the experiments.

Parameter		
Electron mobility in InP	$\mu_{n,300}^L$	5300 cm^2/V-s
Electron mobility in InGaAs	$\mu_{n,300}^L$	14000 cm^2/V-s
Hole mobility in InP	$\mu_{p,300}^L$	200 cm^2/V-s
Hole mobility in InGaAs	$\mu_{p,300}^L$	300 cm^2/V-s
Electron saturated velocity	$v_{n,\text{sat},300}$	1.2×10^7 cm/s
Hole saturated velocity	$v_{p,\text{sat},300}$	5×10^6 cm/s
Permittivity	ϵ	1.21×10^{-12} F/cm
Electron velocity fitting parameter in InP	β	0.8×10^{-8}cm^2/V^2
Electron velocity fitting parameter in InGaAs	β	0.4×10^{-7}cm^2/V^2
Hole velocity fitting parameter	γ	2
Intrinsic region recombination times	τ_n, τ_p	20 ns
Doped regions recombination times	τ_n, τ_p	200 ps
Optical beam Gaussian radius	r_g	12 μm
Radius of the device	R	24 μm
Donor energy level	ΔW_D	0.025 eV
Acceptor energy level	ΔW_A	0.005 eV
Light wavelength	λ	1550 nm
Electron effective mass	m_n^*/m_0	0.041
Heavy hole effective mass	m_p^*/m_0	0.43
Light hole effective mass	m_p^*/m_0	0.04
InGaAs Band gap energy at 300 K	W_g	0.72 eV

Table 3.1: Parameters used in the simulation at room temperature.
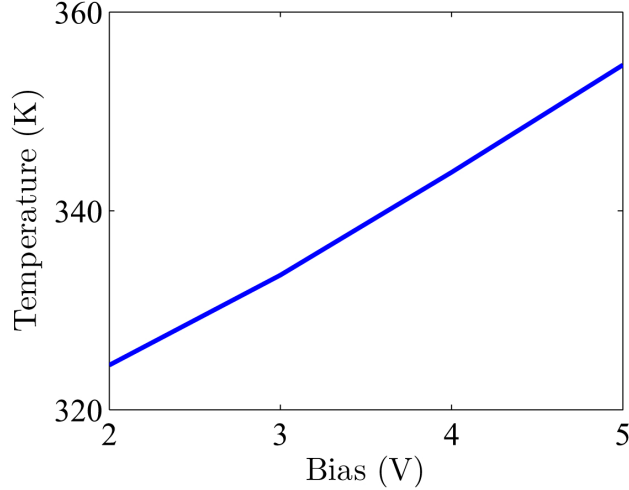
Figure 3.4: Calculated average temperature in the device. The output photocurrent is 10 mA.

3.2.2 Responsivity

Figure 3.5 shows the simulated and measured responsivity for a 9 mA output current. We obtain good agreement with the experimental results. In the simulations, we keep incomplete ionization, impact ionization, and an external load. We then calculated the harmonic power using the same parameters. The parameters that we used in the simulations are shown in Table 3.1.

We show the effect of the Coulomb interaction. We show the responsivity as a function of bias for different wavelengths in Fig. 3.6. When the bias is between 1 and 5 V, the electric field is between 4×10^6 and 2×10^7 V/cm, which corresponds to 36 to 180 (Rydbergs)/[(Bohr radius)–(electron charge)] (Rbe). Without the Coulomb interaction in the simulation, we cannot obtain agreement at 1560 and 1580 nm even with an optimal choice of the responsivity factor. When the Coulomb interaction is not included, we see in Fig. 2.4 that the absorption coefficient first decreases and then
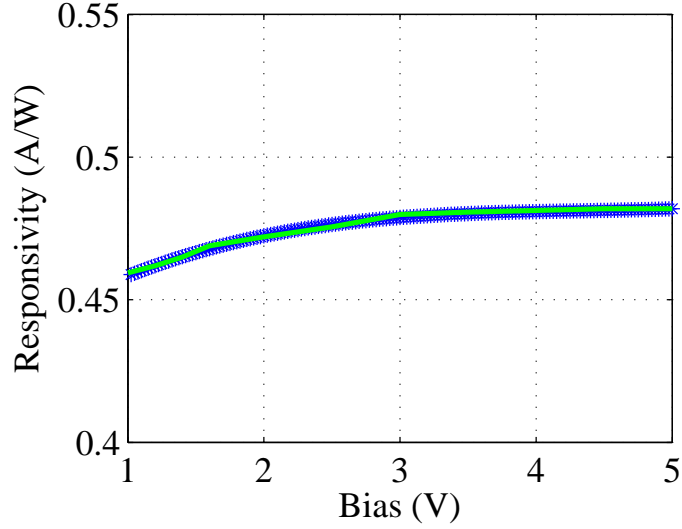
Figure 3.5: Calculated responsivity of the photodetector in our 2D simulations. The blue symbols show the experimental results, and the green curve shows the simulated result. The output photocurrent is 9 mA. The incident light wavelength is 1550 nm.

becomes flat for an electric field between 50 and 150 Rbe. Hence, the responsivity first decreases and then begins to increase at the wavelengths $\lambda = 1560$ nm and $\lambda = 1580$ nm due to impact ionization. By contrast, when the Coulomb interaction is included, the absorption coefficient always decreases for an electric field between 50 and 100 Rbe. So, the simulated responsivity decreases as the field increases, which agrees with experiments.

While the responsivity factor $|\langle c\mathbf{k_0}|\mathbf{e}\cdot\mathbf{p}|v\mathbf{k_0}\rangle|^2$ is assumed unknown and plays no role in our calculation of the responsivity, our simulations combined with the experimental measurements of the responsivity make definite predictions for this factor. Without the Coulomb interaction, we predict $|\langle c\mathbf{k_0}|\mathbf{e}\cdot\mathbf{p}|v\mathbf{k_0}\rangle|^2 = 3.11 \times 10^{-48}$ J-s, and with the Coulomb interaction, we predict $|\langle c\mathbf{k_0}|\mathbf{e}\cdot\mathbf{p}|v\mathbf{k_0}\rangle|^2 = 1.40 \times 10^{-48}$ J-s. This transition matrix element can be calculated using the procedure
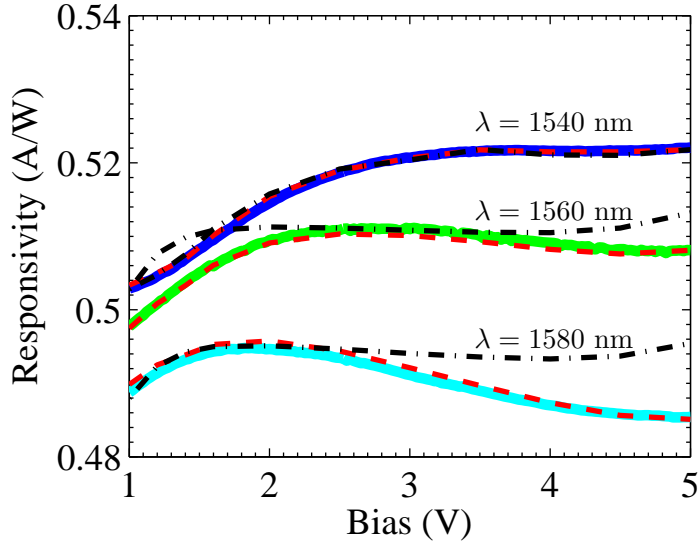
Figure 3.6: Calculated and measured responsivity as a function of bias. The solid curves show the experimental results; the dashed curves show the simulation results with the Coulomb interaction; and the dashed dot curves show the simulation results without the Coulomb interaction.

that is described in [83] and is approximately 1.51×10^{-48} J-s [84], which provides a further verification of the importance of the Coulomb interaction.

3.2.3 Harmonic power

Figure 3.7(a) shows the simulation results for the harmonic powers in the 1D simulation. The effective radius used in the simulations is 10 μm. We obtain good agreement with the experiments. Figure 3.7(b) shows the calculated harmonic powers in the 2D simulations. Here, we achieved excellent agreement with the experiments for all reverse biases. We included external loading, impact ionization, and the Franz-Keldysh effect in the simulations. The photocurrent is 10 mA, the modulation depth is 40%, and the modulation frequency is 2 GHz. The 2D simula-

Figure 3.7: Calculated harmonic powers of the photodetector output power in our 1D and 2D simulations. The symbols show the experimental data for the fundamental, second, and third harmonic powers. The dashed lines show the simulation results. The photocurrent is 10 mA, and the modulation depth is 40%. The modulation frequency is 2 GHz.

tions yield noticeably more accurate results than do the 1D simulations because the 2D simulations include transverse current flow, which is important in this device.

Figure 3.8 shows the harmonic powers in the 2D simulations at light modulation frequencies of 3.1 GHz and 4.3 GHz. We obtain excellent agreement with different modulation frequencies. We find that the fundamental power decreases when the frequency increases. This decrease occurs because the carriers respond less well to changes in the incident light as the frequency increases. The second harmonic power decreases more slowly when the frequency increases. The dip in the third harmonic power shifts from 4.0 V to 4.5 V when the frequency increases from 2.0 GHz to 3.1 GHz.

Figure 3.9(a) shows the influence of the Franz-Keldysh effect on the harmonic power as a function of the reverse bias. When the Franz-Keldysh effect is not

(a) Frequency = 3.1 GHz   (b) Frequency = 4.3 GHz
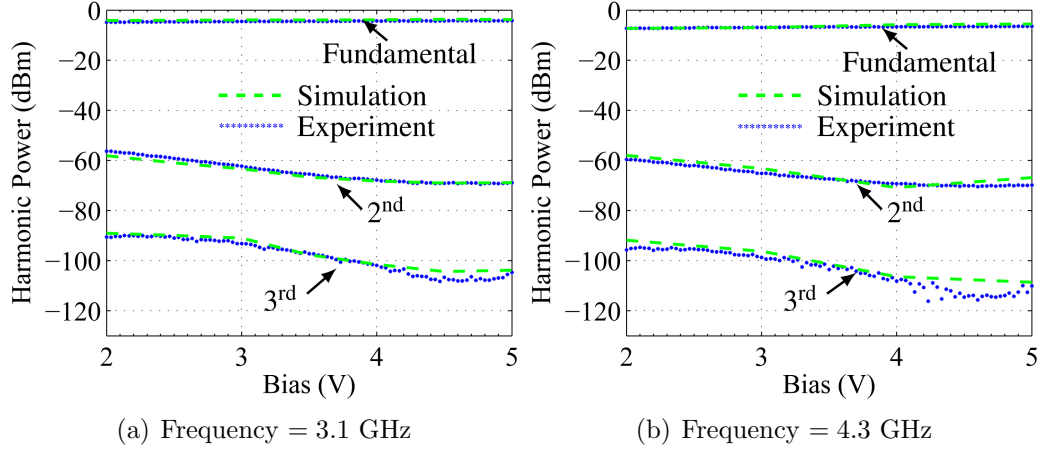
Figure 3.8: Calculated harmonic powers of the photodetector output power in our 2D simulations. The symbols show the experimental data for the fundamental, second, and third harmonic powers. The curves show the simulation results. The photocurrent is 10 mA, and the modulation depth is 40%.

(a) With 50 Ω load   (b) Without 50 Ω load
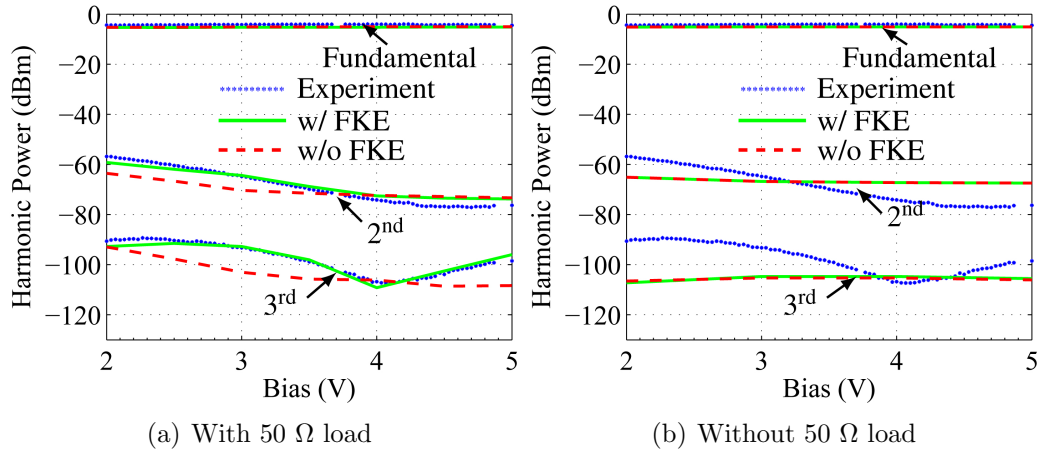
Figure 3.9: Calculated harmonic powers of the photodetector output power in our simulations. The symbols show the experimental data for the fundamental, second, and third harmonic powers. The curves show the simulation results. The photocurrent is 10 mA, the modulation depth is 40%, and the modulation frequency is 2 GHz. The green solid curves show the simulation results with the Franz-Keldysh effect (FKE), and the red dashed curves show the simulation results without the Franz-Keldysh effect.

kept in the simulation, the second and third harmonic powers in the simulation are

smaller than the experimentally-measured harmonic powers in the range from 2 V

to 4 V. This result implies that the Franz-Keldysh effect is an important source of nonlinearity in the photodetector. Without the Franz-Keldysh effect, the harmonic powers decrease as the bias increases. However, with the Franz-Keldysh effect, the harmonic powers oscillate. We observe a dip in the third harmonic power when the bias is close to 4 V.

Photogenerated carriers change the electric field and hence the absorption coefficient, which leads to changes in the output photocurrent. Due to the load resistor in the circuit, the voltage across the device changes so that the electric field in the device changes. When the load resistance is zero, Fig. 3.9(b) shows the harmonic powers with and without the Franz-Keldysh effect. Without the load resistor in the measured circuit, the voltage across the device is determined by the applied voltage. The electric field in the intrinsic region only changes slightly due to the change of the absorption coefficient. So, the Franz-Keldysh effect by itself makes little difference. It is the load resistor combined with the Franz-Keldysh effect that is the source of nonlinearity in the photodetector.

3.3   Other issues

3.3.1   Impact of the base radius

Figure 3.10 shows the harmonic powers for different geometries of the photodetector. The green curves represent the simulation results with the structure shown in Fig. 3.2, in which the radius of the bottom layer (n-InP layer) of the device is larger (35 μm) than other layers (24 μm), and the red curves represent a uniform
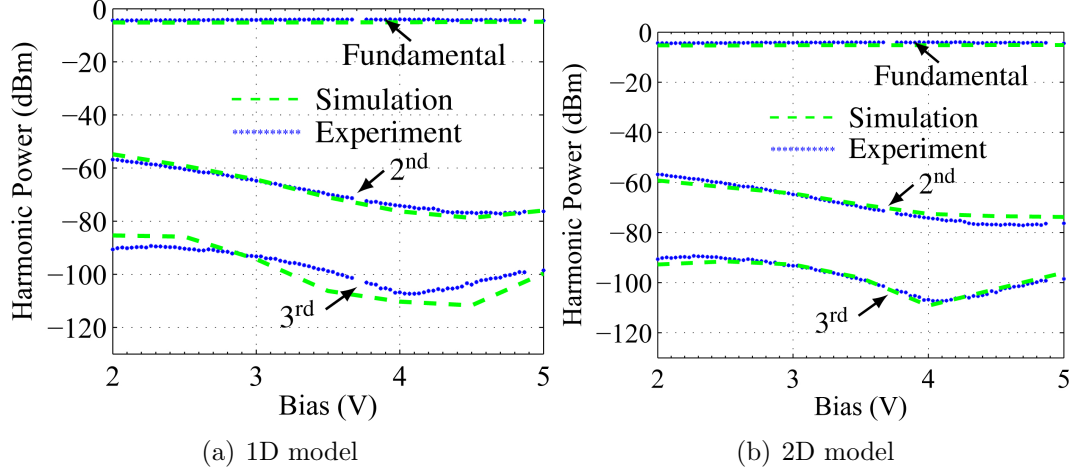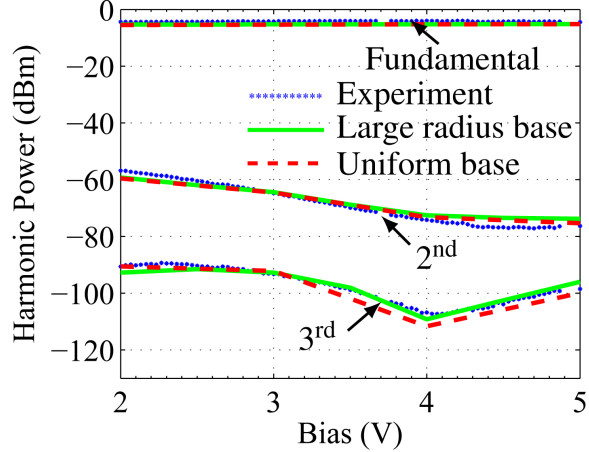
Figure 3.10: Calculated harmonic powers of the photodetector output power in our 2D simulations. The symbols show the experimental data for the fundamental, second, and third harmonic power. The green solid curves show the simulation results when the base has a larger radius (green) and the same radius (red) as the other layers in the device. The photocurrent is 10 mA, the modulation depth is 40%, and the modulation frequency is 2 GHz.

device, in which we assume that all layers in the device, including the base, have the same radius (24 μm). The simulation results show that changing the size of the base does not make much difference. The reason that changing the size of the base does not matter much is that the nonlinearity is primarily created in the p- and intrinsic layers. Hence, we can use a relatively simple structure to calculate the harmonic powers in the device.

The actual device that we are modeling is not cylindrically symmetric, as we assume in our 2D simulations. Instead, it sits on a pedestal with the electrical contact on one side of the device. A full 3D simulation that models the actual geometry is too computationally time-consuming to allow us to carry out parameter studies. This result, which indicates that the behavior is largely independent of the geometry of the base, increases our confidence in the 2D simulations.

3.3.2 Validation of the Franz-Keldysh effect model

The Franz-Keldysh effect is a spatially extended effect that is due to tunneling of electrons through a barrier [66]. Here, we verify that the change in the field is small over the spatial extent of the Franz-Keldysh effect and will not affect the calculation of this effect. In order for the change in the field to be sufficiently small, the absorption length due to the Franz-Keldysh effect l_A should satisfy the condition

$$\frac{1}{l_A} \gg \max \left| \frac{1}{E} \frac{dE}{dz} \right|, \tag{3.1}$$

where

$$l_A = \left(\frac{\hbar^2}{2e\mu E} \right)^{1/3}. \tag{3.2}$$

The absorption coefficient is obtained from a dimensional analysis of the 1D two-particle Schrödinger equation [85]

$$[(\hbar^2/2\mu)\nabla^2 + |e|Ez + W]\Phi(r) = 0, \tag{3.3}$$

where E is the electric field in the z direction, W is the sum of the electron and hole energies measured from their respective band edges, and μ is the reduced mass that is defined by

$$\frac{1}{\mu} = \frac{1}{m_h^*} + \frac{1}{m_e^*}. \tag{3.4}$$

As an example, we set the bias equal to 2 V. We assume that the electric field in the intrinsic region is uniform, and the strength of the electric field should be

approximately 1×10^7 V/m. Equation (3.2) then implies $l_A = 5.04 \times 10^{-9}$ m, and $1/l_A = 1.98 \times 10^8$ m^{-1}. Figure 3.11(a) shows $(1/E)(dE/dz)$ in the intrinsic region. We see the Eq. (3.1) is always satisfied. Figure 3.11(b) shows the electric field in the device as a function of z. We can see that the electric field is almost zero in the p-region except at the interface between the different layers.

(a) $(1/E)(dE/dz)$ (b) electric field
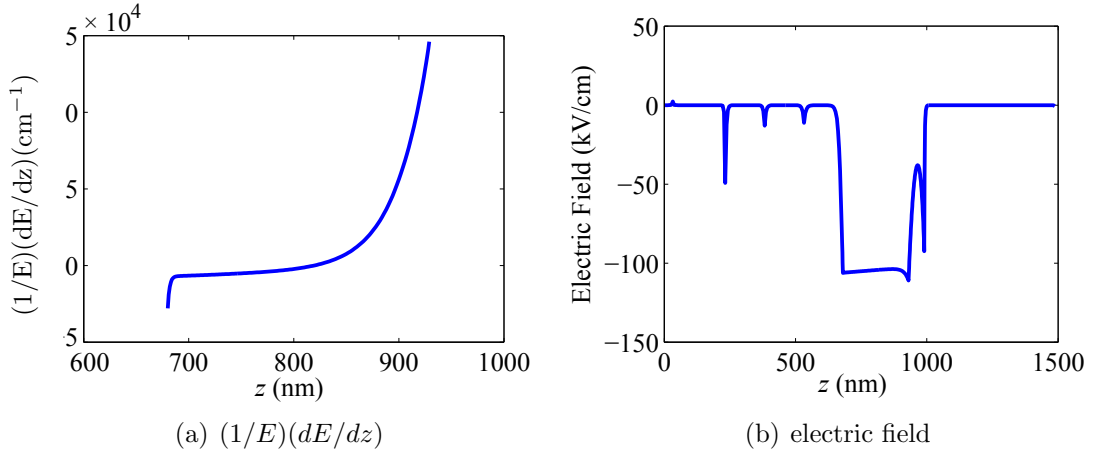
Figure 3.11: (a) The function $(1/E)(dE/dz)$ in the intrinsic region. (b) The electric field distribution in the device in the z-direction.

3.3.3 History-dependent impact ionization

Figure 3.12 shows calculated harmonic powers when we use the local field-dependent impact ionization given in Eq. (2.33), which does not take take the dead length into account. For comparison, we also show the harmonic powers when we take into account the history-dependence impact ionization. The local field-dependent impact ionization overestimates the impact ionization coefficient in the device. Since the intrinsic region of this photodetector is only 250 nm, the dead length effect [50] cannot be ignored, and we must use a history-dependent ionization.
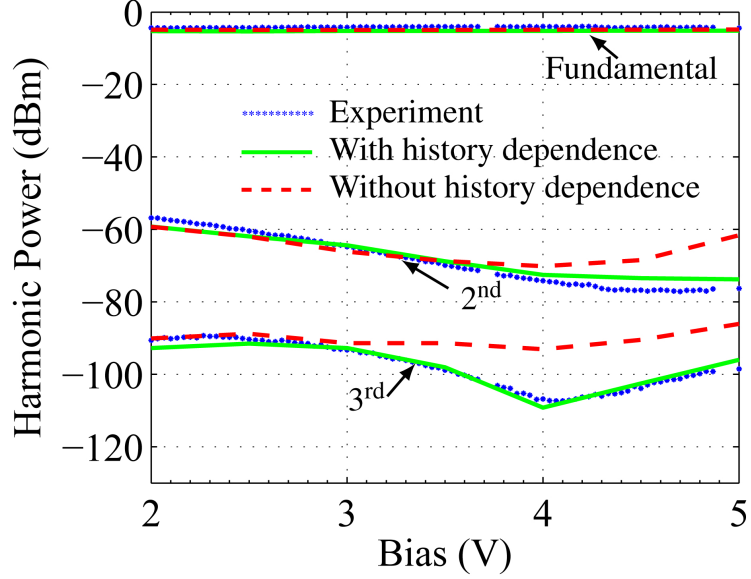
Figure 3.12: Calculated harmonic powers when we use the impact ionization Eq. (2.33), which has no history dependence

Figure 3.13 shows the responsivity using the local field-dependent impact ionization. When the history dependence is not included and the bias is greater than 4 V, we find that the calculated responsivity is higher than the experimental responsivity. Our simulations show the impaction ionization does not make an important contribution to nonlinearity in this device, which is consistent with the results in [36]. However, without using the history-dependent impact ionization in the simulation, the model will overstate the importance of the impact ionization. Thus, it is important to use the history dependent impact ionization in order to accurately determine its importance.
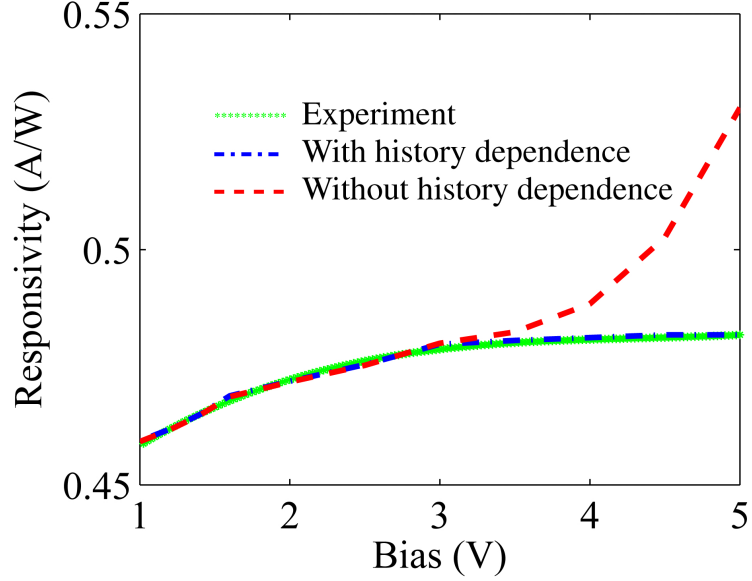
Figure 3.13: Calculated responsivity of the photodetector in our 2D simulation. The green dotted curve shows the experimental results, the blue dash-dot curve shows the simulated result with history-dependent impact ionization, and the red dashed curve shows the simulated result without history-dependent impact ionization. The output current is 9 mA. The incident light wavelength is 1550 nm.

3.3.4 Suggestions for improving device performance

The Franz-Keldysh effect in the intrinsic region is an important source of nonlinearity in this photodetector. It plays almost no role in the other device regions, because the electric field is nearly zero outside the intrinsic region and does not change with the photo-generated carriers. It is therefore advantageous to maximize the absorption in the p-region, which may be done by increasing its length. The absorption in the intrinsic region decreases for the same output photocurrent when the length of the p-region absorption layers increases. The change of the electric field in the intrinsic region that is due to the photo-generated carriers decreases. So, the nonlinearity in the intrinsic region decreases. Figure 3.14(a) shows the calculated

harmonic powers when we double the length of the *p*-region absorption layers. The harmonic powers decrease by about 5 dB between 2 and 4 V. These curves are similar to the simulation results without the Franz-Keldysh effect, as shown in Fig. 3.9(a).

(a) *p*-region absorption layers   (b) intrinsic region
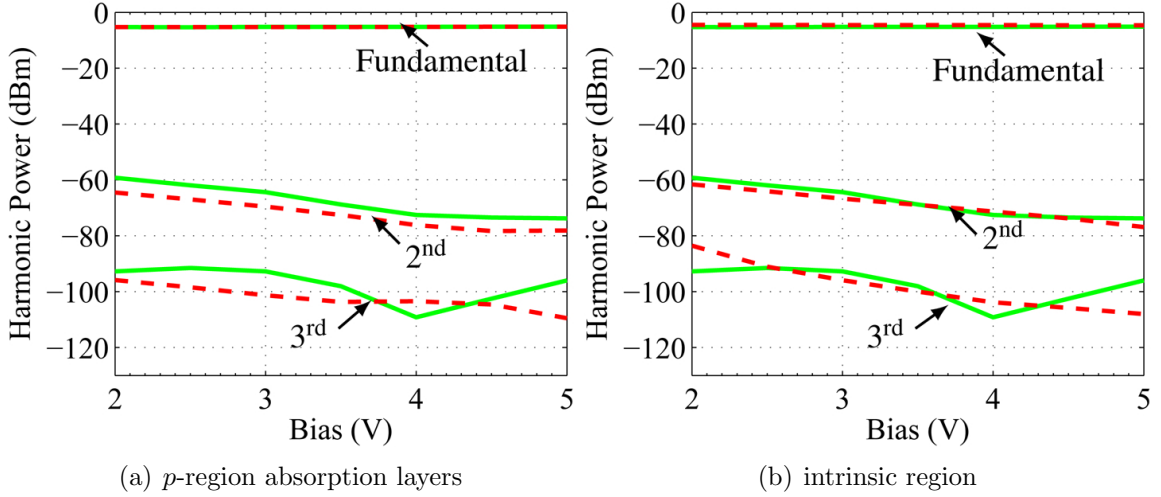
Figure 3.14: Calculated harmonic powers when we double the length of (a) the *p*-region absorption layers (red dashed curves) and (b) the intrinsic region (red dashed curves). For comparison, we also show the original calculation as green solid curves.

Figure 3.14(b) shows the calculated harmonic powers when we double the length of the intrinsic region. The strength of the electric field decreases when the length of intrinsic region increases, increasing the period of the Franz-Keldysh oscillations in the absorption coefficient. We find that the harmonic powers decrease somewhat at high bias when we increase the length of the intrinsic region. However, increasing the intrinsic region will increase the transit time and space charge effect.

Figure 3.9(b) indicates that the third harmonic power decreases without the load resistor. It is not possible in practice to make the load resistance zero. However, we note that the photodetector is close to an ideal current source and operates most linearly with a fixed bias across the device. For narrowband applications,

it is possible to use impedance matching to reduce the effective load resistance and increase the linearity of the device. Figure 3.15 shows the calculated harmonic powers with differing load resistances. We are assuming that an impedance-matching circuit is used to match the effective load resistance to the final load, which is held at 50 Ω, so that the power dissipation is given by $I^2/2 \times 50$ Ω. Decreasing the effective load resistor decreases the third harmonic power significantly at biases below 4 V. When the bias decreases, the voltage across the load resistor become larger relative to the voltage across the photodetector, which increases the effect of the load resistor on the third harmonic power generation.
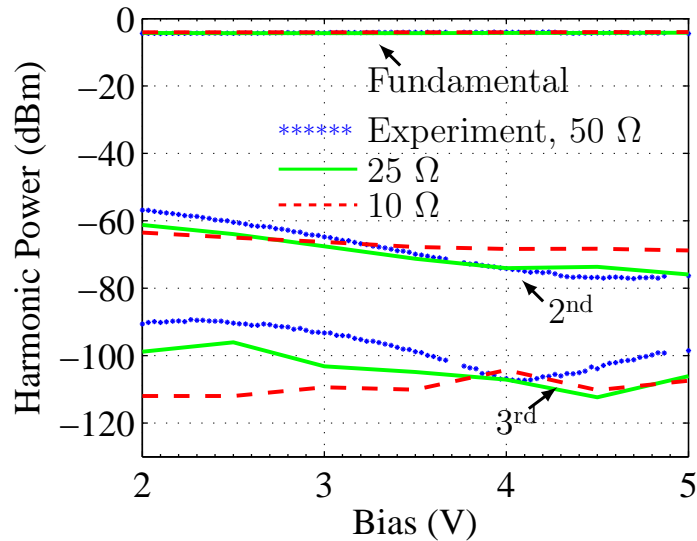
Figure 3.15: Calculated harmonic powers with effective load resistances of 10 and 25 Ω.

Another possibility that we considered for reducing the impact of the Franz-Keldysh effect is to increase the so-called "unintentional" doping density in the intrinsic region. Figure 3.16 shows the calculated harmonic powers when we increase the doping density to 5×10^{15} cm^{-3}. We find that the second harmonic power is
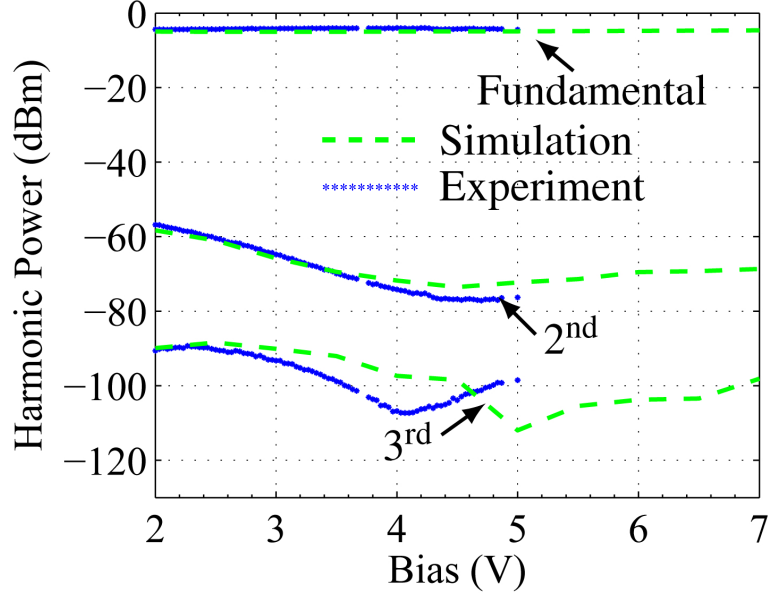
Figure 3.16: Calculated harmonic powers when the doping density in the intrinsic region is 5×10^5 cm^{-3}.

almost the same. The dip in the third harmonic power shifts from 4 V to around 5 V. However, we do not see any decrease in the harmonic powers. So, this approach does not succeed for this structure. We attribute this result to an increase in the dark current when the doping density in the intrinsic region increases.

We found that the Franz-Keldysh effect plays an important role in the device nonlinearity. We can mitigate the effect of the Franz-Keldysh effect by increasing the length of the p-region absorption layers. The change of the absorption coefficient principally occurs in the intrinsic region. The absorption in the p-region absorption layers remains the same because the electric field does not change with the incident light power. Increasing the length of the p-region absorption layers therefore decreases the nonlinearity due to the Franz-Keldysh effect.

It would be helpful to measure the output photocurrent with a fixed applied

voltage across the device. With the load resistor in the measured circuit, it is difficult to fix the voltage across the device when the photocurrent changes. However, the harmonic powers decrease when we decrease the load resistor. The third harmonic power decreases by more than 10 dB when the load resistor is 10 Ω.

3.4   Summary for the PDA photodetector

We have developed a 2D drift-diffusion model to study nonlinearity and harmonic power generation in a PDA photodetector. The heat flow equation was included in the model to study the effects of temperature change as a function of bias. We have shown that history-dependent impact ionization is important in this PDA photodetector, which has a thin intrinsic region. Without history-dependent impact ionization in the model, the effect of impact ionization is overestimated, and we cannot obtain agreement with experiments for either the responsivity or the harmonic powers. We also achieved excellent agreement with the experiments at different modulation frequencies.

We found that the Franz-Keldysh effect plays an important role in the device nonlinearity. We can mitigate the Franz-Keldysh effect by increasing the length of the p-region absorption layers. The change of the absorption coefficient occurs principally in the intrinsic region. The absorption in the p-region absorption layers remains the same because the electric field does not change with the incident light power. Increasing the length of the p-region absorption layers therefore decreases the nonlinearity due to the Franz-Keldysh effect. However, increasing the length of

the p-region absorption layers also increases the recombination, leading to a tradeoff.

It would be helpful to measure the output photocurrent with a fixed applied voltage across the device. With the load resistor in the measured circuit, it is difficult to fix the voltage across the device when the photocurrent changes. However, the harmonic powers decrease when we decrease the load resistor. The third harmonic power decreases by more than 10 dB when the load resistor is 10 Ω.

Chapter 4

Modeling an MUTC photodetector

A unitraveling-carrier photodiode (UTC) [4] only uses electrons as a traveling carrier in the device. The UTC photodetector can achieve a higher speed and higher output than devices that use both electrons and holes as carriers because the velocity of an electron is larger than velocity of a hole in InGaAs by about a factor of two. The band diagram of a UTC photodetector is shown schematically in Fig. 4.1.
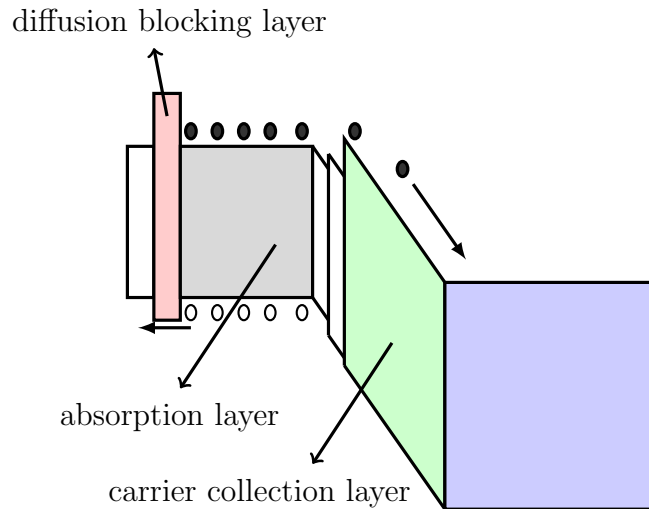
Figure 4.1: A depiction of the photodetector band diagram. Black circles represent electrons, and white circles represent holes. Red indicates the diffusion blocking layer, purple indicates the absorption layer, green indicates the collection layer made of InP. The slope of the band diagram is due to the built-in electric field in the intrinsic region. This figure is similar to Fig. 1 in Ito [4].

The main difference between a *p-i-n* photodetector and a UTC photodetector is the position of the absorption layer. In the *p-i-n* photodetector, the depleted region and the *p*-region are used as the absorption layers. The holes have to travel

through the entire intrinsic region and p-region to reach the p-contact. So, the response time of a p-i-n photodetector is determined by the velocity of the holes. In a UTC photodetector, the only absorption layer is the p-region. The intrinsic region is used as a collection layer. Photogenerated majority holes quickly diffuse to the p-contact. The photo-generated minority electrons in the absorption layer diffuse (and/or drift) into the depleted collection layer. Therefore, the response time of a UTC photodetector is determined only by the electron transport in the device. There is a diffusion blocking layer on the p-side of the absorption layer to block electrons from diffusing to the p-contact. Between the absorption layer and the collection layer, a graded energy gap helps the electrons transit through the interface and thus reduces the transport time.

An advantage of a UTC photodetector is its rapid response time, which can be enhanced without reducing the responsivity. The widths of the absorption layer and the collection layer can be designed independently. It is possible to achieve a large bandwidth without reducing the responsivity by designing a thin intrinsic absorption layer. By contrast, decreasing the width of the absorption layer in a p-i-n photodetector decreases the responsivity.

Another advantage of a UTC photodetector is a high output saturation current because of the reduced space charge effect. In the depletion region, the electron is the only carrier, so that transport is faster than if holes are present, and the output saturation current is an order of magnitude higher than is the case for a p-i-n photodetector [86]. Even at zero bias, the UTC photodetector has a higher speed and a higher output current because an electron can maintain high speed with a low

electric field, such as the built-in electric field.

To date, a record 3-dB bandwidth of 310 GHz and a millimeter-wave output power of over 20 mW at 100 GHz have been achieved [4] using a short pulse and an effective load of 12.5 Ω. With a 50 Ω load, Rouvalis et. al [87] demonstrated an output power of -9 dBm at 200 GHz.

An InGaAs/InP MUTC photodetector has been designed by Z. Li et al. [88]. Figure 4.2 shows the MUTC structure [88]. The main difference between this structure and a UTC photodetecter is that there is a cliff layer between the collection layer and the absorption layer. The cliff layer is moderately doped. The electric field has a large magnitude in the InGaAs intrinsic layer compared to the other photodetector regions. Hence the space charge effect is reduced. Another difference is that there is a thin intrinsic layer of InGaAs, which is used to increase the responsivity.

4.1 Displacement current and intermodulation distortion

Asymmetries in the amplitudes of the lower and upper intermodulation distortion (IMD) tones are often observed in microwave devices that are subjected to two-tone or three-tone tests. These asymmetries are also observed in the photodetector measurement [89, 90]. In a three-tone measurement, where the modulation frequencies are F_1, F_2, and F_3, the IMD power that is associated with the frequency combination $F_1 + F_2$ is different from the one at $|F_1 - F_2|$. In particular, the bias voltage at which a null occurs (bias null) in the IMD is different. It has been suggested that frequency dependence of the IMD power may be due to a memory effect, i.e.,

a bandwidth-dependent nonlinear effect. There are several studies of the memory effect on a microwave amplifier [91, 92], but the physical reason for the IMD power difference in a photodetector remains unclear. We will use the drift-diffusion model to show that the asymmetry is due to the displacement current.

A three-tone setup [93] was used to measure the harmonic powers in the device. The device output power was measured as a function of reverse bias voltage from 0–10 V in 0.25 V increments. The frequencies are 4.9 GHz, 5.0 GHz, and 5.15 GHz. The average photocurrent is 20 mA. We show the experimental results in Fig. 4.4. We can separate the IMD2 (second-order IMD powers) into two groups. One group contains the sum frequencies powers at $F_1 + F_2$, $F_1 + F_3$, and $F_2 + F_3$, and the other group contains the difference frequencies powers at $|F_1 - F_2|$, $|F_1 - F_3|$, and $|F_2 - F_3|$. In each group, the IMD2 behavior is the same. Hence, we only show the IMD2 powers at $F_1 + F_2$ and $|F_1 - F2|$. However, we observe a significant difference between the IMD2 powers for the sum frequency $(F_1 + F_2)$ and the difference frequency $(|F_1 - F_2|)$. A bias null appears in both IMD2 powers, but the bias voltage at which a null appears is different.

4.2   Simulation results

We use a drift-diffusion model to study the IMD in this MUTC device [88] with a three-tone setup, which is the same as in the experiments. The generation

InGaAs, p+, Zn, 2.0×10^{19}, 50nm		50 nm
InP, p+, Zn, 1.5×10^{18}, 100nm		150 nm
InGaAsP, Q1.1, Zn, 1.0×10^{16}, 15nm		165 nm
InGaAsP, Q1.4, Zn, 1.0×10^{16}, 15nm		180 nm
InGaAs, p, Zn, 2.0×10^{18}, 100nm		280 nm
InGaAs, p, Zn, 1.2×10^{18}, 150nm		430 nm
InGaAs, p, Zn, 8.0×10^{17}, 200nm		630 nm
InGaAs, p, Zn, 5.0×10^{17}, 250nm		880 nm
InGaAs, Si, 1.0×10^{16}, 150nm		1030 nm
InGaAsP, Q1.4, Si, 1.0×10^{16}, 15nm		1045 nm
InGaAsP, Q1.1, Si, 1.0×10^{16}, 15nm		1060 nm
InP, Si, 1.4×10^{17}, 50nm	$\rightarrow$ cliff layer	1110 nm
InP, Si, 1.0×10^{16}, 900nm	$\rightarrow$ collection layer	2010 nm
InP, n+, Si, 1.0×10^{18}, 100nm		2110 nm
InP, n+, Si, 1.0×10^{19}, 900nm		3010 nm
InGaAs, n+, Si, 1.0×10^{19}, 20nm		3030 nm
InP, n+, Si, 1.0×10^{19}, 200nm		3230 nm
InP, semi-insulating substrate Double side polished		

Figure 4.2: Structure of the MUTC photodetector. Green indicates the absorption regions, which include an intrinsic region and a p-doped region. Red indicates highly doped InP layers, purple indicates highly-doped InGaAs layers, and white indicates other layers.
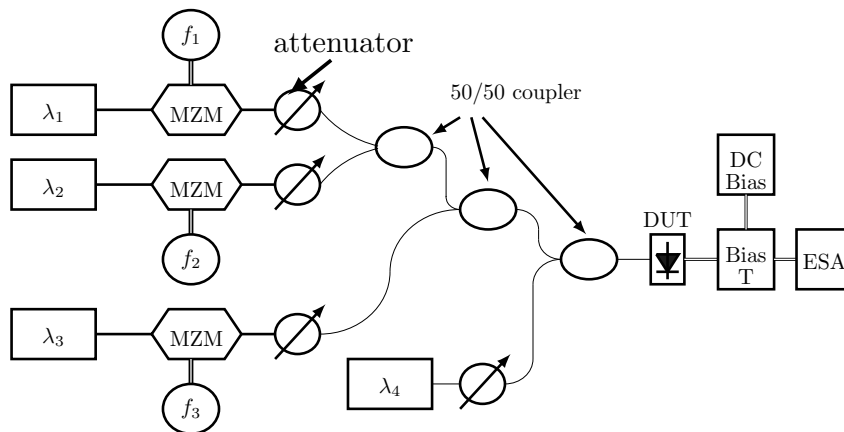
Figure 4.3: Schematic illustration of the test setup. MZM = Mach-Zehnder modulator, DUT = Device under test, ESA = Electronic spectrum analyzer

82

Figure 4.4: The measured fundamental, IMD2, and IMD3 powers as a function of reverse bias for input frequencies $F_1 = 4.9$ GHz, $F_2 = 5.0$ GHz, and $F_3 = 5.15$ GHz with a photocurrent of 20 mA.

rate may be expressed as

$$G = G_0 \left\{ 1 + m_d \left[\sin(2\pi F_1 t) + \sin(2\pi F_2 t) + \sin(2\pi F_3 t) \right] \right\}, \tag{4.1}$$

where G_0 is the steady state generation rate, m_d is the modulation depth, and F_1, F_2, and F_3 are the three-tone modulation frequencies.

Figure 4.5 shows the steady-state electron and hole currents in the device. We see that in the n-region, the total current depends on electron current, and in the p-region, the hole current is larger than the electron current. In the intrinsic region, the electron current is larger than the hole current. We know that the response time of the MUTC device depends mainly on the electron transit time. It is important to analyze the electron current in the intrinsic region, where most of the electrons are generated.
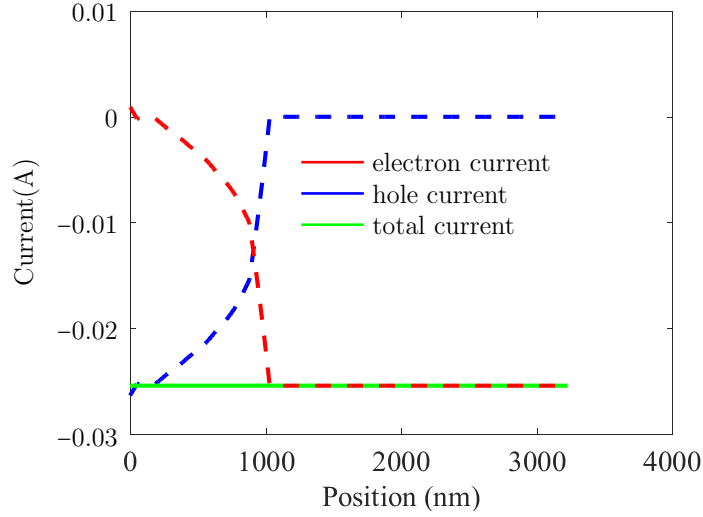
Figure 4.5: The calculated electron and hole currents in the device.

We show the simulation results for the IMD2 power in Fig. 4.6, and the agreement with the experiments is good. We also obtain a bias null in the IMD2 power. The bias null in the difference frequency IMD2 power appears at around 6 V, while the bias null in the sum frequency IMD2 power appears at around 6.5 V, which agrees with the experiment.

Figure 4.7 shows the RF output power when the Franz-Keldysh effect is not included, in which case there is no bias null in the IMD2 power. We conclude that the nulls are due to the Franz-Keldysh effect. The absorption coefficient changes when the electric field changes in the device, so that the generation rate in the device — especially in the intrinsic absorption region — changes as a function of the electric field. The nulls appear at biases where the change of absorption coefficient as a function of the electric field strength is small. Figure 4.8 shows the electric field strength at 2 and 6 V. The electric field only differs significantly from zero in the
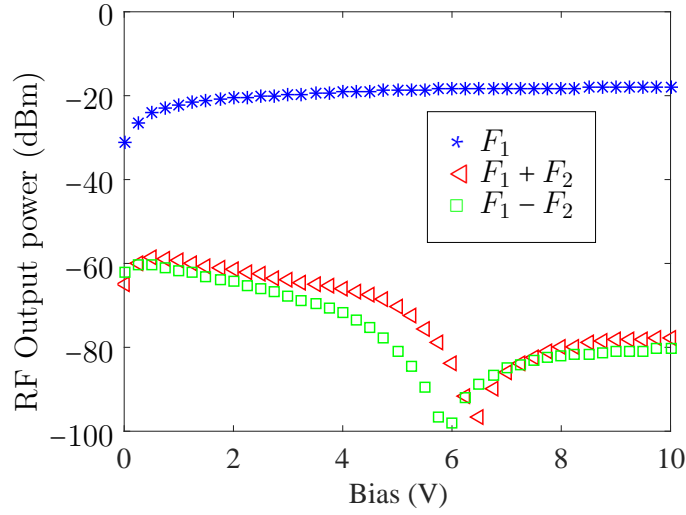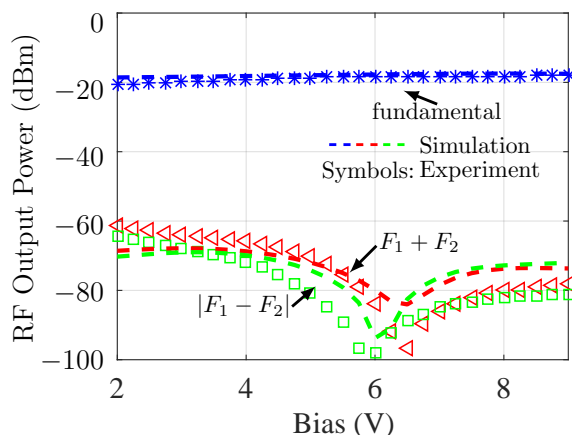
Figure 4.6: The measured and calculated fundamental and IMD2 powers as a function of reverse bias for input frequencies $F_1 = 4.9$ GHz, $F_2 = 5.0$ GHz, and $F_3 = 5.15$ GHz.

intrinsic absorption region, which is due to the cliff layer. The Franz-Keldysh effect changes the absorption in the intrinsic absorption region since the electric field is large. Figure 4.9 shows the absorption coefficient as a function of the electric field strength. When the electric field is around 150 kV/cm, which correspond to an applied bias of 6 V, the absorption reaches its peak. However, at this electric field, the change of absorption due to the change of the electric field is small, so that the nonlinearity due to the Franz-Keldysh effect is minimized. Hence, the IMD2 power reaches its lowest value at around 6 V.

Figure 4.10 shows the current output in the presence of a three-tone modulation and a one-tone modulation. With a three-tone modulation, it is difficult to determine the physical origin of the device nonlinearity and explain the origin and location of the bias null because two or three frequencies are mixed together. We will use the one-tone modulation to analyze the physical origin of the nonlinearity.
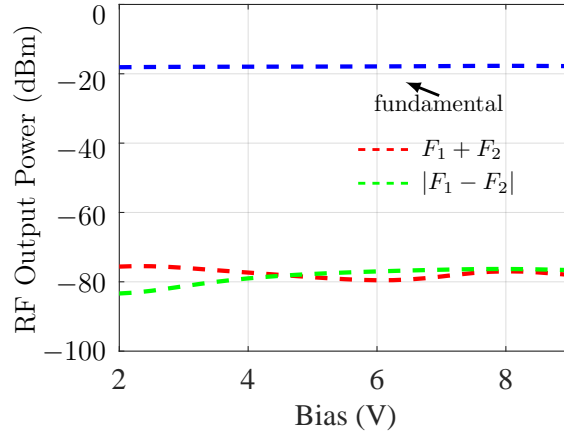
Figure 4.7: The calculated fundamental and IMD2 powers as a function of reverse bias for input frequencies $F_1 = 4.9$ GHz, $F_2 = 5.0$ GHz, and $F_3 = 5.15$ GHz. The Franz-Keldysh effect is not included in the simulation.
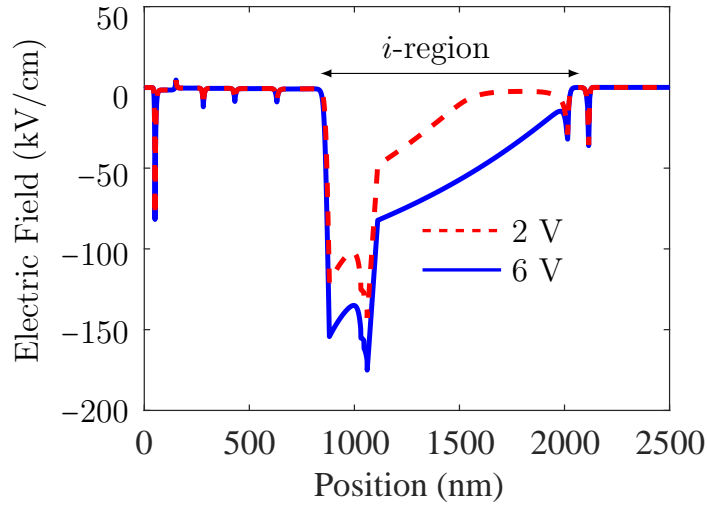
Figure 4.8: The calculated electric field in the device at 2 and 6 V.
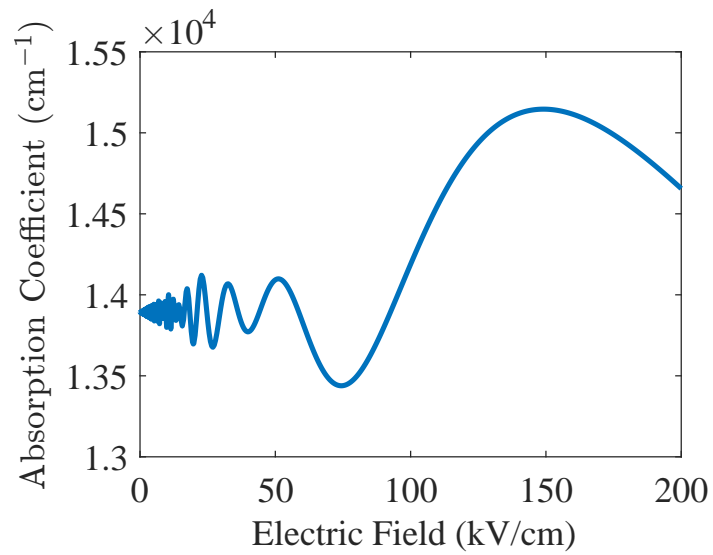
Figure 4.9: The calculated absorption coefficient as a function of the electric field strength.
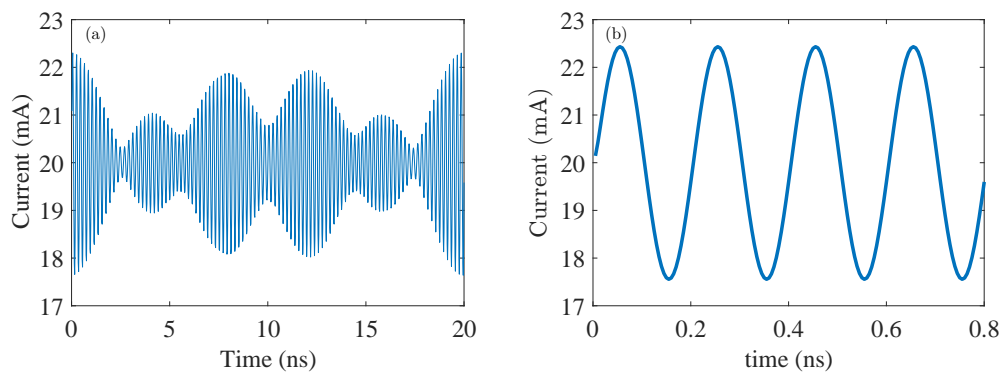
Figure 4.10: The current output of the photodetector with (a) a three-tone and (b) a one-tone modulation.
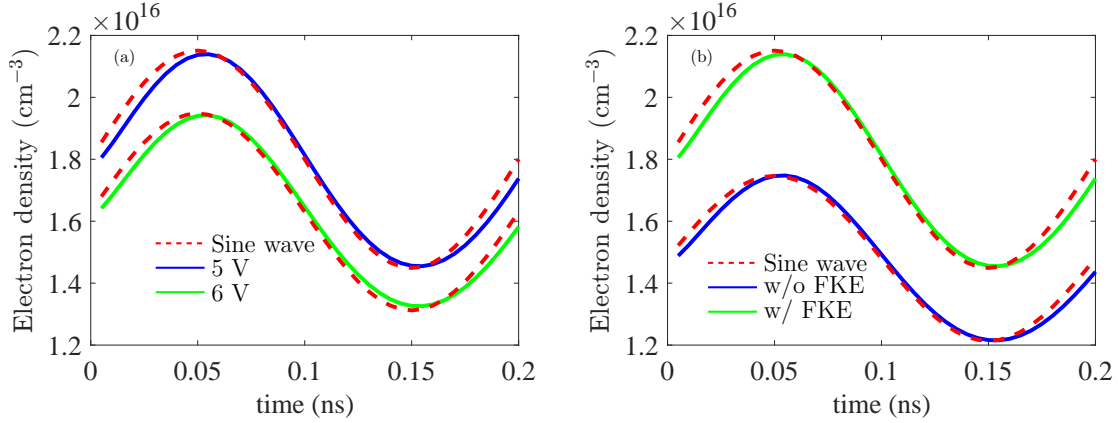
Figure 4.11: (a) The calculated electron density in the intrinsic region at 1000 nm compared to a sine function at 5 and 6 V. (b) The calculated electron density in the intrinsic region at 1000 nm compared to a sine function with and without the Franz-Keldysh effect (FKE).

We will show that the results with a three-tone modulation and a simulation that keeps only one tone are almost the same. Figure 4.11 shows the electron density as a function of time compared to a modulation sine function (one-tone modulation) in the intrinsic region. The amplitude of the modulation sine function is adjusted to have the same amplitude as the electron density, but the phase is unchanged. We observe that the electron density is not exactly a sine function. It is a delayed with respect to the modulation sine function. We also find that the modulation depth for the electron density (about 0.19) is larger than the modulation depth (0.04) of the optical input power, which creates electrons in the intrinsic region. This increase in the modulation depth occurs because electrons accumulate in the intrinsic region at the heterojunction boundary with the cliff layer. In Fig. 4.11(a), we show that the difference of the electron density from a sine function at 5 V is larger than the difference of the electron density from a sine function at 6 V, which occurs because
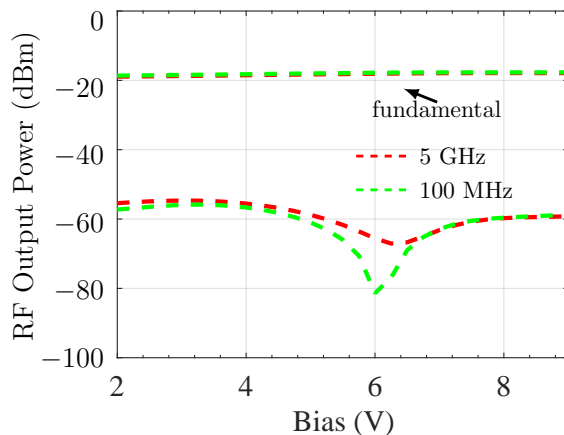
Figure 4.12: The calculated RF output powers for modulation frequencies of 100 MHz and 5 GHz.

the Franz-Keldysh effect is mitigated when the bias is 6 V, as we previously discussed. Figure 4.11(b) shows the electron density as a function of time with and without the Franz-Keldysh effect at 5 V. We observe that the difference between the electron density and the sine function is larger when the Franz-Keldysh effect is taken into account, providing further evidence that the Franz-Keldysh effect is the principal source of nonlinearity in the device.

We have shown that the Franz-Keldysh effect is the reason for the null that appears in the IMD2 power, but we have not explained why the null position is different for the sum frequency and the difference frequency IMD2 powers. We use a one-tone simulation with different modulation frequencies to examine this question. The modulation frequencies are set to 100 MHz and 5 GHz, so that the second-harmonic frequencies are 200 MHz and 10 GHz, which correspond to the difference and sum frequencies in the three-tone measurement. We show the harmonic powers in Fig. 4.12. We find that the bias null in the second-harmonic power at a modulation
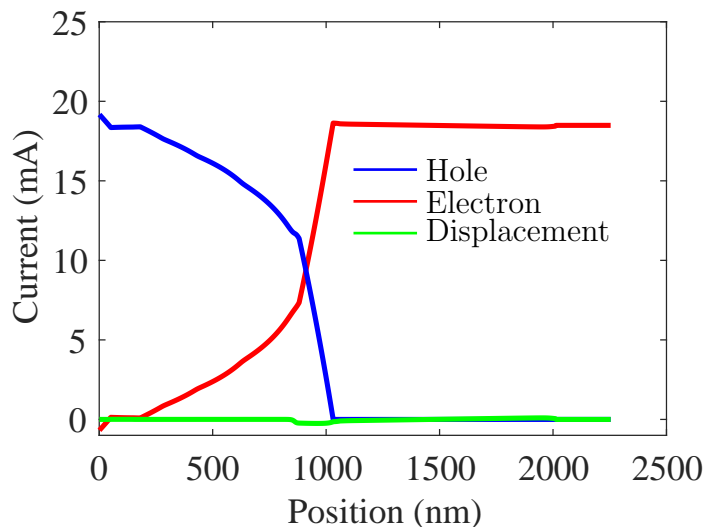
Figure 4.13: The calculated amplitude of the electron, hole, and displacement current in the device when a modulation is applied at 5 GHz.

frequency of 100 MHz is the same as the bias null in the three-tone simulation at frequency $|F_1 - F_2|$, and the bias null in the second-harmonic power at a modulation frequency of 5 GHz is the same as the bias null in the three-tone simulation at the frequency $F_1 + F_2$. This frequency dependence of the null position is consistent with experiments [90].

4.3   Discussion

The current in the intrinsic region includes the electron current, the hole current, and the displacement current. We show these currents in Fig. 4.13 at 5 GHz. We see that the displacement current is almost zero at all positions except in the intrinsic region. Although the displacement current is small compared to the electron and hole currents in the intrinsic region, the displacement current contributes to the harmonic powers. In Fig. 4.14(a), we show the RF output current in the intrinsic

region without the displacement current. We find that the bias nulls are the same for different modulation frequencies. Displacement current is responsible for the difference in the bias null of the IMD2 powers for the sum and difference frequencies. The displacement current is proportional to the rate of change of the electric field in the intrinsic region. When the modulation frequency is large, the rate of change increases, and the displacement current becomes large and has a large effect on the harmonic powers. Figure 4.14(b) shows the IMD2 power of the displacement current. At the sum frequency $F_1 + F_2$, the IMD2 power of the displacement current is around -85 dBm, which is close to the IMD2 power of the total current. By contrast, the IMD2 power of the displacement current at the difference frequency $|F_1 - F_2|$ is about -125 dBm, which is much smaller than the IMD2 power of the total current. So, the displacement current does not affect the IMD2 power of the difference frequency.

From a circuit perspective, the displacement current is due to device capacitance. Charge of opposite sign accumulates on each side of the intrinsic region, and there is almost no charge in the intrinsic region, creating a capacitor. We show the charge in the p-region and intrinsic region in Fig. 4.15. We see that when the bias increases, the charge in the p-region increases. We note that the charge in the p-region is negative and is positive in the n-region. Figure 4.16 shows the capacitance of the device as a function of bias. The capacitance in the photodetector is almost constant when the bias is large, but the impedance of the capacitance is different for different modulation frequencies. The impedance difference for different modulation frequencies leads to different displacement currents, which affects the bias null in

Figure 4.14: The calculated fundamental and IMD2 powers as a function of reverse bias for input frequencies F_1 = 4.9 GHz, F_2 = 5.0 GHz, and F_3 = 5.15 GHz. (a) Displacement current is not included in the total current. (b) IMD2 power of the displacement current.
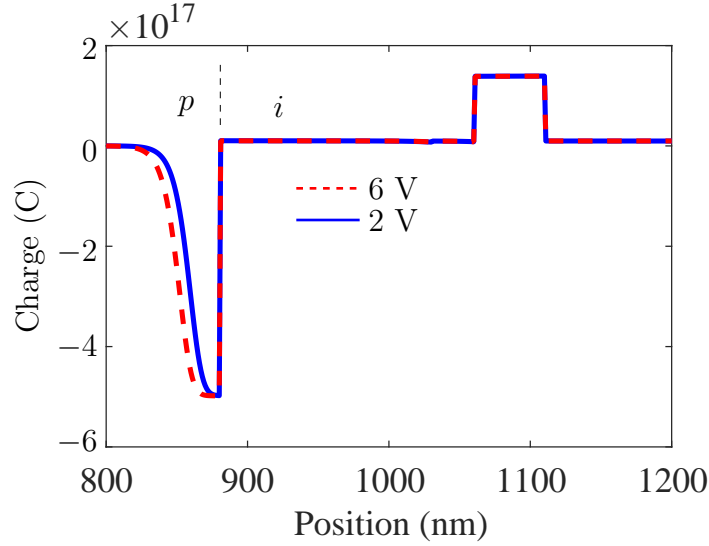
Figure 4.15: The calculated charge in the p-region and intrinsic region in the device at 2 and 6 V.

the IMD2. Figure 4.17 shows the largest displacement current when modulation is applied to the device for modulation frequencies of 200 MHz and 5 GHz. We observe that the displacement current with a 5 GHz modulation is much larger than with a 200 MHz modulation. The displacement current is larger in the intrinsic absorption region, where the electric field is larger than it is in other regions.

Figure 4.18 shows the three-tone RF output powers as a function of applied bias, when the lifetime increases to 5×10^{-11} in the p-region. The null position in the second order harmonic powers are almost the same for the sum frequency and the difference frequency. The recombination rate in the p-region significantly affects the bias null of the IMD2. When the recombination time increases, the recombination rate decreases in the p-region, so that more electrons enter the intrinsic region, increasing the electron density and decreasing the electric field in the intrinsic region. The Franz-Keldysh effect causes the null to appear when the electric field is around
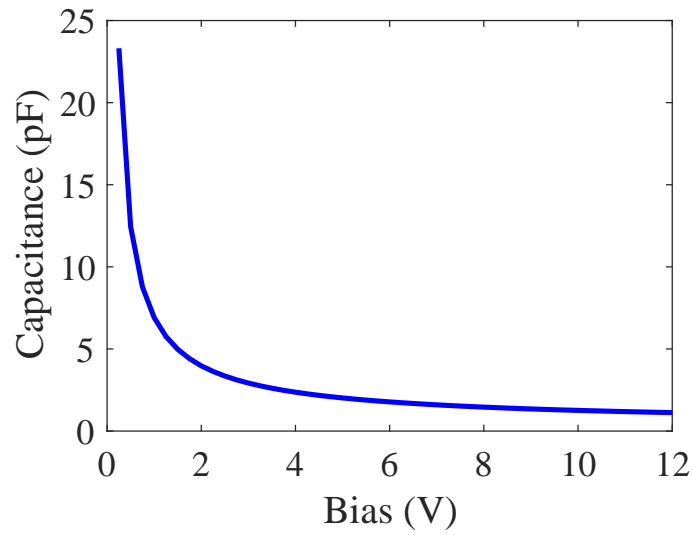
Figure 4.16: The calculated capacitance in the device as a function of bias.
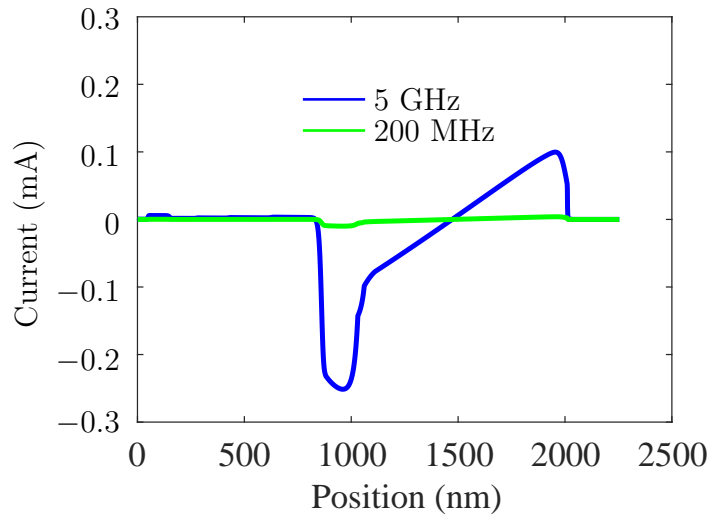
Figure 4.17: The amplitude of the sinusoidally varying displacement current in the device at 200 MHz and 5 GHz.
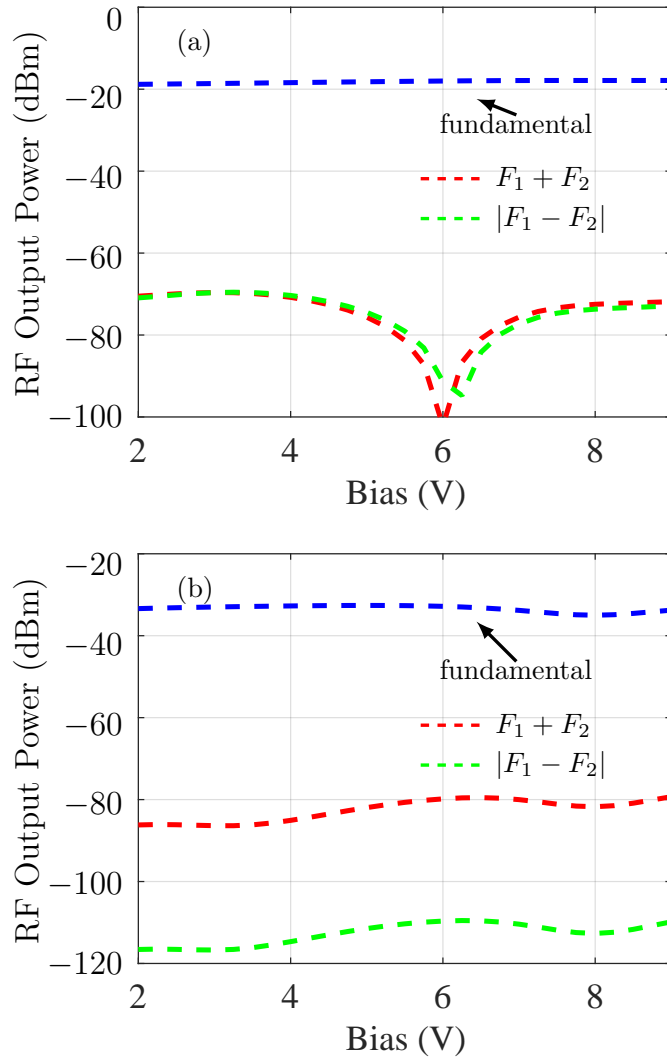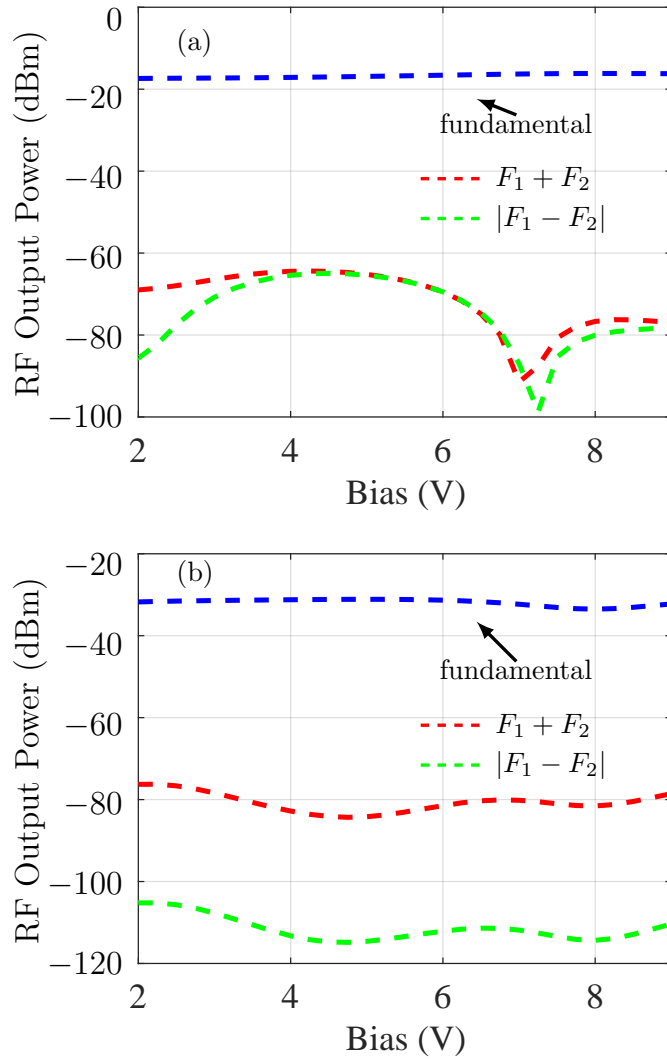
Figure 4.18: The calculated fundamental and IMD2 powers as a function of reverse bias for input frequencies $F_1 = 4.9$ GHz, $F_2 = 5.0$ GHz, and $F_3 = 5.15$ GHz. The lifetime in the p-region is 5×10^{-11} s. (a) IMD2 power of the total current and (b) IMD2 power of the displacement current

150 kV/cm. So, when the electric field decreases due to the increase in the electron lifetime in the p-region, the bias null moves to a larger voltage bias where the average electric field in the intrinsic absorption region is around 150 kV/cm.

Additionally, the electron diffusion coefficient is a factor in determining the position of the nulls. When the diffusion coefficient of the electrons in the p-region increases, more electrons diffuse into the p-region. Hence, there are less electrons in the intrinsic region, so that the electric field n the intrinsic region increases, and the capacitance increases. As a consequence, the impedances is smaller at high modulation frequencies.

4.4   Summary

We obtained agreement with experiments for the null position in the IMD2 power for different modulation frequencies. We investigated the physical origin of the nulls in the IMD2 power, and we found that the Franz-Keldysh effect causes the bias nulls. The difference in the location of the bias nulls between the sum frequency and difference frequency IMD2 powers is due to the displacement current in the intrinsic region. When the frequency is high, the displacement current is large and affects the harmonic powers.

We also found that the recombination rate in the p-region affects the bias null in the IMD2 power. When the recombination rate decreases, more electrons enter into the intrinsic region, which decreases the electric field is this region. Then the bias null appears at a higher bias. The diffusion coefficient in the p-region is also a

factor in determining the location of the bias null.

Chapter 5

Modeling amplitude to phase (AM-to-PM) noise conversion in an MUTC photodetector

5.1   Introduction

Ultrastable microwave signals are of great interest in applications such as radar, telecommunications, navigation systems, and time synchronization [94–96]. Recently, there has been great interest in generating microwaves through optical frequency division (OFD) with a modelocked laser comb. Ultrastable microwave generation has been demonstrated [18, 19, 97, 98]. The stability of the optical reference is transferred to the repetition rate of the pulse train of a modelocked laser. Two factors determine the noise level of the microwave output. One factor is the phase noise in the modelocked laser comb, and the other factor is the phase noise that is generated in the photodetector. In this paper, we will focus on the second factor, explaining in particular the amplitude-to-phase noise conversion in a high current photodetector.

The phase noise that is produced by the photodetector is a critical limit to system performance. A major source of phase noise is amplitude-to-phase (AM-to-PM) conversion in the photodetector. The AM-to-PM conversion coefficient $\alpha_{\mathrm{AM/PM}}$ is defined as the phase change in the device $\Delta\phi$, divided by the fractional optical

power fluctuation $\Delta P/P$.

$$\alpha_{\text{AM/PM}} = \frac{\Delta\phi}{\Delta P/P}. \tag{5.1}$$

Zhang et al. [99] used a simple model to study the AM-to-PM conversion coefficient in a p-i-n photodetector. Taylor et al. [100] experimentally studied AM-to-PM conversion and found that there are several nulls, where the AM-to-PM conversion coefficient approaches zero as a function of the photocurrent. In the experiments, they use the impulse response method to measure the phase change and the AM-to-PM noise conversion coefficient.

We have used a modified drift-diffusion model to study the AM-to-PM conversion in the modified uni-traveling carrier (MUTC) photodetector [88] using the configuration shown in Fig. 4.2. We first calculate the impulse response in the time domain, and from that we calculate the AM-to-PM conversion coefficient. We explain the physical origin of the conversion nulls, and we show how the pulse duration affects the AM-to-PM noise conversion coefficient. We show that when the pulse duration is shorter than 500 fs, the output is only affected by the total pulse energy.

There are several methods to measure the phase noise [100]. One is to use a phase bridge, which directly measures the phase fluctuations. The other method is to measure the time-domain impulse response of the photodetector and to use a Fourier transform to calculate the phase difference as the power varies. The advantage of using a phase bridge is high precision, but the experimental setup is more complicated than measurement of the time domain impulse response. Measurement of the time domain impulse response, followed by the Fourier transform, is easier to

do, but it is necessary to measure more average current points.

We will simulate the impulse response of the photodetector to calculate the phase. In the model, the input light is a pulse train. We calculate the output current as a function of time. Then, we use a Fourier transform to calculate the RF phase for the given Fourier frequency. We use the phase information to calculate the AM-to-PM conversion coefficient that is defined in Eq. 5.1.
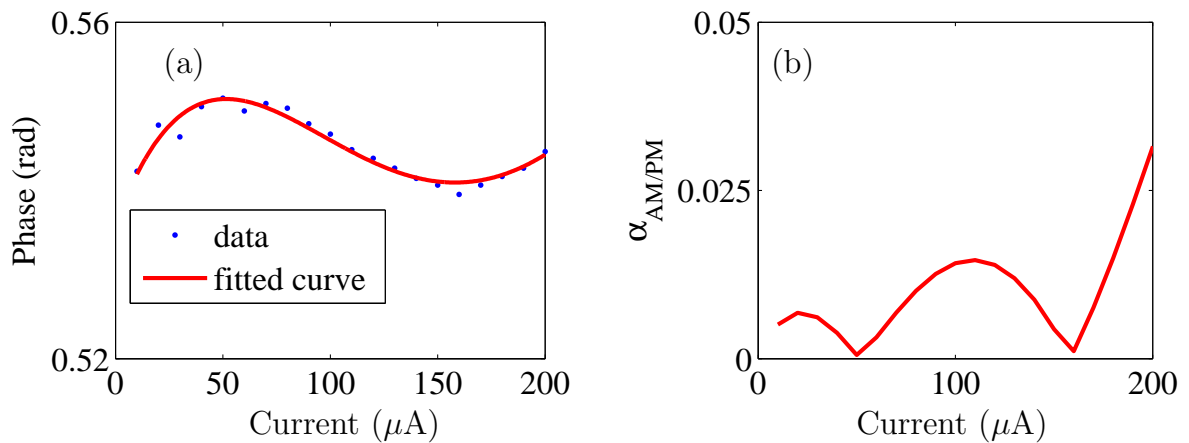
Figure 5.1: The measured phase change and AM-to-PM noise conversion coefficient in the MUTC device as a function of the output average photocurrent at 1 GHz.

Figure 5.1 shows the experimental phase change and AM-to-PM noise conversion coefficient. The diameter of the device is 40 μm. The red curves are the fitted curves. The repetition rate is 250 MHz. We calculate the phase change and the AM-to-PM noise conversion coefficient at 1 GHz. We observe two nulls in the AM-to-PM noise conversion coefficient. The phase increases when the photocurrent increases to 50 μA, and next decreases when the photocurrent increases to 155 μA, and finally increases again when the photocurrent further increases. The pulse profile that we

use in our calculations is

$$y(t) = A\mathrm{sech}\left(\frac{t - t_p}{t_w}\right), \tag{5.2}$$

where t_p is the pulse position, t_w is the pulse duration, and A is the pulse amplitude.

5.2 Simulation results
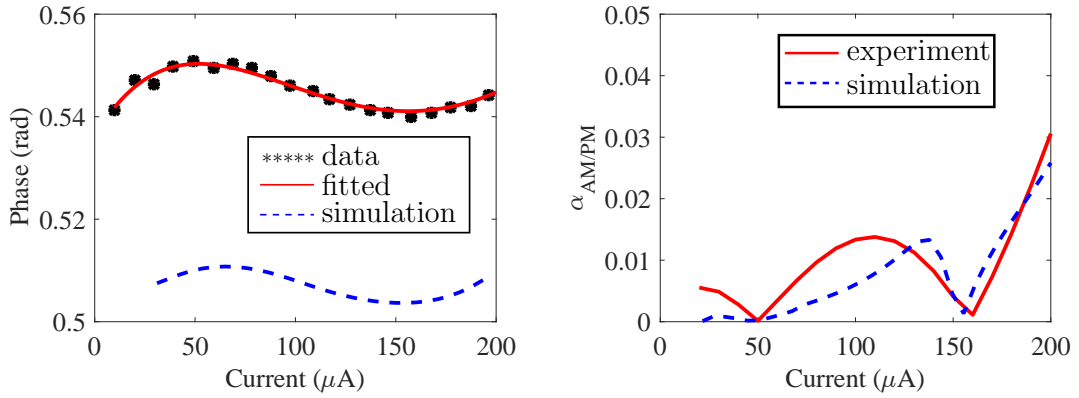
Figure 5.2: The calculated (a) phase change and (b) AM-to-PM noise conversion coefficient in the MUTC device as a function of output average photocurrent at 1 GHz. The repetition rate is 250 MHz.
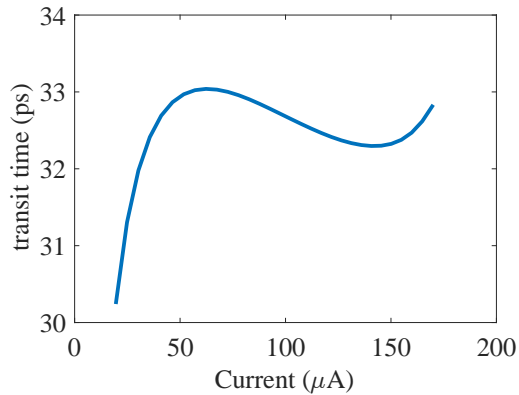
Figure 5.3: The calculated transit time in the MUTC device as a function of the average output photocurrent.

Figure 5.2 shows the calculated phase change and the AM-to-PM noise con-
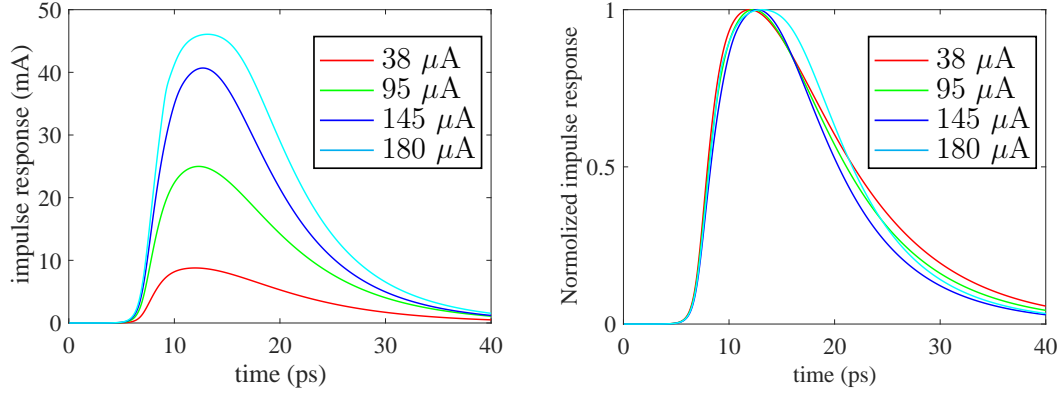
Figure 5.4: The calculated impulse response in the MUTC device for different average output photocurrents.
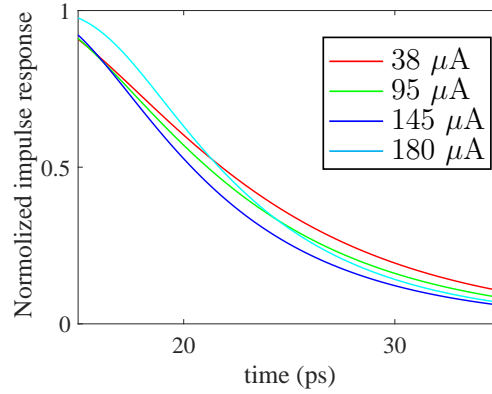
Figure 5.5: The calculated impulse response in the MUTC device for different average output photocurrents.

version coefficient. We obtain agreement with experiments for the phase change and AM-to-PM noise conversion coefficient. The nulls appear due to the phase changes when the photocurrent increases. The offset in the phase between the simulation and the experimental data is due to the different input pulse phase and is not meaningful. It is the relative phase change as a function of the average pulse current that is physically important. At present, we do not have an explanation for the difference between the measured and theoretical values for $\alpha_{\mathrm{AM/PM}}$, but this difference does

not affect our conclusions. Figure 5.3 shows the calculated average transit time in the device. The behavior of the transit time is similar to the phase change. When the phase change increases, the transit time increases. At 50 μA, the transit time is a maximum. Figure 5.4(a) shows the impulse response for different average output photocurrents. Figure 5.4(b) shows the normalized impulse response. Figure 5.5 shows the tail of the normalized impulse response. When the average current increases, the time for the impulse response to reach its peak increases. However, when the current increases from 30 μA to 150 μA, the tail of the impulse response decreases. These two processes compete with each other, leading at first to a small phase increase and then a phase decrease. When the current is larger than 150 μA, the output photocurrent response time increases dramatically, which corresponds to a phase increase.

5.3 Physical origin of the nulls

The AM-to-PM noise conversion coefficient α, defined by Eq. (5.2), depends on the phase change $\Delta\phi$. The phase change in turn depends on the average electron transit time in the device. A key feature of an MUTC device is that the hole transit time is dominated by diffusion current and is fast compared to the electron transit time.

Figure 5.6 shows the electron velocity as a function of electric field for InGaAs and InP. The velocity first rapidly increases and then decreases as a function of the electric field, eventually saturating. The principal physical reason for this behavior
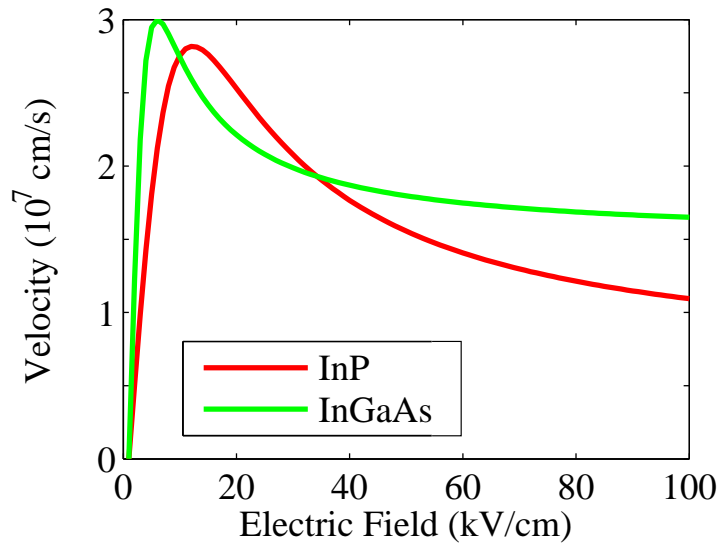
Figure 5.6: The calculated electron velocity as a function of electric field for InGaAs and InP.
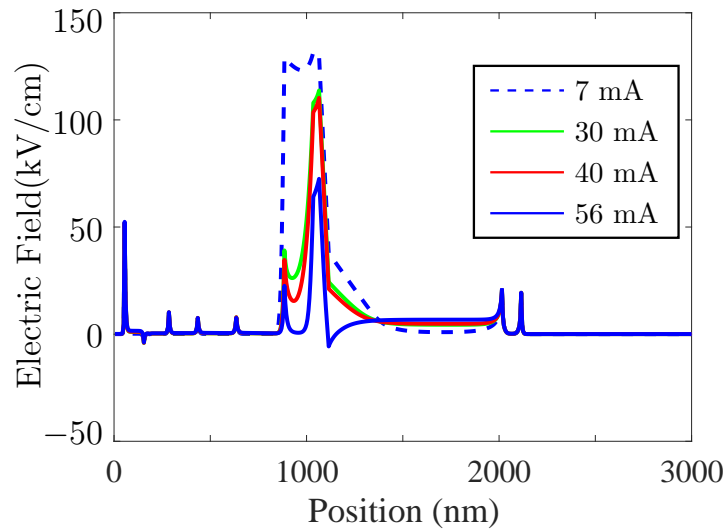
Figure 5.7: The calculated steady-state electric field distribution in the device for different photocurrents. The applied reverse bias is 3 V.

is that the ratio of heavy (X- and L-valley) electrons to light (Γ-valley) electrons increases as the electric field increases, slowing the average velocity. This behavior is important in understanding the appearance of the higher-current null in the AM-
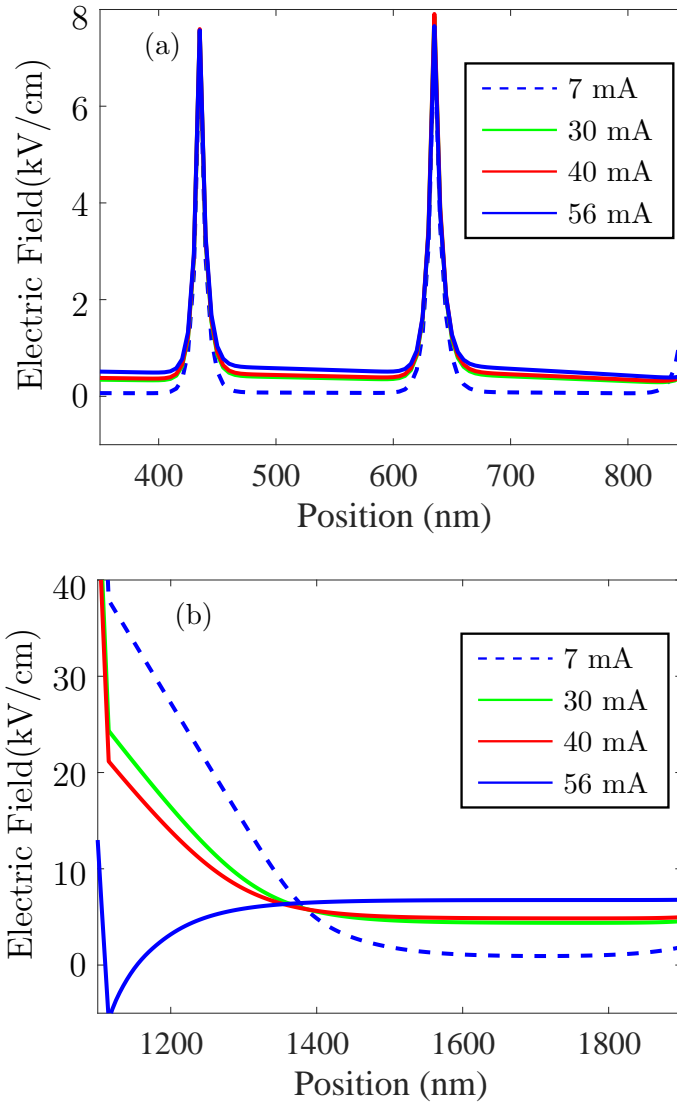
Figure 5.8: The calculated steady state electric field distribution in the device for different photocurrents in (a) the p-absorption region and (b) the collection region shown in Fig. 4.2. The applied reverse bias is 3 V.

to-PM conversion.

There is an intrinsic absorption region and a p-absorption region in the device. The photogenerated electrons in the InGaAs intrinsic region travel faster than in the InP intrinsic region. However, there is a heterojunction between InGaAs and InP. When the pulse energy increases, more electrons accumulate in the heterojunction,

leading to a field that opposes the current flow. So, a larger optical pulse energy leads to a longer time for the photocurrent to reach its peak.

The output photocurrent decay time changes significantly when the optical pulse energy changes because the peak photocurrent changes, leading to a change in the electric field in the device. The velocity depends on the electric field and changes as the peak current varies. When the average photocurrent is 50 μA and 150 μA, the corresponding peak currents are 10 mA and 40 mA. Figure 5.7 shows the electric field in the device for different photocurrents. Figure 5.8(a) shows the electric field in the p-absorption region and the collection region. We observe that when the current increases in the device, the electric field in the p-absorption region and in the collection region increases. Figure 5.6 shows the electron velocity as a function of the electric field in InGaAs and InP. The electron velocity increases in the p-absorption region. The decay times decrease as the output photocurrent increases. The two processes compete with each other. When the output average photocurrent is less than 50 μA, the time that it takes the photocurrent to reach its peak dominates the total transit time. So, the phase increases as the current increases up to 50 μA. When the output photocurrent is between 50 μA and 150 μA, the decay time dominates the average transit time. Hence, the phase increases when the photocurrent increases. Finally, when the output photocurrent is larger than 150 μA, which corresponds to a peak current of 40 mA, the electric field in the n-region becomes positive, so that the electron transit time increases when the output photocurrent increases. Hence, the phase again increases when the photocurrent increases.

106
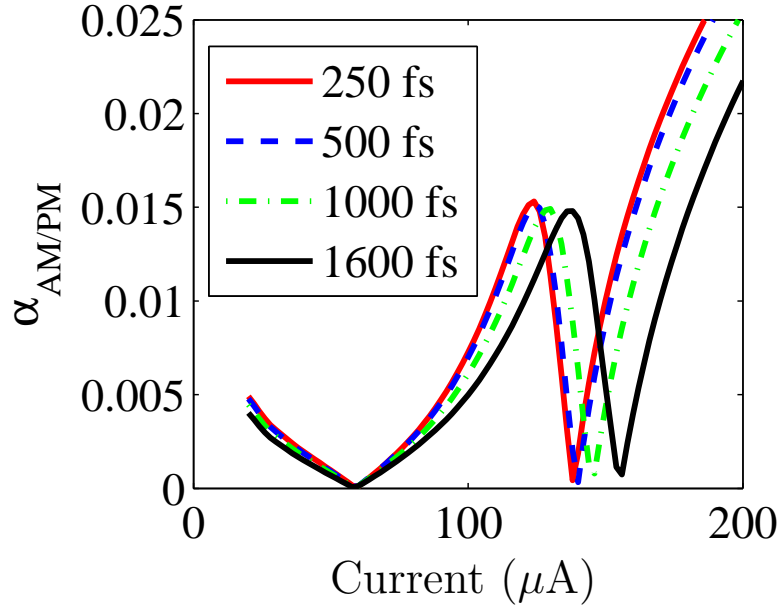
Figure 5.9: The calculated AM-to-PM noise conversion with different pulse durations at 1 GHz.

5.3.1 Pulse duration

Figure 5.9 shows the AM-to-PM noise conversion coefficient for different pulse durations. We observe that the null position does not change when the pulse duration is less than 500 fs. When the pulse duration is larger than 500 fs the second null position shifts to larger photocurrents. This shift occurs even though the pulse duration is short compared to the photodetector response time, which is 40 ps. When the pulse duration increases, the peak current decreases. Figure 5.10 shows the impulse response for different pulse durations with the same pulse energy. The photocurrent at which the second null occurs depends on the electric field, which is determined by the peak current. When the pulse duration increases, the peak current decreases, and a second null appears at a larger average photocurrent.
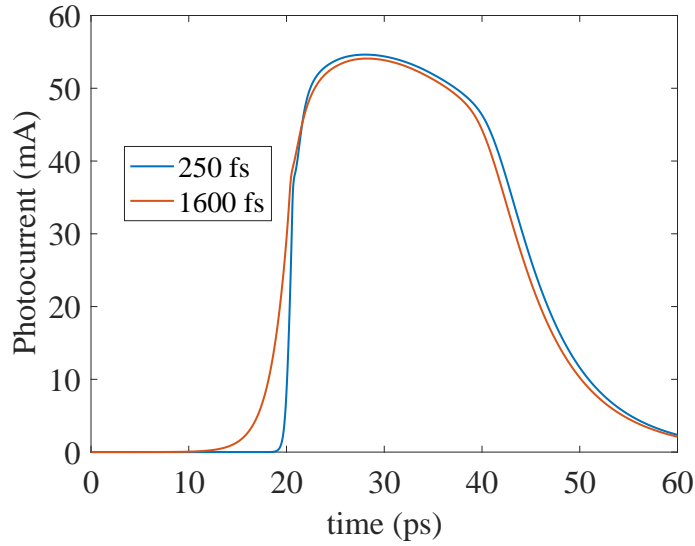
Figure 5.10: The calculated impulse response for different pulse durations and the same pulse energy.

5.3.2 Repetition rate

Figure 5.11(a) shows the AM-to-PM noise conversion coefficient as a function of average current for different repetition rates. The curves are the same except for a scale factor, as shown in Fig. 5.11(b), where we plot the two curves as a function of optical pulse energy. So, the AM-to-PM noise conversion coefficient does not depend on the repetition rate when the repetition rate is less than the bandwidth of the photodetector, which is about 25 GHz. The average photocurrent depends on the repetition rate. This result is consistent with experiments [97].

Figure 5.12 shows the impulse response for different repetition rates. We observe that the shape of the output photocurrents are the same. The only difference is that the output photocurrent pulses are spaced twice as far apart, lowering the average photocurrent by a factor of two, which has no effect on the Fourier transform
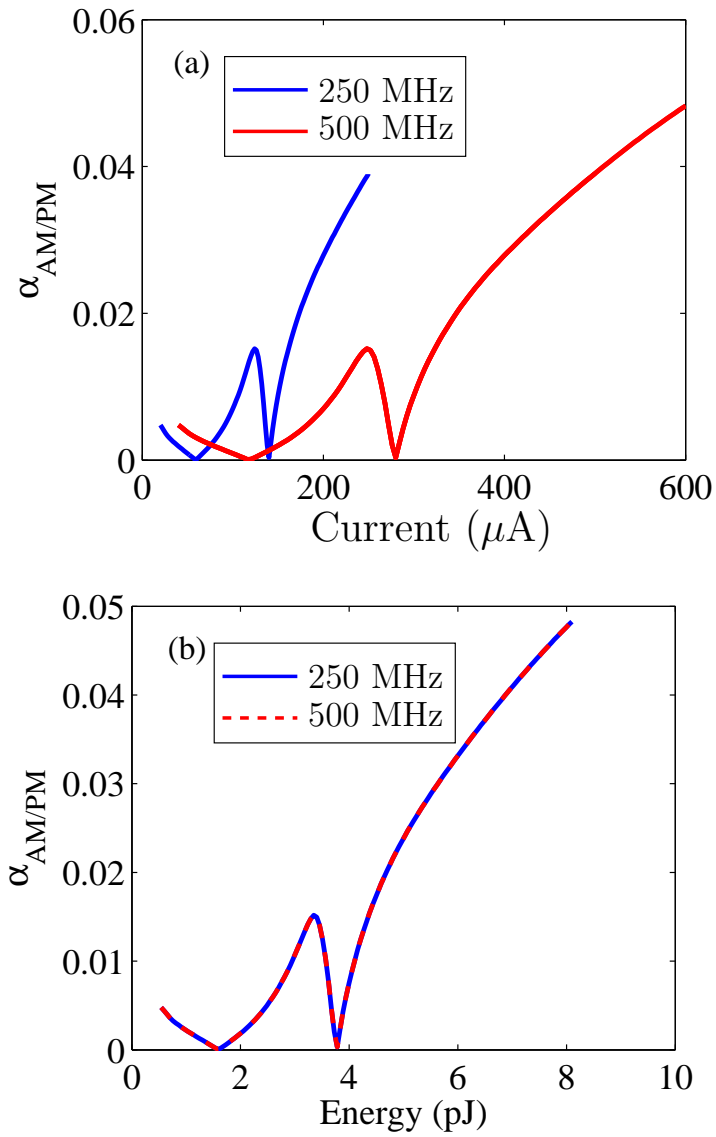
Figure 5.11: The calculated AM-to-PM noise conversion coefficient at 1 GHz in the MUTC for different repetition rates. (a) The AM-to-PM noise conversion coefficient as a function of average current. (b) The AM-to-PM noise conversion coefficient as a function of pulse energy.

of the photocurrent impulse response.
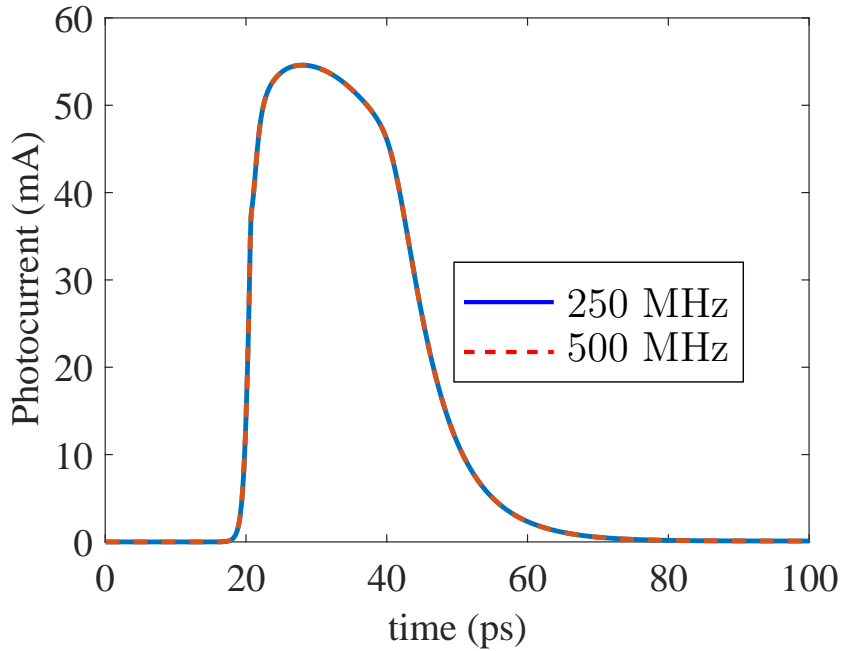
Figure 5.12: The calculated impulse response of the MUTC device for different repetition rates.

5.4 Discussion

5.4.1 Suggestions for improvement

The AM-to-PM noise conversion coefficient depends on the phase change in the device, which is due to the change in the average electron transit time. The pileup of electrons that occurs at the heterojunction between the intrinsic absorption layer and the cliff layer is a major factor increasing the transit time. It is not possible in practice to completely eliminate the heterojunction. However, by having several intermediate layers, it should be possible to improve the heterojunction transition. Figure 5.13 shows the phase change and AM-to-PM conversion coefficient if the heterojunction barrier is reduced by half. The $\alpha_{AM/PM}$ noise conversion coefficient

is then also reduced by half. Figure 5.14 shows the phase change and AM-to-PM conversion coefficient if there is no heterojunction between InGaAs and InP. In this case, the $\alpha_{AM/PM}$ noise conversion coefficient is reduced by about one order of magnitude. We conclude that AM-to-PM noise conversion coefficient is reduced when the heterojunction barrier is reduced.
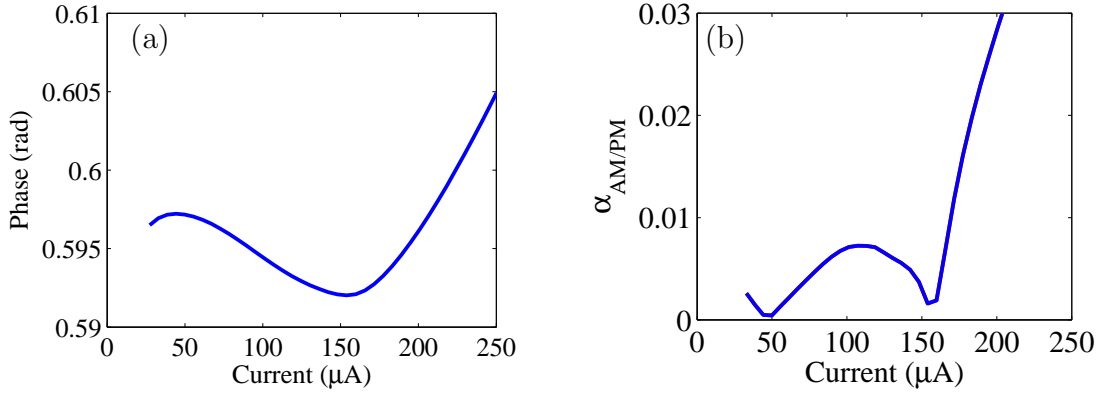
Figure 5.13: The calculated (a) phase change and (b) AM-to-PM noise conversion coefficient in the MUTC device as a function of output average photocurrent at 1 GHz. The heterojunction barrier is reduce by half.
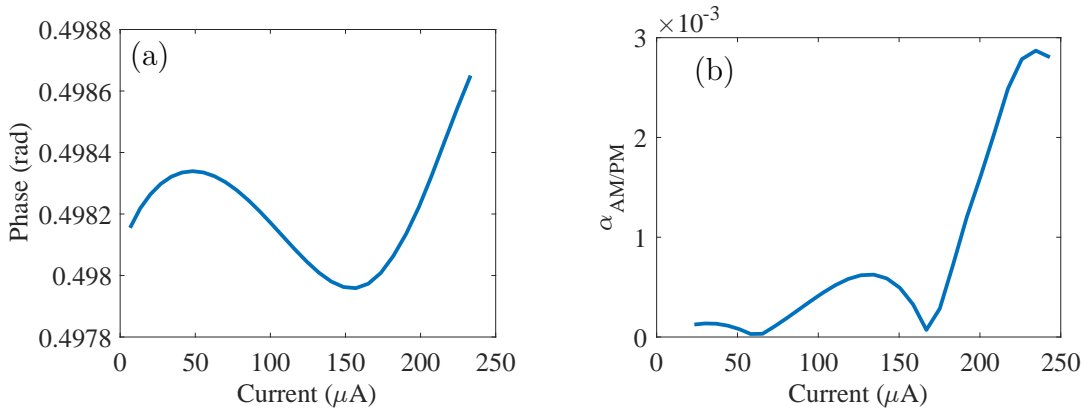
Figure 5.14: The calculated (a) phase change and (b) AM-to-PM noise conversion coefficient in the MUTC device as a function of output average photocurrent at 1 GHz. A heterojunction barrier is not included in the model.

5.5   Summary

We used a drift-diffusion model to study the AM-to-PM noise conversion in an MUTC photodetector. There are two nulls in the AM-to-PM noise conversion coefficient as a function of the average photocurrent. We have explained the appearance of these nulls as a consequence of changes in the transit time through the device, which is in turn due to the nonlinear dependence of the electron velocity on the electric field.

We also showed that when the pulse duration is less than 500 fs, the AM-to-PM conversion coefficient does not change. When the pulse duration is greater than 500 fs, the second null in the AM-to-PM shifts to larger photocurrents. The repetition rate does not change the AM-to-PM conversion coefficient when plotted as a function of the input optical pulse energy.

The AM-to-PM noise conversion coefficient can be greatly reduced by having an intermediate transition layer between the InGaAs and InP heterojunction.

Chapter 6

Carrier flow in the photodetectors

In this section, we describe and compare the carrier flow in the different photodetector devices that we studied.

6.1   Carrier flow in the p-i-n photodetector

Figure 6.1: The electron density in the p-i-n photodetector when a modulation is applied.

Figure 6.2: The electron velocity density in the *p-i-n* photodetector when a modulation is applied.

Figure 6.1 shows the electron density flow animation in the device during one period when a modulation is applied to the device. The modulation frequency is 5 GHz. The average output current is 1 mA. The applied bias voltage is 4 V. The other parameters are shown in Table 2.1. The electron density first increases and then decreases as the modulated input optical power first increases and then decreases. We observe that the density changes in the transverse direction, implying a current flow. This transverse current flow is especially important when the reverse bias is low. In Chapter 2, we showed that the difference between the 1D and 2D model is due to the transverse flow in the device. Figure 6.2 shows the electron

velocity during one period when a modulation is applied to the device. We note that we only show the absolute velocity of electrons and holes. The electron velocity is in the $+z$-direction, and the hole velocity is in the $-z$-direction. The velocity changes dramatically at the i-n junction around 2000 nm. Figure 2.2 show the electron and hole velocities as a function of the electric field. The hole velocity increases when the electric field increases. When the electric field is larger than 7 kV/cm, the electron velocity decreases as the electric field increases. With the increase of the electron density, the electric field decreases and the electron velocity increases.

Figure 6.3: The hole density in the p-i-n photodetector when a modulation is applied.

Figure 6.3 shows the hole density in the device during one period when a modulation is applied. Figure 6.4 shows the hole velocity in the device during one

Figure 6.4: The hole velocity in the p-i-n photodetector when a modulation is applied.

period when a modulation is applied. The hole velocity decreases when the hole density increases and the electric field decreases.

6.2   Carrier flow in the PDA and MUTC photodetector

In the PDA and MUTC photodetector, transverse transport is not as important as in the p-i-n photodetector. So, we only show the carrier density and velocity from the 1D simulations. We show the carrier densities and velocities as a function of time in both the PDA and MUTC photodetectors. The carrier densities and velocities behave similarly. So, we only show them for the PDA photodetector.
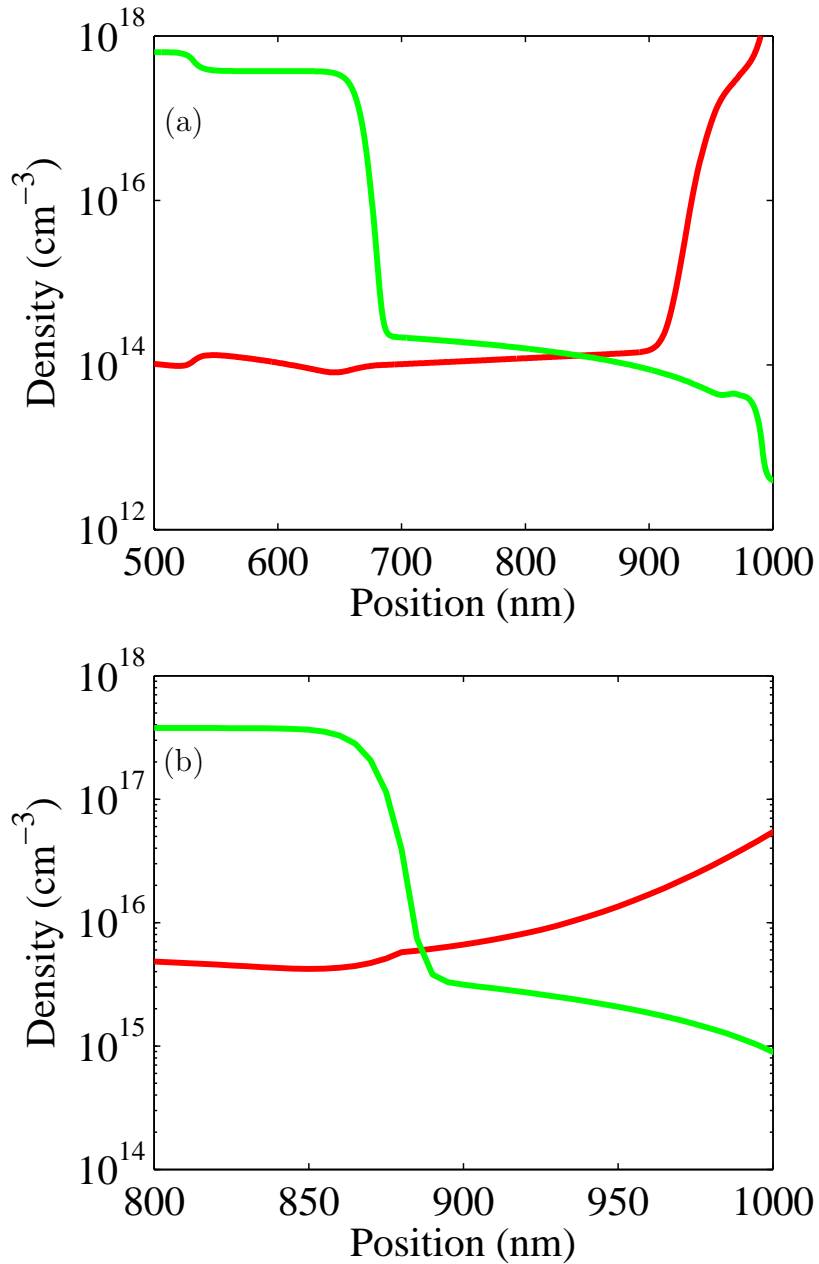
Figure 6.5: The electron and hole densities in the (a) PDA photodetector and (b) MUTC photodetector at steady state. The output current is 10 mA. The modulation depth is 10%. The green curve shows the hole density, and the red curve shows the electron density.

Figure 6.5 shows the electron density at steady state. Figure 6.6 shows the increase of the electron density in the device during the first half period when the

Figure 6.6: The change in the electron density in the (a) PDA photodetector and (b) MUTC photodetector during the first half period when a modulation is applied, compared to the steady state.

Figure 6.7: The electron velocity in the (a) PDA photodetector and (b) MUTC photodetector when a modulation is applied. The electron velocity does not change when the time increases.

optical input is modulated. The applied bias is 6 V. The modulation depth is 10%. The average output current is 10 mA. The other parameters are the same as in Table 2.1 and 3.1. In order to show the electron flow in the device clearly, we show the increase of the electron density from the steady state instead of the electron density itself. Figure 6.7 shows the electron velocity in the device. We find that the electron velocity is almost unchanged. However, the velocity is in the $+z$-direction. So, the electrons move in the $+z$-direction. Due to the heterojunction between InGaAs and InP, the velocity decreases significantly in the heterojunction. In the p-region, the electric field is small, and the velocity is close to zero.

Figure 6.8 shows the increase of hole density in the device during the first half-period when the input is modulated light. The hole density is still larger than the steady state density. The holes move in the $-z$-direction. Figure 6.9 shows the hole velocity in the device. The velocity remains almost constant as the optical intensity changes. The velocity drops significantly in the interface between the p-region and the intrinsic region because the electric field is nearly equal to zero in the p-region. So, there is an accumulation of holes at the interface.

Next we show the transient carrier flow when we instantaneously increase the input optical power by 50%. As a consequence, the output current increases from 10 mA to 15 mA over 200 fs. Figure 6.10 shows the electron density evolution. When the time increases, the electron density increases, and the increase is most rapid in the region between 800 nm and 1000 nm, so that the electrons move in the $+z$-direction. We show the electron velocity in Fig. 6.11. While the electron velocity is almost constant, there is a small change, which is not visible. So, we only show

Figure 6.8: The change in the hole density in the (a) PDA photodetector and (b) MUTC photodetector during the first half period when a modulation is applied, compared to the steady state.

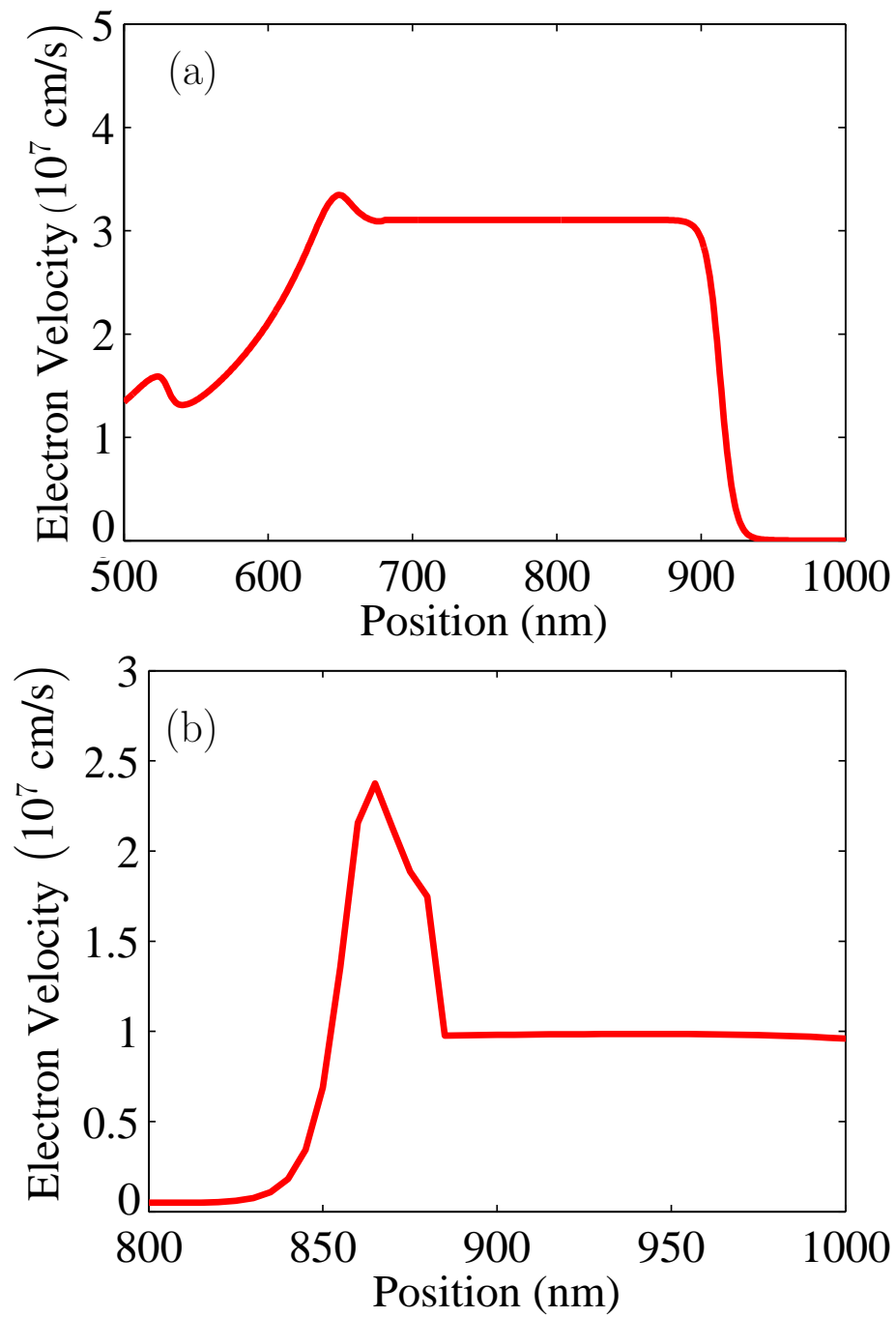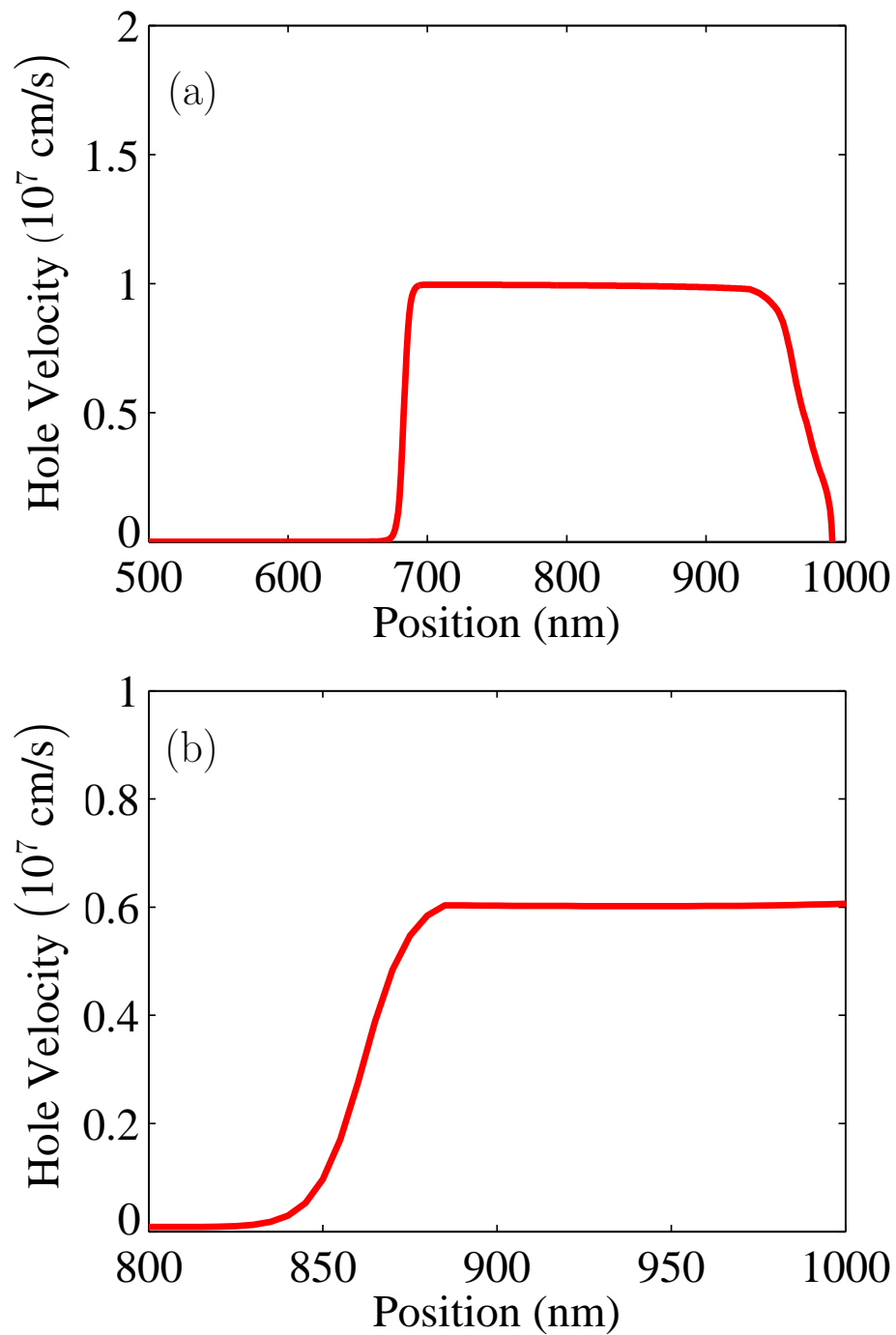Figure 6.9: The hole velocity in the (a) PDA photodetector and (b) MUTC photodetector when a modulation is applied. The hole velocity does not change when the time increases.

Figure 6.10: The increase of the electron density compared to the steady state in the PDA photodetector when the optical power increases.
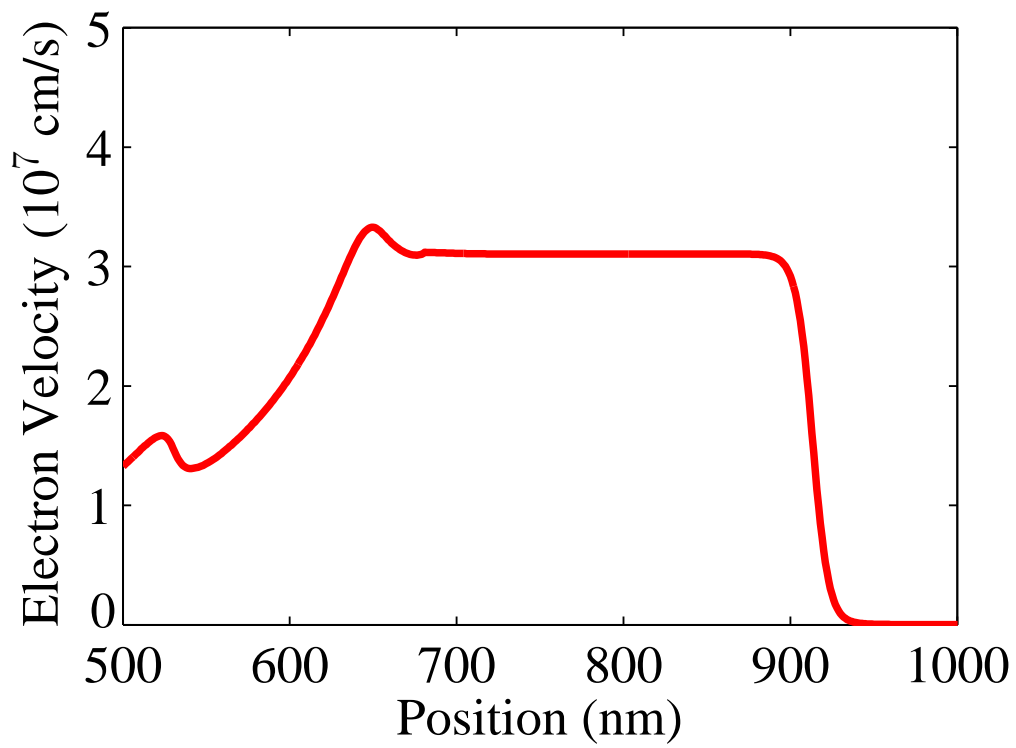
Figure 6.11: The electron velocity in the PDA photodetector when the optical power increases.

Figure 6.12: The electron velocity in the PDA photodetector from 700 to 900 nm in the PDA photodetector when the optical power increases.

the figure instead of animation. Fig. 6.12 shows the small change of the electron velocity from 700 to 900 nm. Figure 6.13 shows the hole density. We observe that the holes move to the p-region, and the hole density in the region between 600 nm and 700 nm increases faster than in the other regions. We show the electron velocity in Fig. 6.14. The hole velocity is almost constant.

The largest difference between the p-i-n photodetector and PDA photodetector or MUTC photodetector is the space charge effect in the intrinsic region. When the input optical power changes in the p-i-n photodetector, the electron and hole velocities change dramatically. However, in the PDA or MUTC photodetector,

Figure 6.13: The increase of the hole density in the PDA photodetector when the optical power increases compared to steady state.
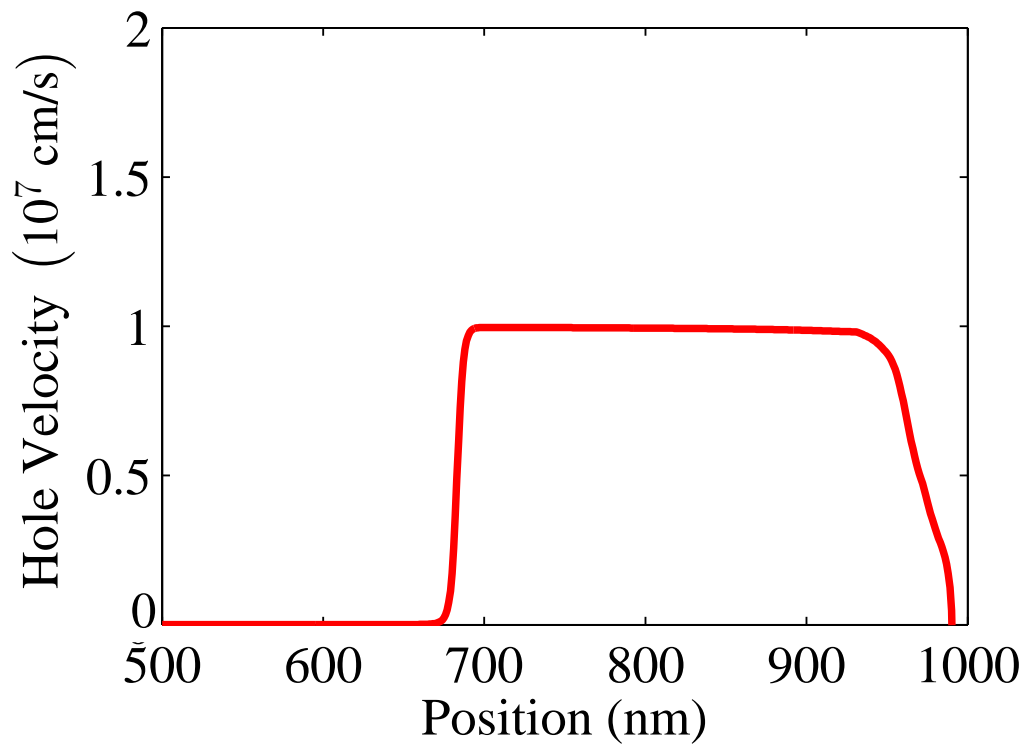
Figure 6.14: The increase of the hole density in the PDA photodetector when the optical power increases compared to steady state.

the electron and hole velocities are almost constant when a modulation is applied. Hence, the PDA or MUTC photodetector has better linearity than a traditional *p-i-n* photodetector.

6.3   Impulse response in the MUTC photodetector

Figure 6.15: The electron and hole current in the MUTC photodetector with pulse generation. The carrier pulse generation is at 900 nm.

In order to determine the current flow in the device in response to an input optical pulse, we turn on carrier pulse generation at particular positions in the device in our simulations, and we turn it off at other positions. The pulse duration has no impact on the result as long as it is 500 fs or less and the total pulse energy is fixed.

128

We used a 500 fs pulse. The applied bias is 4 V. The total pulse energy is 2 pJ. The pulse in Fig. 6.15 shows the impulse response when we turn on the carrier generation at 900 nm. Figure 6.16 shows the impulse response when we turn on the carrier pulse generation at 600 nm. Initially, the electron and hole current are large, and the hole current density rapidly becomes constant due to the holes diffusion, only electron current density is visible. The electrons are the only important carriers in the MUTC photodetector. We observe that the electrons that are generated at 600 nm take a longer time to reach the n-region than the electrons that are generated at 900 nm, because the electrons have a longer distance to travel. We also observe that the electron transit time is smaller in the InGaAs intrinsic region than it is in the InP intrinsic region, which is because the electric field is larger in the InGaAs intrinsic region than in the other regions. These animations show that the electrons are the only traveling carrier in the device, and the transit time only depends on the electrons.

Figure 6.16: The electron and hole current in the MUTC photodetector with pulse generation. The carrier pulse generation is at 600 nm.

6.4 Summary

In this chapter, we show the current flow and the velocity in the p-i-n, PDA, and MUTC photodetectors. We also show the electron and hole transport in both the transverse and longitudinal directions.

The electric and hole velocities change dramatically in the intrinsic region in the p-i-n photodetector, indicating that the space charge effect plays an important role. By contrast, the electron and hole velocities are almost constant in the PDA or MUTC photodetector.

In the MUTC photodetector, we show the impulse response of the device. In the InGaAs intrinsic region, the electric field is larger than in the other regions, and the electron velocity is also larger than in the other regions. The electron transport time in the InP transit region dominates the total electron transit time.

Chapter 7

Conclusion

We have built modified one-dimensional and two-dimensional drift-diffusion models to study nonlinearity in p-i-n, PDA, and MUTC photodetectors. These models include temperature changes, thermionic boundary conditions, incomplete ionization, external loading, history-dependent ionization, and the Franz-Keldysh effect.

We obtained excellent agreement with experiments for the harmonic power and responsivity. In the p-i-n photodetector, we found that impact ionization is an important source of nonlinearity. In the p-i-n photodetector, the output current is about 0.1 mA, and the external loading is not important.

In the PDA photodetector, the output current is 10 mA, and the external loading has a large impact on the nonlinearity and hence the harmonic powers. Due to a thin intrinsic region in these devices, a history-dependent impact ionization should be used in the model. We showed that the Franz-Keldysh effect is an important source of nonlinearity. Decreasing the effective load resistor decreases the higher harmonic powers.

We applied our model to study the source of nonlinearity and AM-to-PM conversion in modified uni-traveling carrier (MUTC) photodetectors. In InGaAs, the velocity of electrons is faster than the velocity of holes by a factor of 2. In an

MUTC photodetector, electrons are the only carriers, which shortens the transit time of carriers through the device and increases response time of the device. The collection and absorption regions are separated, so that it is relatively easy to modify each region to optimize the performance of the device. We obtained good agreement with the experimental data for the MUTC photodetector. We showed that the physical source of the bias null in the IMD2 power is the Franz-Keldysh effect. We investigated the physical origin of a difference between the location of the bias nulls for the sum frequency and difference frequency IMD2 powers, and we showed that it is due to the displacement current in the intrinsic region.

AM-to-PM conversion in the photodetector occurs due to nonlinearities in the photodetector. We used the impulse response to calculate the phase delay in the photodetector, and to analyze the source of AM-to-PM conversion. The AM-to-PM noise conversion is due to a change in the electron transit time when the pulse energy changes. One way to reduce the AM-to-PM noise conversion coefficient is to reduce the transit time by better design of the heterojunction between InGaAs and InP. Our calculation shows that the AM-to-PM noise conversion coefficient can be reduced up to 90% by lowering the heterojunction barrier between InGaAs and InP.

We also showed the electron and hole flow in the *p-i-n*, PDA, and MUTC photodetectors, which allowed us to explain the difference in performance of the three devices.

Bibliography

[1] C. Cox, *Analog Optical Links: Theory and Practice.* Cambridge: Cambridge University Press, 2006.

[2] K. J. Williams, R. D. Esman, and M. Dagenais, "Nonlearities in p-i-n microwave photodetectors," *J. Lightw. Technol.*, vol. 14, pp. 84–96, 1996.

[3] K. J. Williams, "Microwave nonlinearities in photodiodes," PhD Dissertation, University of Maryland College Park, Maryland, USA, 1994.

[4] H. Ito, S. Kodama, Y. Muramoto, T. Furuta, T. Nagatsuma, and T. Ishibashi, "High-speed and high-output InP-InGaAs unitraveling-carrier photodiodes," *IEEE J. Sel. Topics Quantum Electron.*, vol. 10, pp. 709–727, 2004.

[5] A. Seeds, "Microwave photonics," *IEEE Trans. Microw. Theory Techn.*, vol. 50, pp. 877–887, 2002.

[6] T. Clark, M. Currie, and P. Matthews, "Digitally linearized wide-band photonic link," *J. Lightw. Technol.*, vol. 19, pp. 172–179, 2001.

[7] C. Cox, E. Ackerman, G. Betts, and J. Prince, "Limits on the performance of RF-over-fiber links and their impact on device design," *IEEE Trans. Microw. Theory Techn.*, vol. 54, pp. 906–920, 2006.

[8] A. Seeds and K. Williams, "Microwave photonics," *J. Lightw. Technol.*, vol. 24, pp. 4628–4641, 2006.

[9] J. Capmany and D. Novak, "Microwave photonics combines two worlds," *Nature Photonics*, vol. 1, pp. 319–330, 2007.

[10] V. Urick, F. Bucholtz, J. McKinney, P. Devgan, A. Campillo, J. Dexter, and K. Williams, "Long-haul analog photonics," *J. Lightw. Technol.*, vol. 29, pp. 1182–1205, 2011.

[11] T. Nagatsuma, H. Ito, and T. Ishibashi, "High-power RF photodiodes and their applications," *Laser & Photonics Reviews*, vol. 3, pp. 123–137, 2009.

[12] T. Nagatsuma, S. Horiguchi, Y. Minamikata, Y. Yoshimizu, S. Hisatake, S. Kuwano, N. Yoshimoto, J. Terada, and H. Takahashi, "Terahertz wireless communications based on photonics technologies," *Opt. Express*, vol. 21, pp. 23736–23747, 2013.

[13] T. M. Fortier, F. Quinlan, A. Hati, C. Nelson, J. A. Taylor, Y. Fu, J. Campbell, and S. A. Diddams, "Photonic microwave generation with high-power photodiodes," *Opt. Lett.*, vol. 38, pp. 1712–1714, 2013.

[14] F. N. Baynes, F. Quinlan, T. M. Fortier, Q. Zhou, A. Beling, J. C. Campbell, and S. A. Diddams, "Attosecond timing in optical-to-electrical conversion," *Optica*, vol. 2, pp. 141–146, 2015.

[15] T. Nagatsuma, "Progress of instrumentation and measurement toward millimeter-wave photonics," in *International Topical Meeting on Microwave Photonics (MWP)*, 1999, pp. 91–94.

[16] C. H. Lee, *Microwave photonics.* Boca Raton: CRC press, 2013.

[17] V. J. Urick, J. D. Mckinney, and K. J. Williams, *Fundamentals of microwave photonics*. New York: John Wiley & Sons, 2015.

[18] T. Fortier, M. Kirchner, F. Quinlan, J. Taylor, J. Bergquist, T. Rosenband, N. Lemke, A. Ludlow, Y. Jiang, C. Oates *et al.*, "Generation of ultrastable microwaves via optical frequency division," *Nature Photonics*, vol. 5, pp. 425–429, 2011.

[19] S. A. Diddams, M. Kirchner, T. Fortier, D. Braje, A. M. Weiner, and L. Hollberg, "Improved signal-to-noise ratio of 10 GHz microwave signals generated with a mode-filtered femtosecond laser frequency comb," *Opt. Express*, vol. 17, pp. 3331–3340, 2009.

[20] M. Lessing, H. S. Margolis, C. T. A. Brown, P. Gill, and G. Marra, "Suppression of amplitude-to-phase noise conversion in balanced optical-microwave phase detectors," *Opt. Express*, vol. 21, pp. 27057–27062, 2013.

[21] M. Y. Peng, A. Kalaydzhyan, and F. X. Kärtner, "Balanced optical-microwave phase detector for sub-femtosecond optical-RF synchronization," *Opt. Express*, vol. 22, pp. 27102–27111, 2014.

[22] M. Shtaif, C. R. Menyuk, M. L. Dennis, and M. C. Gross, "Carrier-envelope phase locking of multi-pulse lasers with an intra-cavity Mach-Zehnder interferometer," *Opt. Express*, vol. 19, pp. 23202–23214, 2011.

[23] E. C. Levy, O. Okusaga, M. Horowitz, C. R. Menyuk, W. Zhou, and G. M. Carter, "Comprehensive computational model of single- and dual-loop opto-

electronic oscillators with experimental verification," *Opt. Express*, vol. 18, pp. 21461–21476, 2010.

[24] A. Joshi and S. Datta, "Dual InGaAs photodiodes having high phase linearity for precise timing applications," *IEEE Photon. Technol. Lett.*, vol. 19, pp. 1360–1362, 2009.

[25] B. A. Saleh and M. C. Teich, *Fundamentals of Photonics.* New York: Wiley, 2007.

[26] R. Pierret, *Semiconductor Device Fundamentals.* Boston: Addison-Wesley, 1996.

[27] A. Yariv and P. Yeh, *Photonics: Optical Electronics in Modern Communications.* Oxford: Oxford University Press, 2007.

[28] K. J. Williams, R. D. Esman, and M. Dagenais, "Effects of high space-charge fields on the response of microwave photodetectors," *IEEE Photon. Technol. Lett.*, vol. 6, pp. 639–641, 1994.

[29] K. J. Williams, R. D. Esman, and M. Dagenais, "Nonlinearities in p-i-n microwave photodetectors," *J. Lightw. Technol.*, vol. 14, pp. 84–96, 1996.

[30] Y.-L. Huang and C.-K. Sun, "Nonlinear saturation behaviors of high-speed p-i-n photodetectors," *J. Lightw. Technol.*, vol. 18, pp. 203–212, 2000.

[31] J. Guo, Y. Zuo, Y. Zhang, W. Ding, B. Cheng, J. Yu, and Q. Wang, "Simulation research of nonlinear behavior induced by the charge-carrier effect in

resonant-cavity-enhanced photodetectors," *J. Lightw. Technol.*, vol. 25, pp. 2783–2790, 2007.

[32] H. Jiang, D. S. Shin, G. L. Li, T. A. Vang, D. C. Scott, and P. K. L. Yu, "The frequency behavior of the third-order intercept point in a waveguide photodiode," *IEEE Photon. Technol. Lett.*, vol. 12, pp. 540–542, 2000.

[33] G. M. Dunn, A. B. Walker, A. J. Vickers, and V. R. Wicks, "Transient response of photodetectors," *J. Appl. Phys.*, vol. 79, pp. 7329–7338, 1996.

[34] A. B. Walker, "One- and two-dimensional models of the transient response of metal–semiconductor–metal photodetectors including diffraction," *Semiconduct. Sci. Technol.*, vol. 12, pp. 1265–1272, 1997.

[35] S. P. Wilson and A. B. Walker, "Mechanism of impact ionization enhancement in GaAs p-i-n diodes under high illumination conditions," *Semiconduct. Sci. Technol.*, vol. 13, pp. 190–193, 1998.

[36] Y. Fu, H. Pan, Z. Li, A. Beling, and J. C. Campbell, "Characterizing and modeling nonlinear intermodulation distortions in modified uni-traveling carrier photodiodes," *IEEE J. Quantum Electron.*, vol. 47, pp. 1312–1319, 2011.

[37] Y. Hu, B. Marks, C. Menyuk, V. Urick, and K. Williams, "Modeling sources of nonlinearity in a simple p-i-n photodetector," *J Lightw. Technol.*, vol. 32, pp. 3710–3720, 2014.

[38] H. Jiang and P. K. Yu, "Equivalent circuit analysis of harmonic distortions in photodiode," *IEEE Photon. Technol. Lett.*, vol. 10, pp. 1608–1610, 1998.

[39] K. Horio and H. Yanai, "Numerical modeling of heterojunctions including the thermionic emission mechanism at the heterojunction interface," *IEEE Trans. Electron Dev.*, vol. 37, pp. 1093–1098, 1990.

[40] B. K. Crone, P. S. Davids, I. H. Campbell, and D. L. Smith, "Device model investigation of bilayer organic light emitting diodes," *J. Appl. Phys.*, vol. 87, pp. 1974–1982, 2000.

[41] K. Yang, J. C. Cowles, J. R. East, and G. I. Haddad, "Theoretical and experimental DC characterization of InGaAs-based abrupt emitter HBT's," *IEEE Trans. Electron Dev.*, vol. 42, pp. 1047–1058, 1995.

[42] H. Wang and G.-I. Ng, "Avalanche multiplication in InP/InGaAs double heterojunction bipolar transistors with composite," *IEEE Trans. Electron Dev.*, vol. 47, pp. 1125–1133, 2000.

[43] Y. Hu, C. R. Menyuk, V. J. Urick, and K. J. Williams, "Sources of nonlinearity in a p-i-n photodetector at high applied reverse bias," in Proc. *IEEE Topical Meeting on Microwave Photonics (MWP)*. 2013, pp. 282–285.

[44] A. S. Hastings, D. A. Tulchinsky, K. J. Williams, H. Pan, A. Beling, and J. C. Campbell, "Minimizing photodiode nonlinearities by compensating voltage-dependent responsivity effects," *J. Lightw. Technol.*, vol. 28, pp. 3329–3333, 2010.

[45] S. Selberherr, *Analysis and simulation of semiconductor devices.* New York: Springer-Verlag Wien, 1984.

[46] D. A. Tulchinsky, X. Li, N. Li, S. Demiguel, J. C. Campbell, and K. J. Williams, "High-saturation current wide-bandwidth photodetectors," *IEEE J. Sel. Topics Quantum Electron.*, vol. 10, pp. 702–708, 2004.

[47] Y. Hu, T. F. Carruthers, C. R. Menyuk, M. N. Hutchinson, V. J. Urick, and K. J. Williams, "Simulation of a partially depleted absorber (PDA) photodetector," *Opt. Express*, vol. 23, pp. 20 402–20 417, 2015.

[48] A. S. Hastings, D. A. Tulchinsky, and K. J. Williams, "Photodetector nonlinearities due to voltage-dependent responsivity," *IEEE Photon. Technol. Lett.*, vol. 21, pp. 1642–1644, 2009.

[49] Y. Hu and C. Menyuk, "Computational modeling of nonlinearity in a pin photodetector," in *2013 International Semiconductor Device Research Symposium (ISDRS)*, 2013, pp. 1–2.

[50] R. Mcintyre, "A new look at impact ionization-part I: A theory of gain, noise, breakdown probability, and frequency response," *IEEE Trans. Electron Dev.*, vol. 46, pp. 1623–1631, 1999.

[51] P. Yuan, K. A. Anselm, C. Hu, H. Nie, C. Lenox, A. L. Holmes, B. G. Streetman, J. C. Campbell, and R. McIntyre, "A new look at impact ionization-Part II: Gain and noise in short avalanche photodiodes," *IEEE Trans. Electron Dev.*, vol. 46, pp. 1632–1639, 1999.

[52] M. Dentan and B. D. Cremoux, "Numerical simulation of the nonlinear response of a p-i-n photodiode under high illumination," *J. Lightw. Technol.*, vol. 8, pp. 1137–1144, 1990.

[53] K. Williams, R. Esman, R. Wilson, and J. Kulick, "Differences in p-side and n-side illuminated p-i-n photodiode nonlinearities," *IEEE Photon. Technol. Lett.*, vol. 10, pp. 132–134, 1998.

[54] S. P. Wilson, "Modelling of p-i-n photodiodes under high illumination conditions," *Int. J. Numer. Model*, vol. 10, pp. 139–151, 1997.

[55] S. J. Woods, S. P. Wilson, and A. B. Walker, "Non-unique solutions in drift diffusion modelling of phototransistors," *Int. J. Numer. Model*, vol. 13, pp. 37–57, 2000.

[56] S. A. Malyshev, A. L. Chizh, and Y. G. Vasileuski, "2D Simulation of planar InP/InGaAs avalanche photodiode with no guard rings," in *NUSOD*, 2008, pp. 81–82.

[57] A. Habibpoor and H. Mashayekhi, "Numerical modeling of the effect of optical pulse position on the impulse response of a Metal-Semiconductor-Metal (MSM) photodetector (low field condition)," *Eur. Phys. J. Appl. Phys.*, vol. 55, p. 10502, 2011.

[58] A. A. Mohamed, N. A. Ayad, A. Nabih, Z. Rashed, and H. M. El-Hageen, "Speed response and performance degradation of high temperature gamma

irradiated silicon p-i-n photodiodes," *Int. J. Com. Sci. Telecom.*, vol. 2, pp. 15–22, 2011.

[59] K. W. Boer, *Survey of Semiconductor Physics.* New York: Van Nostrand Reinhold, 1990.

[60] C. Hilsum, "Simple empirical relationship between mobility and carrier concentration," *Electron. Lett.*, vol. 10, pp. 259–260, 1974.

[61] T. P. Pearsall, "Impact ionization rates for electrons and holes in $Ga_{0.47}In_{0.53}As$," *Appl. Phys. Lett.*, vol. 36, pp. 218–220, 1979.

[62] J. Marsland, R. Woods, and C. Brownhill, "Lucky drift estimation of excess noise factor for conventional avalanche photodiodes including the dead space effect," *IEEE Trans. Electron Dev.*, vol. 39, pp. 1129–1135, 1992.

[63] K. A. Anselm, H. Nie, C. Hu, C. Lenox, P. Yuan, G. Kinsey, J. C. Campbell, and B. Streetman, "Performance of thin separate absorption, charge, and multiplication avalanche photodiodes," *IEEE J. Quantum Electron.*, vol. 34, pp. 482–490, 1998.

[64] P. Yuan, C. C. Hansing, K. A. Anselm, C. V. Lenox, H. Nie, J. Holmes, A. L., B. G. Streetman, and J. C. Campbell, "Impact ionization characteristics of III-V semiconductors for a wide range of multiplication region thicknesses," *IEEE J. Quantum Electron.*, vol. 36, pp. 198–204, 2000.

[65] M. A. Saleh, M. Hayat, P. Sotirelis, A. Holmes, J. C. Campbell, B. Saleh, and M. Teich, "Impact-ionization and noise characteristics of thin III-V avalanche photodiodes," *IEEE Trans. Electron Dev.*, vol. 48, pp. 2722–2731, 2001.

[66] J. Callaway, "Optical absorption in an electric field," *Phys. Rev.*, vol. 130, pp. 549–553, 1963.

[67] R. J. Elliott, "Intensity of optical absorption by excitons," *Phys. Rev.*, vol. 108, pp. 1384–1389, 1957.

[68] K. Tharmalingam, "Optical absorption in the presence of a uniform field," *Phys. Rev.*, vol. 130, pp. 2204–2206, 1957.

[69] J. D. Dow and D. Redfield, "Electroabsorption in semiconductors: The excitonic absorption edge," *Phys. Rev. B*, vol. 1, pp. 3358–3371, 1969.

[70] L. D. Landau and E. M. Lifshitz, *Quantum Mechanics.* London: Pergamon Press, 1958.

[71] H. I. Ralph, "On the theory of the Franz-Keldysh effect," *J. Phys. C*, vol. 1, pp. 378–386, 1968.

[72] X. Zhang, "A planar violet electroabsorption modulator and modeling of electric effects on zinc oxide excitons," PhD Dissertation, North Carolina State University, Raleigh, USA, 2006.

[73] J. Q. Gonzalez and D. Thompson, "Getting started with Numerov's method," *Computers in Physics*, vol. 11, pp. 514–515, 1997.

[74] J. W. Cooley, "An improved eigenvalue corrector formula for solving the schrödinger equation for central fields," *Mathematics of Computation*, vol. 15, pp. 363–374, 1961.

[75] B. O. Seraphin and N. Bottka, "Franz-Keldysh effect of the refractive index in semiconductors," *Phys. Rev.*, vol. 139, pp. A560–A565, 1965.

[76] S. Selberherr, *Analysis and simulation of semiconductor devices.* New York: Springer-Verlag Wien, 1984.

[77] V. Palankovski, "Simulation of heterojunction bipolar transistors," PhD Dissertation, Technische Universitat Wien, Viena, Austria, 2000.

[78] M. Wagner, "Simulation of thermoelectric devices," PhD Dissertation, Technische Universitat Wien, Viena, Austria, 2007.

[79] M. Sotoodeh, A. H. Khalid, and A. A. Rezazadeh, "Empirical low-field mobility model for III-V compounds applicable in device simulation codes," *J. Appl. Phys.*, vol. 87, pp. 2890–2900, 2000.

[80] R. Quay, "Analysis and simulation of high electron mobility transistors," PhD Dissertation, Technische Universitat Wien, Viena, Austria, 2001.

[81] S. M. Sze and K. K. Ng, *Physics of Semiconductor Devices.* New York: Wiley-Interscience, 2007, 3rd edition.

[82] R. Quay, C. Moglestue, V. Palankovski, and S. Selberherr, "A temperature dependent model for the saturation velocity in semiconductor materials," *Mater. Sci. Semicond. Process.*, vol. 3, pp. 149–155, 2000.

[83] J. Taylor and V. Tolstikhin, "Intervalence band absorption in InP and related materials for optoelectronic device modeling," *J. App. Phys.*, vol. 87, pp. 1054 –1059, 2000.

[84] E. Zielinski, H. Schweizer, K. Streubel, H. Eisele, and G. Weimann, "Excitonic transitions and exciton damping processes in InGaAs/InP," *J. App. Phys.*, vol. 59, pp. 2196–2204, 1986.

[85] K. Tharmalingam, "Optical absorption in the presence of a uniform field," *Phys. Rev.*, vol. 130, pp. 2204–2206, 1963.

[86] H. Ito, T. Furuta, S. Kodama, and T. Ishibashi, "Zero-bias high-speed and high-output-voltage operation of cascade-twin unitravelling-carrier photodiode," *Electron. Lett.*, vol. 36, pp. 2034–2036, 2000.

[87] E. Rouvalis, M. Chtioui, F. van Dijk, F. Lelarge, M. J. Fice, C. C. Renaud, G. Carpintero, and A. J. Seeds, "170 GHz uni-traveling carrier photodiodes for InP-based photonic integrated circuits," *Opt. Express*, vol. 20, pp. 20090–20095, 2012.

[88] Z. Li, H. Pan, H. Chen, A. Beling, and J. C. Campbell, "High-saturation-current modified uni-traveling-carrier photodiode with cliff layer," *IEEE J. Quantum Electron.*, vol. 46, pp. 626–632, 2010.

[89] M. N. Hutchinson, S. Estrella, and M. Mashanovitch, "Packaged High Power MUTC Photodetectors for High SFDR Applications," AVFOP 2016, WA2.2, Nov. 2016.

[90] N. J. Frigo, M. N. Hutchinson, and J. R. Peasant, "Characterization of photo-diode nonlinearities by output frequency analysis," *J. Lightw. Technol.*, vol. 34, pp. 4696–4704, 2016.

[91] N. B. Carvalho and J. C. Pedro, "Large- and small-signal imd behavior of microwave power amplifiers," *IEEE Trans. Microw. Theory Techn.*, vol. 47, pp. 2364–2374, 1999.

[92] N. B. Carvalho and J. C. Pedro, "A comprehensive explanation of distortion sideband asymmetries," *IEEE Trans. Microw. Theory Techn.*, vol. 50, pp. 2090–2101, 2002.

[93] M. N. Draa, A. S. Hastings, and K. J. Williams, "Comparison of photodiode nonlinearity measurement systems," *Opt. Express*, vol. 19, pp. 12635–12645, 2011.

[94] J. Kim, J. A. Cox, J. Chen, and F. X. Kärtner, "Drift-free femtosecond timing synchronization of remote optical and microwave sources," *Nature Photonics*, vol. 2, pp. 733–736, 2008.

[95] K. Jung and J. Kim, "All-fibre photonic signal generator for attosecond timing and ultralow-noise microwave," *Scientific Reports*, vol. 5, p. 16520, 2015.

[96] P. Ghelfi, F. Laghezza, F. Scotti, G. Serafino, A. Capria, S. Pinna, D. Onori, C. Porzi, M. Scaffardi, A. Malacarne *et al.*, "A fully photonics-based coherent radar system," *Nature*, vol. 507, pp. 341–345, 2014.

[97] T. M. Fortier, F. Quinlan, A. Hati, C. Nelson, J. A. Taylor, Y. Fu, J. Campbell, and S. A. Diddams, "Photonic microwave generation with high-power photodiodes," *Opt. Lett.*, vol. 38, pp. 1712–1714, 2013.

[98] X. Xie, K. Li, Y. Shen, Q. Li, J. Zang, A. Beling, and J. Campbell, "Photonic generation of high-power pulsed microwave signals," *J. Lightw. Technol.*, vol. 33, pp. 3808–3814, 2015.

[99] W. Zhang, T. Li, M. Lours, S. Seidelin, G. Santarelli, and Y. Le Coq, "Amplitude to phase conversion of InGaAs pin photo-diodes for femtosecond lasers microwave signal generation," *Appl. Phys. B*, vol. 106, pp. 301–308, 2012.

[100] J. Taylor, S. Datta, A. Hati, C. Nelson, F. Quinlan, A. Joshi, and S. Diddams, "Characterization of power-to-phase conversion in high-speed p-i-n photodiodes," *IEEE Photonics J.*, vol. 3, pp. 140–151, 2011.